uc3m | Universidad Carlos III de Madrid

TESIS DOCTORAL

Aerodynamic forces and vortex structures of flapping wings in forward flight

Autor:
Alejandro Gonzalo Grande

Tutor/Director:
Manuel García-Villalba Navaridas

Codirector:
Óscar Flores Arias

Programa Interuniversitario en Mecánica de Fluidos

Leganés, Septiembre 2018

A mis padres y a mi hermano. Con vosotros a mi lado todo es más fácil.

Tesis doctoral

Aerodynamic forces and vortex structures of flapping wings in forward flight

Autor: Alejandro Gonzalo Grande

Directores: Manuel García-Villalba Navaridas y Óscar Flores Arias

Firma del Tribunal Calificador:

Firma

Presidente:

Secretario:

Vocal:

Calificación:

Leganés, de de

Abstract

In the last two decades, there has been an increasing interest to develop micro air vehicles (MAVs) capable to fly like insects and small birds. These animals have evolved over centuries achieving outstanding flight abilities. Thus, engineers are trying to mimic their flapping motions to develop devices with high maneuverability. Although the unconventional unsteady aerodynamic mechanisms are well known since the 1980s, their systematic applicability to the practical design of MAVs has been proven difficult. The problem arises due to the vast amount of maneuvers performed by these flying animals, which leads to an incredibly large range of kinematics parameters. This, added to the diversity of geometric parameters (body morphology, wing shape, size and weight,...) of the different birds and insects makes really difficult to develop reliable models for the aerodynamic forces.

In order to contribute to the understanding of the aerodynamics of MAVs, in this thesis we study flapping wings in forward flight by means of direct numerical simulations. More specifically, the question we want to address is how the aerodynamic forces change when the wing kinematics are varied. Thus, we consider the transition from wings rotating with respect to their roots (flapping wing) to wings oscillating vertically (heaving wings). To that end, several direct numerical simulations of the flow (at low Reynolds number, $Re = 500$) around a pair of wings have been performed, varying the distance between an axis parallel to the flying velocity and the wing root (radius of flapping motion, R). Apart from R, which shifts from flapping to heaving motion, another kinematic parameter has been varied. This parameter is the maximum vertical displacement of the outboard wing tip (h_0), which has been kept fixed for most of the cases studied. Besides, the importance of the wing geometry has also been considered by studying wings with two different aspect ratios (AR). Note that to keep the problem as simple as possible, the same angular frequency has been imposed in all the motions and no other kinematics and geometric complexities (e.g. pitching motion or wing geometric twist) have been considered.

The database generated has been studied in terms of net aerodynamic forces during the cycle, forces distributions on the wings surface and flow structures around the wings. Among these structures, a particular attention has been paid to the leading edge vortex (LEV), which has been characterized qualitatively and quantitatively. For the latter characterization, a methodology to track the position of the LEV core in time and space has been developed. This methodology has also been used to evaluate several flow quantities along the LEV and their relation with the aerodynamic forces on the wings.

The results show that in the configurations studied, the local aerodynamic forces,

forces distributions on the wing surface, and flow structures are mainly associated to the local effective angle of attack (α_e). This parameter is defined as the angle formed by chordline and the relative velocity vector, which is obtained with the flight velocity and the local vertical velocity of a corresponding wing section. Note that α_e increases along the wing span with R for cases with equal h_0 and is maximum close to the outboard wing tip for cases with larger h_0. Thus, cases with larger effective angle of attack averaged along the wing span ($\langle\alpha_e\rangle$) produce net forces with larger peaks during the cycle when the AR and the h_0 are equal. This is translated into a larger mean lift and a smaller mean drag generation during the downstroke motion. However, cases with higher AR produced larger mean aerodynamic forces during the downstroke even with somewhat smaller $\langle\alpha_e\rangle$ values. The forces have been decomposed in normal and tangential contributions, showing that in all cases the former is responsible for almost the whole lift and thrust generation, while the latter produces the drag force.

The importance of the LEV in the lift generation has been observed through the comparison of the forces distributions on the upper wing surface at the mid-downstroke and the vortical structures. For the flapping cases the LEV structure has a conical shape and its intensity increases from the root to the outboard wing tip, where the forces distributions show larger values. Using the methodology developed to characterize the LEV, it has been shown that the local position of the LEV core depends mainly on α_e along the wing span, except close to the wing tips. In fact, cases with different R and AR, but equal α_e show LEVs with similar positions and therefore comparable local aerodynamic forces. The evolution of the LEV during the downstroke seems also to be linked with the α_e of the wing section studied, presenting more separation from the wing and more chordwise distance respect to the leading edge for larger α_e. However, it has been observed that for cases with equal R and AR, but different values of α_e along the wing span, the chordwise position remains almost equal, both along the wing span and during its time evolution. On the other hand, the local lift force coefficient during the downstroke seems to be associated to the LEV circulation (which in turn depends on α_e), provided that the LEV is sufficiently close to the wing.

Resumen

En las últimas dos décadas ha crecido sustancialmente el interés en el desarrollo de micro vehículos aéreos (MVAs) que sean capaces de volar como insectos y/ó pájaros pequeños. La evolución a lo largo de los siglos ha dotado a estos animales con la capacidad de lograr increibles maniobras de vuelo. Por ello, tanto investigadores como ingenieros están intentando desarrollar dispositivos que sean capaces de imitar sus movimientos de aleteo y de maniobrar en el aire igual que ellos. Aunque los mecanismos no convencionales de la aerodinámica no estacionaria se conocen desde los años 80, es complicado aplicarlos de forma sistemática en el diseño de MVAs. El problema que aparece se debe principalmente a la gran cantidad de maniobras que estos animales son capaces de realizar, que se traduce en una variedad de parámetros cinemáticos extremadamente amplia como para ser abordarda. Esto, sumado a la diversidad de parámetros geométricos (morfología del cuerpo del animal, forma, tamaño y peso del ala,...) que tienen los diferentes pájaros e insectos, complica de forma avismal el desarrollo de modelos aptos para predecir las fuerzas aerodinámicas.

Con el objetivo de ampliar el entendimiento de los fenómenos aerodinámicos que ocurren en el vuelo de los MVAs, en esta tesis estudiamos un configuración de dos alas batientes que vuelan hacia adelante mediante simulaciones numéricas directas. Más específicamente, queremos saber cómo cambian las fuerzas aerodinámicas cuando cambia la cinemática del ala. Con este objetivo en mente, hemos considerado la transición entre alas que rotan respecto a sus respectivas raíces y alas que oscilan verticalmente. Para ello, se han realizado varias simulaciones numéricas directas que estudian el flujo (a bajo número de Reynolds, $Re = 500$) alrededor de un par de alas, variando la distancia entre un eje paralelo a la velocidad de vuelo y la raíz de cada ala (radio del movimiento de aleteo, R). A parte del R, que hace que el ala transicione del movimiento de aleteo al movimiento de oscilación vertical, se ha variado otro parámetro cinemático. Este parámetro es el desplazamiento vertical máximo de la punta exterior del ala (h_0), que se ha mantenido fijo para la mayoría de los casos estudiados. Además, la importancia de la geometría del ala también ha sido considerada estudiando alas con dos relaciones de aspecto (AR) diferentes. Tenga en cuenta que, para que el problema sea lo más simple posible, se ha impuesto la misma frecuencia angular en todos los movimientos y no se han considerado otras complejidades cinemáticas y geométricas (como por ejemplo, el movimiento de cabeceo del ala o el giro geométrico de la misma).

La base de datos generada se ha estudiado en función de las fuerzas aerodinámicas netas durante un ciclo, las distribuciones de fuerzas en las superficie de las alas y las estructuras del flujo que aparecen alrededor de las alas. Entre estas estructuras, se

ha prestado especial atención al torbellino que aparece en el borde de ataque del ala (TBA), que se ha caracterizado de forma cualitativa y cuantitativa. Para la última caracterización mencionada, se ha desarrollado una metodología que es capaz de rastrear la posición del centro del TBA en el espacio y en el tiempo. Esta metodología también permite evaluar varias cantidades del flujo a lo largo del TBA con el objetivo de poder relacionarlas con las fuerzas aerodinámicas producidas por las alas.

Los resultados de la tesis muestran que en las configuraciones estudiadas, las fuerzas aerodinámicas netas, las distribuciones de fuerzas en la superficie del ala y las estructuras del flujo dependen de forma local del ángulo de ataque efectivo local (α_e). Este parámetro se define como el ángulo formado entre la línea de la cuerda del ala y el vector velocidad relativa, que se obtiene de la composición de la velocidad de vuelo y la velocidad vertical local de la sección del ala correspondiente. Tenga en cuenta que el α_e aumenta a lo largo de la envergadura del ala a medida que lo hace R para los casos que tienen el mismo h_0 y que alcanza valores máximos cerca de la punta exterior del ala para los casos que tienen mayor h_0. Por lo tanto, los casos que tienen un mayor ángulo de ataque efectivo promediado a lo largo de la envergadura del ala ($\langle\alpha_e\rangle$) producen fuerzas netas durante el ciclo que tienen picos más altos (siempre que la AR de sus alas y el h_0 no varíen entre esos casos). Este hecho se traduce en la obtención de una mayor sustentación media y una menor generación de resistencia media durante el movimiento de descenso del ala. Sin embargo, se ha observado que los casos con mayor AR producen mayores fuerzas aerodinámicas medias durante el movimiento de descenso del ala, incluso aunque sus valores del $\langle\alpha_e\rangle$ sean algo más pequeños. Las fuerzas se han descompuesto en sus contribuciones normal y tangencial, la primera contribución es responsable de casi toda la generación de sustentación y empuje del ala, mientras que la segunda produce la fuerza de arrastre.

La comparación de las distribuciones de fuerzas en la superficie superior del ala a la mitad del movimiento de descenso de la misma y de las estructuras de torbellino, nos ha servido para ver la importancia que tiene el TBA en la generación de sustentación. Para los casos de aleteo (excluyendo los casos de movimiento oscilatorio), la estructura del TBA tiene una forma cónica y su intensidad aumenta desde la raíz del ala hasta su punta exterior, donde las distribuciones de fuerzas muestran sus valores más altos. Usando la metodología desarrollada para caracterizar el TBA, se ha demostrado que la posición local del centro del TBA depende principalmente del α_e a lo largo de la envergadura del ala, excepto cerca de las puntas de las mismas. De hecho, algunos casos con diferentes R y AR, pero con los mismos α_e, tienen TBAs con posiciones similares, que provocan una produción de fuerzas aerodinámicas locales comparables. La evolución del TBA durante el movimiento desdendente del ala también parece estar vinculada con el α_e de la sección del ala considerada. Para valores más elevados del α_e el centro del TBA presenta una mayor separación vertical respecto del ala y una distancia mayor respecto

del borde de ataque del ala en la dirección de la cuerda. Sin embargo, se ha observado que para casos con el mismo R y AR, y con distintos valores del α_e a lo largo de la envergadura del ala, la posición en la dirección de la cuerda permanece casi igual, tanto a lo largo de la envergadura del ala como durante su evolución temporal. Por otro lado, el coeficiente de fuerza de sustentación local parece estar asociado a la circulación del TBA (que a su vez depende del α_e) durante el movimiento de descenso del ala. Esto ocurre siempre que el TBA esté lo suficientemente cerca del ala.

Acknowledgments

The research presented in this thesis has been carried out in the department of Bioengineering and Aerospace engineering at Universidad Carlos III de Madrid. The financial support has been provided by the Universidad Carlos III de Madrid through a PIF scholarship awarded on a competitive basis, and by the Spanish Ministry of Economy and Competitiveness through grants TRA2013-41103-P (MINECO/FEDER,UE) and DPI2016-76151-C2-2-R (AEI/FEDER, UE). The simulations were partially performed at the Steinbuch Centre for Computing (SCC), Karlsruhe.

Agradecimientos

En primer lugar me gustaría dar las gracias a Manolo y a Óscar por darme la oportunidad de realizar este doctorado, por ayudarme durante todos estos años y por enseñarme a dar mis primeros pasos en el mundo de la investigación. Hay que reconocer que aunque nos ha tocado esprintar un poco en el último momento, al final hemos conseguido llegar a tiempo.

Manu, eres el siguiente. Gracias por responderme a cada una de las mil y una preguntas que te hecho a lo largo de estos años. Sin tu ayuda TUCAN todavía sería un misterio para mi. Has sido como un tercer tutor/director ó como quieran llamarlo.

A Toni, por ser ese amigo que se necesita como el comer durante el doctorado. Ese que te escucha y te entiende, y que te inyecta moral en los momentos más difíciles.

Cierro el grupo de CFD contigo Gonzalo. Gracias por ese análisis con tu código de paneles que me ayudó a cerrar el capítulo 4 y también por la tarea de revisión del manuscrito. Sin ti esto sería un campo de typos.

Para poder trabajar a gusto hay que estar cómodo en el trabajo y nada mejor para crear un buen ambiente que tener compañeros de despacho como Dani, Marco, Bin, Manu, Toni, Felipe, Carlos, Víctor, Rocco, Gonzalo y Álex. Gracias chicos por hacer las jornadas laborales más entretenidas y los viajes de vuelta a casa en Cercanías más cortos.

Por otro lado tengo que agradecer a Juancar la oportunidad que me dió de trabajar en su lab en UCSD. Parecía que 3 meses no eran muchos, pero la verdad es que ha sido una experencia inolvidable. A nivel profesional porque he encontrado aplicaciones de la mecánica de fluidos muy interesantes y a nivel personal por haber conocido a Ricardo, al que le doy las gracias por haberme presentado a todos sus amigos y haberme tratado como uno más desde el principio.

Es imposible acabar un doctorado sin hacer algo de deporte (*mens sana in corpore sano*). Por eso quiero dar las gracias a Fer, por enseñarme a jugar al tenis y a no perder los nervios. A todos los compañeros de la Naranja Mecánica, por todos estos años de fútbol a nuestra manera y por las cervecitas después de los partidos (ya sean para celebrar las buenas faenas ó para olvidar los malos partidos).

A mis queridos industriales Rubén, Víctor, Feito, David, Juanillo y Alberto, por esos viajes que te permiten resetear y sin los que uno perdería la cabeza.

A los incombustibles Víctor, Pablo, Jorla, Rober, Pedro, Jose, Jaira, Chema, Jubi y Peri, por todos los buenos findes y no findes que hemos pasado juntos.

A mi compañeros de piso Carlos y Nico, porque vivir con dos amigos de toda la vida como vosotros es una pasada.

Por último a mi familia, empezando por mi padres. Sabéis que aunque os pique de vez en cuando, os quiero y os admiro con locura. A mi hermano, porque aunque no hablamos muy a menudo, siempre estás ahí cuando de verdad te necesito. Al pequeńajo de la familia, Dario, por sacarme una sonrisa hasta en momentos de estrés extremo y a su mamá María por darme en qué pensar después de nuestras conversaciones. A mis tías Pilar y Hontanares, y a mis primos Samuel y Rodrigo, por preocuparse por mi y tenerme siempre en su cabeza y en su corazón.

Contents

Glossary

ρ Density of the fluid

ν Dinaymic viscosity of the fluid

u_∞ Forward flight velocity

t Time

$\mathbf{\Omega}$ Angular velocity of the non-inertial reference frame

c Chord of the wing

R Radius of flapping motion

b Span of the wing

S Wetted surface of the wing

D Diameter of the sphere

h Channel semi-height

$\mathbf{n}$ Local unit vector normal to the wing surface pointing towards the fluid

$\boldsymbol{\tau}$ Local unit vector tangent to the wing surface pointing towards the fluid

ε Stretch factor

r Maximum grid growth ratio

$\mathbf{u}$ Absolute velocity of the fluid

$\mathbf{u}'$ Relative velocity of the fluid

ϕ Pseudo-pressure

p Pressure

u Streamwise component of the Flow velocity

v Lateral component of the Flow velocity

w Vertical component of the Flow velocity

ω_{y_w} Spanwise component of the vorticity

$\boldsymbol{\omega'}$ Relative vorticity

$\boldsymbol{\omega}$ Absolute vorticity

Q Second invariant of the absolute velocity gradient tensor

Q' Second invariant of the relative velocity gradient tensor

Q'_{th} Threhold of the second invariant of the relative velocity gradient tensor

λ_2 Lambda2 vortex criterion

$\mathbf{u}^e$ Explicit estimation of flow velocity in the Eulerian mesh

$\mathbf{U}^e$ Estimation of flow velocity in the Lagrangian mesh

$\mathbf{U}^d$ Desired velocity of the Lagrangian points

$\mathbf{f_{IBM}}$ Volume force vector due to the immersed bodies in the Eulerian mesh

$\mathbf{F_{IBM}}$ Volume force vector due to the immersed bodies in the Lagrangian mesh

U_c Characteristic velocity used to non-dimensionalized the Navier-Stokes equations

L_c Characteristic length used to non-dimensionalized the Navier-Stokes equations

$\mathbf{U}$ Velocity at the surface of the body

u_a Advective velocity for the exit boundary condition

$\mathbf{L}_2$ Euclidean norm of a vector

$t_{\mathbf{task}}$ Time spent on a task of TUCAN

$t_{\phi\mathbf{solver}}$ Time required to solve the pseudo-pressure linear solver

N_P Number of processors used to perform a simulation

N_G Number of grid points of the computational domain

N_S Number of steps given to solve a simulation

t_u Unitary time

t_u^{eq} Equivalent unitary time

u_0 Maximum velocity at the center line of the channel

δ_c Direction perpendicular to the walls of the channel.

u_τ Friction velocity

Re_τ Reynolds number based on the friction velocity

u_b Bulk velocity

Re_b Reynolds number based on the bulk velocity

u_{sph} Velocity of the sphere

α_e Effective angle of attack

Φ Flapping angle

Φ_0 Amplitude of flapping motion

ω Angular frequency

h_0 Vertical displacement of the outboard wing tip

T Period of the flapping motion

w_w Vertical velocity of thw wing

n_c Number of grid points per chord length (c)

Δ Mesh width of the computational fluid domain

Δx Mesh width in x direction

Δy Mesh width in y direction

Δz Mesh width in z direction

Δ^r Mesh width inside the refined patch

Δ_x^r Mesh width inside the refined patch in x direction

Δ_y^r Mesh width inside the refined patch in y direction

Δ_z^r Mesh width inside the refined patch in z direction

$\mathbf{x}_{eu}$ Position vector in Eulerian mesh

x streamwise direction/coordinate

y Lateral direction/coordinate

z Vertical direction/coordinate

x_w Chordwise direction/coordinate

y_w Spanwise direction/coordinate

z_w Direction perpendicular to the mean surface of the wing

$\mathbf{r}$ Distance between any fluid point and the origin of the non-inertial reference frame fixed to the wing

O' Origin of the non-inertial reference frame fixed to the wing

Δt Time step

ΔV Volume associated to a Lagrangian point

δ_Δ Regularized delta function

κ Unidimensional, continuous function used by the regularized delta function

$\mathbf{X}_l$ Position vector in Lagrangian mesh

$\mathbf{x}_P$ Position vector from the origin of the inertial reference frame to any point of the wing

Re Reynolds number

St Strouhal number

Ro Rossby number

k Reduced frequency

$\mathbf{f}$ Force per unit area on the surface of the wing

$\mathbf{f}_{n*}$ Normal force per unit area on the surface of the wing

$\mathbf{f}_n$ Normal force per unit area on the surface of the wing (after removing the ambient pressure)

$\mathbf{f}_\tau$ Tangential force per unit area on the surface of the wing

C_x Net force coefficient in the streamwise (x) direction

C_z Net force coefficient in the vertical (z) direction

C_{My} Pitching moment coefficient

C_x^n Contribution from the normal force to C_x

C_z^n Contribution from the normal force to C_z

C_x^τ Contribution from the tangential force to C_x

$\boldsymbol{F}$ Total aerodynamic force on an airfoil or wing section

c_l Lift coefficient on an airfoil or wing section

c_{tot} Total force coefficient on an airfoil or wing section

c_τ Tangential force coefficient

c_x^τ Streamwise contribution of the tangential force coefficient

c_n Normal force coefficient

c_z^n Vertical contribution of the normal force coefficient

$\mathbf{e}_x$ Unit vector in the streamwise (x) direction

$\mathbf{e}_z$ Unit vector in the vertical (z) direction

$\mathbf{e}_{y_w}$ Unit vector in the spanwise (y_w) direction

$\mathbf{e}_{z_w}$ Unit vector in a direction perpendicular to the mean surface of the wing (z_w)

$\mathbf{x}_{w,s}^k$ Position of the k-th point of the vortex skeleton

$x_{w,s}^k$ Chordwise position of the k-th point of the vortex skeleton

$y_{w,s}^k$ Spanwise position of the k-th point of the vortex skeleton

$z_{w,s}^k$ Position of the k-th point of the vortex skeleton in the direction perpendicular to the mean surface of wing

φ_s^k Physical quantities of the LEV associated to the k-th point of the vortex skeleton

Γ_s^k Circulation of the LEV associated to the k-th point of the vortex skeleton

V_s^k Volume associated to the k-th point of the vortex skeleton

$\mathbf{n}_s^k$ Direction of the LEV at the k-th point of the vortex skeleton

θ_{th} Deviation angle allowed between $\mathbf{e}_{y_w}$ and the projection of $\mathbf{n}_s^k$ onto an $x_w - y_w$ plane

H Width of the spanwise bins

$\mathbf{x}_{w,c}$ Position of the vortex core

$x_{w,c}$ Chordwise position of the vortex core

$z_{w,c}$ Vertical position of the vortex core

φ_c Physical quantities associated to the LEV core

Γ_c Circulation of the LEV

p_c Pressure inside the LEV

ω_c Relative vorticity of the LEV along the core direction

u_c Relative velocity inside the LEV along the core direction

$\mathbf{n}_c$ Direction of the LEV core

$\boldsymbol{\omega}'_c$ Relative vorticity associated to the LEV core

$\mathbf{u}'_\mathbf{c}$ Relative velocity associated to the LEV core

σ Standard deviation

Operators

This glossary contains the operators used during the document. To illustrate some of the operators, they have been applied on the variable φ.

∇ Nabla operator

∇^2 Laplace operator

$\langle\varphi\rangle$ Averaging operator. The average is performed along the wing span

$\overline{\varphi}$ Averaging operator. The average is performed in time during the downstroke

φ^{rms} Root-mean-square

$|\varphi|$ Absolute value

$\|\varphi\|$ Module

Acronyms

MAV micro air vehicle

FWMAV flapping wing micro air vehicle

TEV trailing edge vortex

LEV leading edge vortex

TiV tip vortex

2D two dimensional

3D three dimensional

AR aspect ratio

RHS right-hand side

R-K Runge-Kutta

DNS direct numerical simulation

TUCAN Two(Three)-Dimensional Unsteady Code for Aerodynamics in Nature

IBM immersed boundary method

I/O input/output

MPI Message Passing Interface

HDF5 Hierarchical Data Format version 5

CFL Courant Fredrich Levy number

UPM unsteady panel method

rms root-mean-squared

p.d.f. Probability density function

UC3M Universidad Carlos III de Madrid

UCSD University of California San Diego

CHAPTER
ONE

Introduction

1.1 Motivation

In recent years there has been a growing interest in the development of micro air vehicles (MAVs) [Pines and Bohorquez, 2006]. These small vehicles, with sizes of the order of $\lesssim$ 15cm and weights of the order of $\lesssim$ 200g, have multitude of applications such as surveillance, reconnaissance or monitoring of hazardous environments, specially in confined spaces which are difficult to access with larger vehicles.

Depending on the aerodynamic design, MAVs can be classified in three main groups: fixed wing, rotary wing and flapping wing vehicles. There are several practical implementations of fixed wing and rotary wing MAVs, like the Flyswatter (fixed wing) and the Heli-Rocket (rotary wing) of Morris [1997], or the Black Widow (fixed wing) of Grasmeyer and Keennon [2001]. However, the performance of fixed and rotary wing MAVs is limited by the degradation of the aerodynamic performance of fixed/rotary wings at low Reynolds numbers [Pines and Bohorquez, 2006].

This limitation has pushed researchers to evaluate the third configuration, the flapping wing MAV (FWMAV), inspired by the way insects, small birds and bats fly. The hope is that FWMAVs should achieve unprecedented aerodynamic performance, manoeuvrability and versatility, similar to that observed in natural fliers. The idea is to take advantage of the unconventional aerodynamic mechanisms that appear in flapping wings: delayed stall of the leading edge vortex (LEV), rapid pitch up, wake capture and clap and fling [Ellington, 1984, Sane, 2003]. Again, there are several practical implementations of FWMAVs [Gerdes et al., 2012] but probably one of the most successful is the DelFly family developed in the Delft University of Technology [De Croon et al., 2016].

However, the design of FWMAVs is still relatively far from the efficiency and accuracy of the design of fixed wing or rotary wing MAVs. Part of the problem is that the variety of manoeuvres, wing kinematics and geometric parameters is so vast that there are no simple and reliable models for the aerodynamic forces covering this huge parametric space. Probably the reason behind is that, at present, the acquired knowledge is mostly of a qualitative nature. For example, it is well known that an attached LEV provides

additional lift [Ellington et al., 1996, Dickinson et al., 1999]. However, it is difficult to predict exactly how much additional lift is obtained as a function of the large number of parameters involved in flapping flight. Furthermore, for a general flapping motion, the LEV might present a non-trivial three dimensional (3D) structure, whose precise geometry, location and intensity is very difficult to predict a priori.

Improving our understanding of the unsteady aerodynamics associated to flapping wings is one of the main objective of the present thesis.

1.2 State of the art

As mentioned above, one of the problems associated to flapping wings is that the parametric space for the wing geometry and kinematics is extremely large. Even when the wing geometry (i.e., planform, span, wing surface, geometric and aerodynamic twist, thickness distribution, etc.) and its structural properties (i.e., flexural and torsional rigidity, mass distribution, inertia, etc.) are fixed, the definition of the kinematics of the wing offers a virtually infinite parametric space: orientation of the stroke plane with respect to the direction of flight, motion within the stroke plane (translation and/or rotation), deviations of the wing motion outside of the stroke plane, rotation of the wing around a spanwise axis (pitching), as well as the amplitude, frequency and relative phase shifts of all these motions.

Since the problem is so complex, many studies have explored the simplified configuration of a two dimensional (2D) airfoil in heaving (vertical translation) and/or pitching (in-plane rotation) motion [Anderson et al., 1998, Lewin and Haj-Hariri, 2003, Read et al., 2003, Baik et al., 2012, Choi et al., 2015, Martín-Alcántara et al., 2015, Moriche et al., 2017]. Such studies have shown and quantified the role that the vortical structures generated near the leading edge (leading edge vortices or LEVs) and near the trailing edge (trailing edge vortices or TEVs) play in the process of force generation. These LEVs and TEVs have a strong influence on the aerodynamic forces while they remain sufficiently close to the airfoil [Chang, 1992], resulting in optimal aerodynamic performance for Strouhal numbers (St) or the order $St \approx 0.1 - 0.2$, and a combination of heaving and pitching with a phase shift of about 90° [Martín-Alcántara et al., 2015, Moriche et al., 2017].

It should be noted that the simplified configuration of the 2D airfoil corresponds to the motion of an *infinite* aspect ratio wing, where all 3D effects (both due to intrinsic flow instabilities and due to the finite wing effects) are missing. Moreover, all sections of the corresponding *infinite* aspect ratio wing have the same vertical displacement. However, this is not the case for natural flyers or FWMAVs, which flap their wings so that the amplitude of the motion increases from the root of the wing (i.e., the inboard wing tip) to the outboard wing tip.

There are multitude of studies analyzing the aerodynamic performance and flow characteristics around flapping wings, both in hover and forward flight. In particular, flapping wings in forward flight have been studied by several authors, simulating both idealized configurations [Dong et al., 2006, Guerrero, 2010, Bos et al., 2013, Gursul and Cleaver, 2018] as well as realistic configurations corresponding to insects [Nagai et al., 2009, Yokoyama et al., 2013, Zheng et al., 2013, Liu et al., 2016] or bats [Viswanath et al., 2014]. While the emphasis in most of these studies lies in the characterization of the aerodynamic forces for the particular geometry or kinematics selected, few works analyze systematically the effect on the forces of varying kinematics or geometries. One of the exceptions is the work of Nagai et al. [2009] who reported experiments and numerical simulations of an insect-like flapping wing, analyzing the effect on the aerodynamic forces of the position of the stroke plane and of the advance ratio. Another comprehensive study was performed by Bos et al. [2013]. They studied the effect of the radius of flapping motion (R) on the aerodynamic forces, presenting an extensive database of cases in hover and a limited database of cases in forward flight. Their results show that both in hover and in forward flight, the aerodynamic force coefficients decrease as the radius of flapping motion increases, as a result of the stabilizing effect of the Coriolis and centripetal accelerations of the LEV. Also, Guerrero [2010] performed numerical simulations of a flapping, rectangular wing in forward flight. The author considered both heaving motion and a flapping motion with respect to the wing root at a Reynolds number (Re) of 250 based on the flight speed (u_∞) and the wing chord (c). After analyzing the aerodynamic forces and flow visualizations, the author concluded that the heaving case produces larger forces and vortices than the flapping case, in apparent contradiction with the limited results reported by Bos et al. [2013] for forward flight.

Contrary to flapping wings, a systematic analysis of the effect of kinematics (i.e., radius of the motion) and geometry (i.e., aspect ratio, AR) can be found in the literature of revolving wings [Dickson and Dickinson, 2004, Lentink and Dickinson, 2009, Jardin and David, 2014, Lee et al., 2016]. It is important to note that compared to the kinematics of flapping wings, revolving wings only move in one direction (i.e., there is no stroke reversal) without any incoming free-stream velocity. The results in the literature show that in revolving wings the effect of the centripetal and Coriolis acceleration is to stabilize the LEV, producing an increase in lift as the radius of flapping motion decreases. This effect is usually quantified with the Rossby number (Ro), which measures the ratio between the inertial force and the Coriolis force.

Overall, the literature cited in the previous paragraphs tends to agree in the central role of the Ro in the generation of aerodynamic forces in flapping wings. However, it is not clear how close to the wing needs the LEV to be to have a positive effect on the aerodynamic performance of the wing. Note that for most of the kinematics discussed so far, the LEV is shed into the wake at the end of the stroke, and different kinematics

produce LEVs of different sizes and positions. The quantification of these effects require a method capable to identify and track the leading edge in complex 3D geometries.

Several approaches are documented in the literature to identify LEVs in flapping wings. For instance, Visbal [Visbal, 2011a,b] used pressure contours to qualitatively identify vortices as regions of low pressure. In Visbal et al. [2013], some specific features of the LEV (e.g. the motion of the legs of the arch-vortex) were determined by means of the phase-averaged surface pressure. Other authors [Birch and Dickinson, 2003, Taira and Colonius, 2009, Jones and Babinsky, 2011, Jardin and David, 2014, Calderon et al., 2014] employ the vorticity field to identify the vortices. Thus, regions with high vorticity values are considered vortices, although it is important to note that this magnitude is also high in shear layers. There are other local approaches based on the velocity gradient tensor that do not present this limitation. Among others, the Q [Hunt et al., 1988] and the λ_2 [Jeong and Hussain, 1995] criteria are extensively used in the unsteady aerodynamics field to identify vortical structures [Taira and Colonius, 2009, Kweon and Choi, 2010, Visbal, 2011a,b, Jardin et al., 2012, Visbal et al., 2013, Jantzen et al., 2013, Harbig et al., 2013, Jantzen et al., 2014, Harbig et al., 2014, Jardin and David, 2014, Kolomenskiy et al., 2014, Jardin, 2017]. All these approaches have been used to explain qualitatively the flow features observed around the wing, such as the LEV, the tip vortices (TiVs) and the trailing edge vortex (TEV).

In order to characterize the effect of the LEV on the aerodynamic forces generated by flapping wings, it is important to provide quantitative information in addition to qualitative one. This includes for example the precise determination of the relative position of the LEV with respect to the wing and the quantification of the LEV intensity. Several authors have attempted to tackle this issue. Birch et al. [2004] performed experiments on revolving wings at constant angular velocity, observing a stable LEV on the wing. They integrated the vorticity over wing cross-sections to estimate the local circulation around the wing. Jones and Babinsky [2011] performed a similar experiment at a somewhat higher Re than Birch et al. [2004]. They identified the vortices using the vortex identification method of Graftieaux et al. [2001]. They studied the geometry and location of the LEV as a function of time by analyzing several wing cross-sections. The growth of the LEV at a given cross-section was quantified by computing the local circulation as a function of time. Jardin and David [2014] performed direct numerical simulations of flow over a wing undergoing different maneuvers. They characterized the LEV by analyzing the midspan plane and computing the local circulation as a function of the distance traveled by the wing. Finally, Jantzen et al. [2014] performed direct numerical simulations and experiments of flat-plate rectangular wings undergoing pitching maneuvers about the leading edge. They tracked the LEV along the midspan plane employing the vortex identification method of Graftieaux et al. [2001]. They also evaluated the vortex strength by integrating the spanwise vorticity inside the vortex core bound-

ary. These results were limited to a 2D plane, but the flow visualizations showed that the LEV was a complex 3D structure, emphasizing the need of a fully three-dimensional study of the LEV position and evolution.

1.3 Objectives

The fundamental objective of this thesis is to contribute to the understanding of the 3D aerodynamics of flapping wings in forward flight at low-Reynolds numbers.

Particularly, our interest is focused on the aerodynamic forces on finite wings, and the flow structures around them, due to a transition from a heaving motion to a flapping motion.

In order to study this transition, several direct numerical simulation (DNS) of finite wings in forward flight have been carried out varying smoothly the radius of flapping motion. Since the wings are finite, two different values of AR are studied to evaluate how the 3D geometry affects the aerodynamic forces and the flow structures during the transition.

Among the flow structures that appear around the wings, this thesis focuses mainly on the effect of the leading edge vortex on the aerodynamic forces. This effect is studied both qualitatively and quantitatively. In order to be able to perform such analyses, a secondary objective of the thesis is to develop a methodology capable to provide a quantitative 3D description of the LEV.

1.4 Structure of the document

The thesis is structured as follows. The numerical methods used to perform the DNS is presented in chapter 2. The description of the problem studied and the details of the computational setup of the simulations that make up the database analyzed are provided in chapter 3. In chapter 4 the results of database cases with wings of $AR = 2$ are discussed. After that, the methodology developed to provide a quantitative description of the LEV is described in detail in chapter 5. Then, the analysis of the database cases with wings of $AR = 4$ and their comparison with the cases with wings of $AR = 2$ is discussed in chapter 6. Finally, the conclusions and some propositions for future work are presented in chapter 7.

CHAPTER
TWO

Methodology

In this chapter, first the code used to perform the DNS is described in section 2.1. Then, the modifications implemented in the code to improve its overall performance are detailed in section 2.2. Subsequently, the improvements in performance obtained are measured and discussed in section 2.3. Finally, the validation of code is presented in section 2.4.

2.1 TUCAN

The code used to carry out the simulations of this thesis is TUCAN (Three-Dimensional Unsteady Code for Aerodynamics in Nature), a parallel in-house code written in Fortran 90. TUCAN solves the Navier-Stokes equations for an incompressible flow and allows to simulate the presence of submerged rigid bodies of arbitrary shape and motion. The equations that are solved in TUCAN are

$$\nabla \cdot \mathbf{u} = 0, \tag{2.1a}$$

$$\frac{\partial \mathbf{u}}{\partial t} + (\mathbf{u} \cdot \nabla)\,\mathbf{u} = -\frac{1}{\rho}\nabla p - \nu \nabla^2 \mathbf{u} + \mathbf{f}_{\mathrm{IBM}}, \tag{2.1b}$$

$$\mathbf{u} = \mathbf{U} \quad \text{at the surface of the body} \tag{2.1c}$$

where $\mathbf{u}$ is the flow velocity, ρ the density of the fluid, p the pressure, ν the kinematic viscosity and $\mathbf{U}$ the velocity of the bodies immersed in the fluid. Since the Navier-Stokes equations are solved for a viscous fluid, a no-slip condition is imposed at the surface of the bodies (equation 2.1c) by means of the volume force $\mathbf{f}_{\mathrm{IBM}}$ added in equation (2.1b). Furthermore, initial conditions and conditions at the boundaries of the domain are required for $\mathbf{u}$ and p to close the problem. The different boundary conditions implemented in TUCAN will be discussed later in this section.

The 3D computational domain of the fluid is discretized with a structured, uniform, staggered Cartesian grid. On these grids, scalar variables such as the pressure are stored in the center of the cells, while the velocity components are placed at the center of the faces of the cells (see the illustration of Figure 2.1*a*).

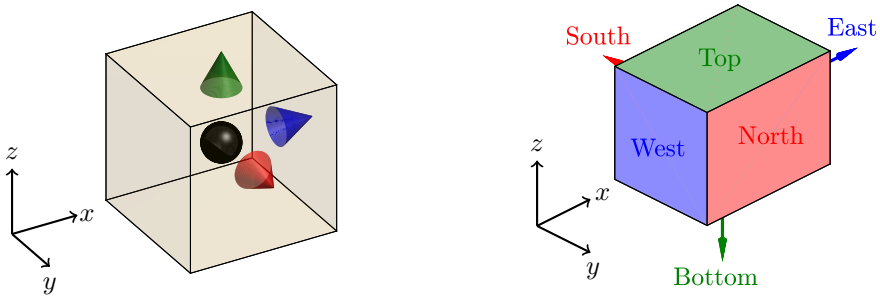

Figure 2.1: *a*) Sketch of the cell of a computational staggered mesh. The pressure point is represented with a black sphere and the streamwise, spanwise and vertical velocities points are depicted with a blue, red and green cone, respectively. *b*) Sketch of the physical domain with its corresponding boundaries.

On the other hand, the submerged bodies are discretized in a Lagrangian grid, which consists of evenly distributed points along the surface of each body. For the 3D simulations carried out in this thesis, the Lagrangian grids have been generated in preprocessing with Gmsh (Geuzaine and Remacle [2009]).

The equations (2.1) are solved using the projection method described in Brown et al. [2001] to enforce the continuity equation. This method is based on the decomposition of $\mathbf{u}$ in a non divergence-free term ($\mathbf{u}^*$) and an irrotational term equal to the gradient of a potential ϕ, which is going to be called pseudo-pressure in the manuscript. The time integration is performed with the three-stages low-storage semi-implicit Runge-Kutta (R-K) time scheme proposed by Rai and Moin [1991], the spatial derivatives are evaluated by means of second-order, central finite-differences and the presence of submerged bodies is modelled using the direct forcing immersed boundary method (IBM) proposed by Uhlmann [2005].

In this IBM, an explicit estimation of the flow velocity ($\mathbf{u}^e$) is used to calculate the volume force ($\mathbf{f}_{\text{IBM}}$) of the momentum equation (2.1b) at each sub-step of the R-K. First, in order to obtain $\mathbf{f}_{\text{IBM}}$, it is necessary to interpolate $\mathbf{u}^e$ from the Eulerian mesh (fluid) to $\mathbf{U}^e$ in the Lagrangian mesh (bodies). Subsequently, the forcing term ($\mathbf{F}_{\text{IBM}}$) is calculated in the Lagrangian mesh so that the desired velocity ($\mathbf{U}^d$) is imposed at each Lagrangian point, satisfying the no-slip condition. Then, $\mathbf{F}_{\text{IBM}}$ is spread from the Lagrangian mesh to the Eulerian mesh to finally obtain $\mathbf{f}_{\text{IBM}}$. The interpolations performed to transfer the information between both meshes are calculated with regularized delta functions.

These functions discretize the Dirac's delta function in the following form:

$$\delta_\Delta = \frac{1}{\Delta^3}\kappa\left(\frac{d_x}{\Delta}\right)\kappa\left(\frac{d_y}{\Delta}\right)\kappa\left(\frac{d_z}{\Delta}\right), \tag{2.2}$$

where Δ is the Eulerian mesh width, which must be equal in x, y and z directions, d_x, d_y and d_z are the distances between an Eulerian point ($\mathbf{x}_{eu}$) and a Lagrangian point ($\mathbf{X}_L$) in x, y and z directions respectively and κ is a unidimensional, continuous function. Two different κ functions are implemented in TUCAN, the one used by Peskin [2002] and the one proposed by Roma et al. [1999]. The main difference between them is found in the number of grid points that are influenced by δ_Δ in each spatial direction, which is 3 and 4 for the first and the second implementation respectively. For further details of the IBM implementation, refer to Uhlmann [2005].

After discretizing the flow equations, including the fluid-solid interaction, the k-th Runge-Kutta sub-step implemented in TUCAN is

$$\mathbf{u}^e = \mathbf{u}^{k-1} + \Delta t\left(\frac{\alpha_k+\beta_k}{Re}\nabla^2\mathbf{u}^{k-1} - (\alpha_k+\beta_k)\nabla p^{k-1} - \gamma_k\left[(\mathbf{u}\cdot\nabla)\,\mathbf{u}\right]^{k-1} - \xi_k\left[(\mathbf{u}\cdot\nabla)\,\mathbf{u}\right]^{k-2}\right) \tag{2.3a}$$

$$\mathbf{U}^e\left(\mathbf{X}_L^i\right) = \sum_{j=1}^{n_{eu}}\mathbf{u}^e\left(\mathbf{x}_{eu}^j\right)\delta_\Delta\left(\mathbf{x}_{eu}^j - \mathbf{X}_{LAG}^i\right)\Delta^3, \quad \text{for } i\in[1,N_L] \tag{2.3b}$$

$$\mathbf{F}_{\text{IBM}}\left(\mathbf{X}_L^i\right) = \frac{\mathbf{U}^d\left(\mathbf{X}_L^i\right) - \mathbf{U}^e\left(\mathbf{X}_L^i\right)}{\Delta t}, \quad \text{for } i\in[1,N_L] \tag{2.3c}$$

$$\mathbf{f}_{\text{IBM}}\left(\mathbf{x}_{eu}^i\right) = \sum_{j=1}^{N_L}\mathbf{F}_{\text{IBM}}\left(\mathbf{X}_L^j\right)\delta_\Delta\left(\mathbf{X}_L^j - \mathbf{x}_{eu}^i\right)\Delta V, \quad \text{for } i\in[1,n_{eu}] \tag{2.3d}$$

$$\nabla^2\mathbf{u}^* - \frac{Re}{\beta_k\Delta t}\mathbf{u}^* = -\frac{Re}{\beta_k\Delta t}\left(\mathbf{u}^e + \Delta t\mathbf{f}_{\text{IBM}}\right) + Re\nabla^2\mathbf{u}^{k-1} \tag{2.3e}$$

$$\nabla^2\phi^k = \frac{\nabla\cdot\mathbf{u}^*}{(\alpha_k+\beta_k)\,\Delta t} \tag{2.3f}$$

$$\mathbf{u}^k = \mathbf{u}^* - (\alpha_k+\beta_k)\,\Delta t\nabla\phi^k \tag{2.3g}$$

$$p^k = p^{k-1} + \phi^k - \frac{\beta_k\Delta t}{Re}\nabla^2\phi^k \tag{2.3h}$$

where α_k, β_k, γ_k and ξ_k are the coefficients of the R-K scheme (see Table 2.1), Δt is the time between steps, n_{eu} is the number of Eulerian points, N_L the number of Lagrangian points and ΔV is the volume associated to each Lagrangian point. Equations (2.3) have been non-dimensionalized with a velocity U_c, a pressure $\rho {U_c}^2$ and a length L_c, yielding a Reynolds number $Re = U_c L_c/\nu$. In the simulations solved in this work, L_c is equal to the chord of the wing (c) and U_c is the flight speed of the body (u_∞) and therefore $Re = u_\infty c/\nu$. Note that when there are no solids immersed in the fluid, the term $\mathbf{f}_{\text{IBM}}$ vanishes from equation (2.1b) and the no-slip condition (equation 2.1c) must

Stage	α	β	γ	ξ
1	4/15	4/15	8/15	0
2	1/15	1/15	5/12	−17/60
3	1/6	1/6	3/4	−5/12

Table 2.1: Coefficients of the Runge-Kutta scheme used in TUCAN.

not be fulfilled at any surface. In such case, TUCAN becomes a simple Navier-Stokes equations solver.

In a 3D simulation, boundary conditions must be imposed for the velocity components and the pressure at the six boundaries of the physical domain (see Figure 2.1*b*). At each one of these boundaries TUCAN allows Dirichlet, Neumann and periodic boundary conditions. Moreover, an exit boundary condition given by

$$\partial_t \mathbf{u} + u_a \partial_x \mathbf{u} = 0, \tag{2.4}$$

can be imposed at the east boundary, where the advective velocity, u_a, is considered as a constant. This equation is solved explicitly as the non-linear terms in the Navier-Stokes equations.

Since in the staggered grid there are different meshes for each velocity component and for the pressure, the boundary conditions are imposed by means of ghost points, which are added beyond the physical boundaries (green lines in Figure 2.2). The setting of the boundary conditions using ghost points is illustrated in Figure 2.2 through some examples in an x-y section of the staggered grid. For instance, to impose a Dirichlet boundary condition for the x velocity component (▶) at the south boundary ($y = 0$), the pairs of points framed in the magenta rectangles of Figure 2.2*a* would be required. However, to impose the same boundary condition for the y velocity component (▲) at the north boundary, only the points that laid on the physical domain (highlighted with a cyan rectangle in Figure 2.2*a*) would be used. Furthermore, when a periodic boundary condition is imposed in one direction, an additional point is required in the grid of the velocity component which correspond to that direction. Thus, the grid of that velocity component would have the same number of points than the pressure grid. In Figure 2.2*b*, an example of the same x-y section is shown for a case where periodic boundary conditions are set in both x and y directions. The additional point in each direction and the new position of the ghost points are displayed with a pair of magenta (cyan) rectangles in Figure 2.2*b*.

The parallelization of TUCAN is performed by means of a block domain decomposition. All the Eulerian grids (pressure and velocity components) are split into a number of smaller domain blocks (parallelepipeds) which is equal to the number of processors

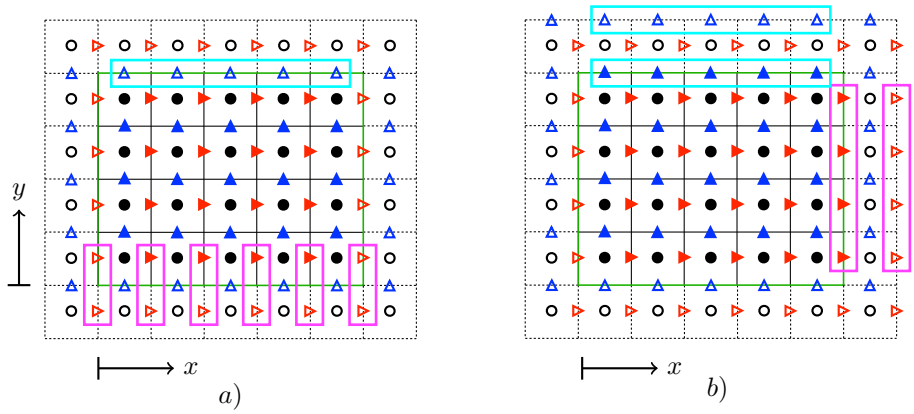

Figure 2.2: x-y section of the staggered grid used by TUCAN to impose a) Dirichlet, Neumann and exit boundary conditions and b) periodic boundary conditions. Pressure points are represented by (●) and streamwise and vertical velocity components are depicted with (▲) and (▶) respectively. Points of the physical domain are shown with filled symbols and ghost points with empty symbols. The physical domain is delimited with a green line (———).

(N_P). The computational size (i.e., the number of points) of these blocks is almost equal for each processor so that the workload of each processor is similar. The block domain decomposition is carried out in 2D in TUCAN. The domain is divided in the y and z directions, hence all processors contains the whole information along the x direction.

Since each processor only have the information of the variables of each corresponding block, it is necessary to share some information with the other processors. Particularly, the values of the variables located at the interfaces (i.e. surfaces in 3D grids) of the blocks are communicated between neighboring processors. These communications are done using Message Passing Interface (MPI), which is a message-passing standard designed to work on different parallel computing architectures.

In TUCAN, two different linear systems are solved at each sub-step, a Helmholtz problem (equation 2.3e) for each component of the velocity and a Poisson problem (equation 2.3f) for the pseudo-pressure. In order to solve these linear systems in parallel, TUCAN uses HYPRE [2018 August] library, which provides a large variety of high performance preconditioners and solvers to solve linear systems on massively parallel computers. After testing several solvers of HYPRE, a biconjugate gradient stabilized solver (BiCGSTAB) preconditioned with a parallel semicoarsening multigrid solver (PFMG) proved to be the faster to solve the Poisson problem. On the other hand, the Helmholtz problem of each velocity component is solved with a preconditioned conjugate gradient solver (PCG) due to its robustness.

The results obtained by TUCAN are stored in two different output files. The first one, saved with the extension .raw, includes statistics of the flow and small size data sets such as the global forces and moments on the bodies, information of the simulation status, the performance of the linear solver, the motion of the bodies, etc. Since the size of these files is between kiloBytes (kB) and MegaBytes (MB), the information is storaged at each time step and is written to disk every $O(10^2)$ time steps. The second output file includes the same parameters of the raw files in addition to the inputs parameters of the simulations, the forces calculated at each Lagrangion mesh point, the Eulerian grids and the buffers of the pressure and velocity components. This file, named frame file and saved with the extension .frame, is only storaged and written to disk every $O(10^2)$ time steps due to its large size. Furthermore, TUCAN also needs to read large size data sets from disk to restart simulations. Since all these input/output (I/O) tasks must be carried out effectively so that the performance of the code does not drop, TUCAN uses Hierarchical Data Format version 5 (HDF5) libraries which handle the MPI standard, enabling collective I/O.

TUCAN has been extensively validated, and a more detailed description of the implementation of TUCAN can be found in Moriche [2017].

2.2 TUCANREF

Despite the good performance shown by TUCAN, there is still room to improve it. For instance, in problems with one body (or several bodies) placed in a small region of the computational domain, TUCAN solves the whole flow with a uniform grid. Thus, the resolution used to solve the flow near the body is equal than in regions far from it, where the flow barely changes and a lower resolution could be used. Moreover, for problems with large domains in the x direction, the large size of the communications between adjacent processors (i.e., the surface of the interface between them) could produce an excessive memory and communications workload.

In order to avoid these problems, a non-uniform grid was implemented in TUCANREF. The staggered arrangement presents some differences between uniform and non-uniform grids. As indicated by Vasilyev [2000], in non-uniform meshes the locations of the velocity and pressure points are ambiguous, since they can be determined as the geometric volume and face centers either in physical or computational space. Furthermore, when solving the incompressible Navier-Stokes equations in these meshes, some complications arise in the conservation properties of high order finite difference schemes.

in these meshes some complications arise in the conservation properties of high order finite difference schemes when solving the incompressible Navier-Stokes equations. The scheme implemented in TUCANREF is the second order accurate finite difference scheme described in Vasilyev [2000]. This scheme achieves mass and momentum conservation

discretizing the convective term in divergence form and using simple linear interpolations to obtain the advecting velocity in this term. Besides, the discrete continuity equation is centered at the cell center and the three components of the momentum equation are evaluated at the staggered locations, as in the scheme of TUCAN for uniform grids.

In the non-uniform meshes, three different possible regions may appear; refined regions, regions where the element size grows or decreases, and coarse regions. The distance between grid points in the first regions is denoted by Δ_x^r, Δ_y^r and Δ_z^r in the streamwise, vertical and spanwise direction, respectively. To solve problems with immersed bodies, this distance must be equal in the three directions (i.e., $\Delta^r = \Delta_x^r = \Delta_y^r = \Delta_z^r$). Thus, when bodies are immersed into the fluid, refined regions must be placed around those objects. The growth or decrease of the element size in the second regions is controlled by the stretch factor, ε. Last, the maximum size of the element in the third regions (coarse regions) is defined by the ratio between the maximum and minimum grid width, r, hence $\Delta_{\max} = r\Delta^r$.

On the other hand, regarding the possible overhead produced in the communication process due to large computational domains in the x directions, we decided to extend the block decomposition to 3D. Note that in block decomposition parallelization the communications can be reduced minimizing the surfaces of the interfaces that are communicated between the processors with respect to the volume of their blocks. In the case of TUCANREF, where the blocks are parallelepipeds, this would be achieved splitting the domain in blocks as similar as possible as cubes. This possibility is enabled with the 3D block decomposition.

Finally, a passive scalars solver was also implemented in TUCANREF. This feature was used during a short visit to University of California San Diego (UCSD) (june-august 2016) to analyze the 3D fluid dynamics of the blood in the left atrium. Simulations with specific patient geometries were performed to investigate the effect of atrial fibrillation on the blood stasis [Flores et al., 2016].

2.3 Performance

Section 2.2 detailed the modifications implemented in TUCAN to improve the performance of the code in terms of CPU-time and memory/storage requirements. In this section, the improvements on both aspects are evaluated and compared with the previous version of the code.

Among the tasks carried out by TUCAN during each time step, solving the linear system of the pseudo-pressure (ϕ) is the most time consuming. This can be seen in Figure 2.3, where the percentage of time spent on each task (t_{task}) respect to the total time of a simulation (t_{tot}) run with TUCAN is broken down. The data shown in the Figure corresponds to a typical test case with $O(10^8)$ grid points, run in 144 processors

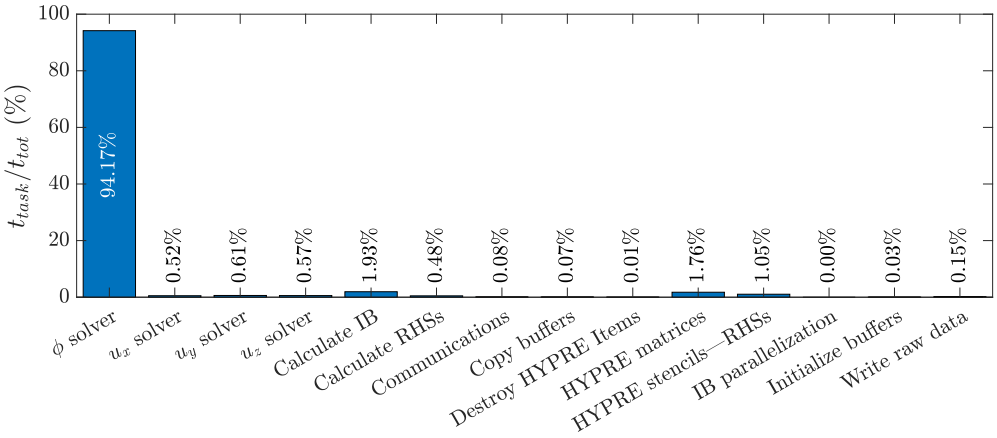

Figure 2.3: Time spent by TUCAN at each task respect the total time (in %) for a simulation of the flow with $Re = 5000$ around a 3D wing with a fixed angle of attack. The computation domain has $156M$ of grid points. The simulation is run with 144 processors.

in the local cluster of the Bioengineering and Aerospace Engineering Department of the Universidad Carlos III de Madrid (UC3M). Similar results are obtained for other cases, like the ones discussed below. In particular, solving the Poisson problem accounts for almost 95% of the total computational time, about 60 times more than the time required to solve the Helmholtz problems for the velocity components.

Note that, Figure 2.3 does not include all the I/O time. Only the time to sample and write the statistics (raw file) is included, while the time necessary to write the output file which contains the flow variables (frame file) is not. It should be noted that since the I/O tasks are performed in parallel using HDF5, which only have little overhead over MPI I/O, the additional time required to write the frame file is small. Besides, this time is only spent every $O(10^2)$ time steps.

A basic measurement of the computational performance of TUCAN is given by the unitary time t_u, which is defined as

$$t_u = \frac{t_{\phi\text{solver}} N_P}{N_S N_G} \tag{2.5}$$

where N_P is the number of processors used to perform the simulation, N_S is the number of steps run and N_G is the number of grid points used to discretize the computational domain. Note that, given that the computational time is dominated by the linear solver of the Poisson equation, only the time for this solver ($t_{\phi\text{solver}}$) is consider in equation (2.5).

In order to compare the performance of TUCAN/TUCANREF with uniform and non-uniform grids, it is important to consider that the behavior of the linear solvers of

HYPRE changes with the distribution of points in the grid. In simulations run with uniform grids, the number of iterations required to solve the linear systems keeps roughly constant at every sub-step of the R-K. However, the number of iterations required using non-uniform grids increases considerably with respect to the uniform grids, showing also a large variability between the different sub-steps of the R-K. Hence, in order to compare the computational time of simulations run with non-uniform grids and uniform grids, an equivalent unitary time (t_u^{eq}) is defined as

$$t_u^{eq} = \frac{t_{\phi\text{solver}} N_P}{N_S N_G^{uni}} \tag{2.6}$$

where N_G^{uni} is the number of grid points that would be required to discretize the computational domain using a uniform mesh with a grid width equal to the smallest grid width of the non-uniform mesh. Hence, t_u^{eq} weights in the gain of performance due to the reduction of grid points (i.e., smaller matrices), and the loss of performance due to the behavior of the linear solvers (i.e., increase in the number of iterations).

It is important to keep in mind that the solution introduced in the right-hand side (RHS) of the linear systems affects the iterative process of the solvers. Thus, in order to compare the performance of TUCAN with uniform and non-uniform grids, a similar problem to the one studied during the thesis has been solved. Particularly, the 3D flow around an infinite wing of chord c moving in forward flight. The cross-sections of the wing consist of NACA0012 airfoils and their angle of attack is fixed to $\alpha_e = 5°$. The Reynolds number of the simulations is defined as specified in chapter 2 and is equal to 5000. The infinite wing is simulated by imposing periodic boundary conditions at the lateral (y) boundaries. Along the streamwise (x) direction, an incoming uniform free stream and an exit (advective) boundary condition are imposed upstream and downstream of the wing respectively. Last, free slip boundary conditions are imposed at the top and bottom boundaries, i.e., at the domain limits of z direction.

Since the refinement of the non-uniform meshes affects the performance of the linear solvers, several simulations have been carried out varying the two parameters that control the growth of the grid width: the stretch factor (ε) and the ratio between the maximum and minimum grid width (r). The effect of both parameters on the performance of the code is studied in two different computational domains. The smallest one is defined between $[-5c, 12c]$, $\left[-16\Delta_y^r, 16\Delta_y^r\right]$ and $[-9c, 3c]$ in x, y and z directions respectively, where $\Delta_y^r = \Delta_x^r = \Delta_z^r = c/256$ is the smallest grid width. The largest domain is extended in x and z directions, yielding a domain of $25c$ in x direction ($x = [-8c, 17c]$) and $20c$ in z direction ($z = [-15c, 5c]$). The refined region is the same in all the simulations. It is defined so that all points of the wing lay within it, therefore it is located at $x = [-0.5c, 2c]$, $z = [-2.8c, 0.5c]$ and along the entire lateral direction. The refinement parameters and the total number of grid points (N_G) used in the simulations performed are presented in Table 2.2. The simulations are labeled with $S\#\#\text{-}\#\#$ and

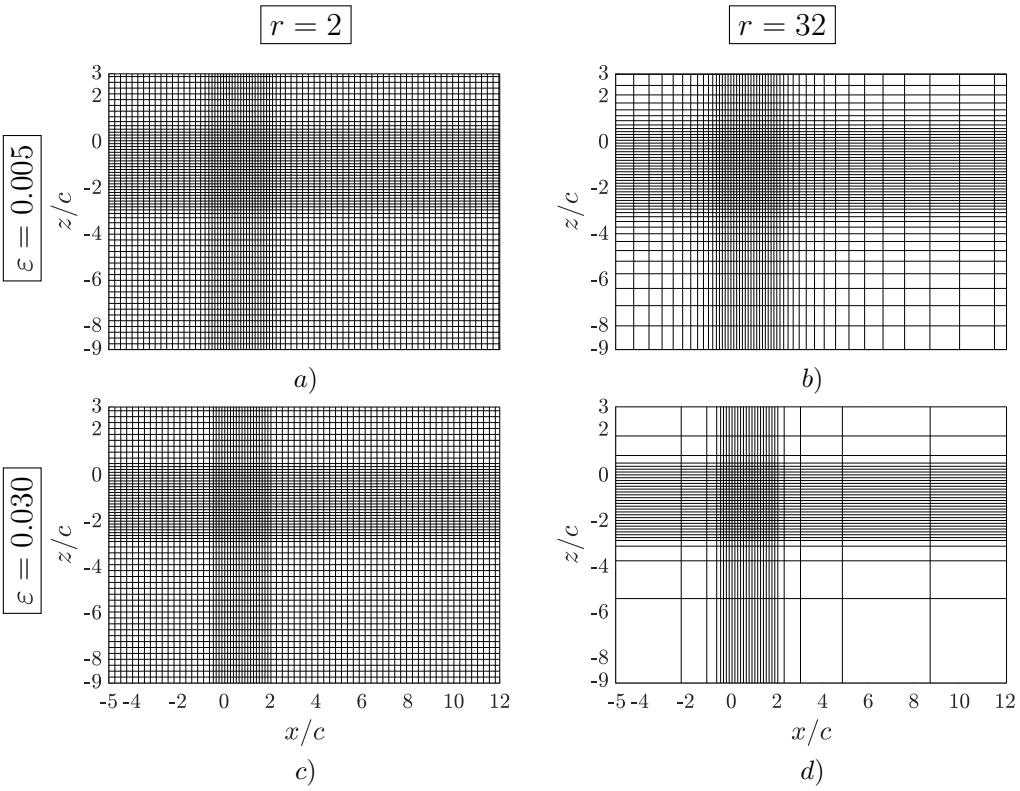

Figure 2.4: x-z view of the meshes used in simulations *a*) $S05$-02, *b*) $S05$-32, *c*) $S30$-02 and *d*) $S30$-32. In order to ease the visualization of the meshes, only 1 every 32 grid lines are shown in the streamwise and vertical directions.

L##-##, where the letter corresponds to the size of the domain (S for the smaller one and L for the larger one), the first two digits indicate the stretch factor (multiplied by 10^3) and the last ones the ratio between the maximum and minimum grid width.

The non-uniform x-z section of four meshes used in the small domain simulations are shown in Figure 2.4 to illustrate the differences between them. The grids of the cases with $r = 2$ (Figures 2.4*a* and 2.4*c*) are more alike than those with $r = 32$ (Figures 2.4*b* and 2.4*d*). It seems that for very small r values, like $r = 2$, the variation of the stretch factor is not translated into large changes in the mesh, since the region with linear stretching is relatively small and the coarse region is reached well before the boundaries. Consequently, the reduction on the number of grid points, N_G, between the meshes generated with $\varepsilon = 0.005$ and $\varepsilon = 0.03$ is smaller than 10% (see Table 2.2). Note, however, that even the case with the smaller refinement ($S05$-02) is able to reduce N_G respect to the uniform case (S_{uni}) by a factor of ~ 2.5.

Cases	ε	r	N_G (M)	size (MB)	Cases	ε	r	N_G (M)
S_{uni}	0.000	1	428	14562	-	-	-	-
S05-02	0.005	2	167	5673	L05-02	0.005	2	349
S10-02	0.010	2	160	5445	L10-02	0.010	2	339
S20-02	0.020	2	155	5284	L20-02	0.020	2	330
S30-02	0.030	2	152	5189	L30-02	0.030	2	323
S05-04	0.005	4	96	3278	L05-04	0.005	4	161
S10-04	0.010	4	82	2801	L10-04	0.010	4	143
S20-04	0.020	4	75	2561	L20-04	0.020	4	132
S30-04	0.030	4	72	2468	L30-04	0.030	4	128
S05-08	0.005	8	79	2705	L05-08	0.005	8	109
S10-08	0.010	8	58	1991	L10-08	0.010	8	82
S20-08	0.020	8	48	1645	L20-08	0.020	8	70
S30-08	0.030	8	45	1530	L30-08	0.030	8	66
S05-16	0.005	16	78	2643	L05-16	0.005	16	98
S10-16	0.010	16	52	1787	L10-16	0.010	16	64
S20-16	0.020	16	39	1339	L20-16	0.020	16	49
S30-16	0.030	16	35	1192	L30-16	0.030	16	44
S05-32	0.005	32	78	2643	L05-32	0.005	32	98
S10-32	0.010	32	52	1767	L10-32	0.010	32	60
S20-32	0.020	32	37	1261	L20-32	0.020	32	42
S30-32	0.030	32	32	1085	L30-32	0.030	32	35

Table 2.2: Parameters and relevant information of simulations carried out for the performance analysis. ε is the stretch factor, r is the ratio between the maximum and minimum grid width and N_G is the total number of points of the computational domain. The size of the computational domain of the cases is denoted with S for the smaller domain and L for the larger one. For the cases with small domain, the size of the output file which contains the flow field variables (frame file) is included in MegaBytes (MB).

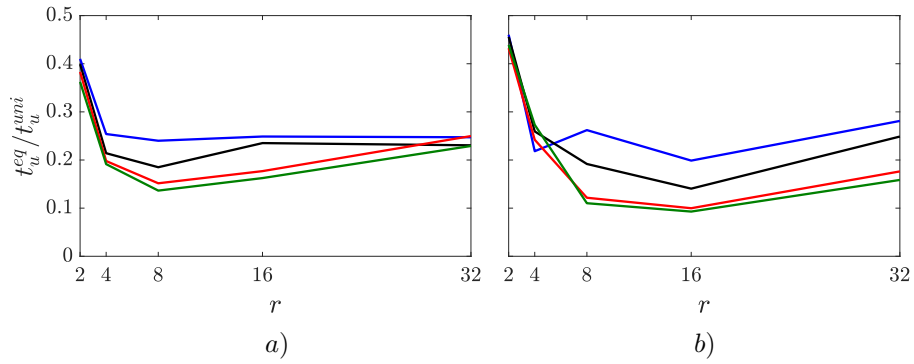

Figure 2.5: Equivalent unitary time (t_u^{eq}) as a function of the ratio between the maximum and minimum grid width (r) for stretch factors $\varepsilon = 0.005$ ( ), $\varepsilon = 0.01$ ( ), $\varepsilon = 0.02$ ( ) and $\varepsilon = 0.03$ ( ) in a) small domain and b) large domain. The equivalent unitary time is normalized with the unitary time obtained from a simulation performed with a uniform mesh (t_u^{uni}).

In the meshes for cases with the larger r, like S05-32 and S30-32 (Figures 2.4b and 2.4d respectively), the region with linear stretching can be better appreciated. In fact, in these two cases the latter region is so large that the meshes do not present coarse regions. This peculiarity may appear in meshes with very large values of r or in meshes with moderate r and a small separation between the boundaries of the refined patch and the computational domain (i.e, short region with linear stretching). The more noticeable visual differences observed between these two grids are undoubtedly linked to a larger reduction of N_G. Particularly, the mesh of case S30-32 reduced N_G a factor of ~ 2.5 respect to the mesh of case S05-32. Note that this reduction of grid points is almost equivalent to the reduction obtained between the grids of all cases S##-02 and S_{uni} (see table 2.2). This observation suggests that r is the governing refinement parameter to reduce grid points, as long as the grid region with linear stretching is large enough. Nevertheless, it is important to note that for large values of r and ε the solution of the problem may change if the resolution in the coarse grid is not good enough to solve the flow appropriately. Indeed, for very large r and ε the linear solvers are not able to converge to a solution. In the present analysis these considerations have not been taken into account, but at the time writing, simulations performed in Tirant (Universidad Politécnica de Valencia) with comparable computational grids ($\varepsilon = 0.01$, $r = 6$, $Re = 1000$, $\Delta_x^r = 0.01$) are providing evidence of well resolved flows.

As mentioned above, the reduction of grid points is not the only factor that must be considered to measure the performance of the code due to the behaviour of the linear solvers. Thus, the equivalent unitary time (t_u^{eq}) obtained from the simulations run with

Code version	n_c	Partition	$t_u \times 10^4$ [s]
TUCAN	64	$1 \times 2 \times 60$	1.39
	128		1.19
	256		1.50
TUCANREF	64	$1 \times 2 \times 60$	1.38
	128		1.19
	256		1.51
TUCANREF	64	$10 \times 2 \times 6$	0.53
	128		1.19
	256		1.40

Table 2.3: Information of the set of simulations performed to analyze the improvement in performance obtained with the 3D block decomposition parallelization. n_c is the number of grid points used to dicretize a chord length ($\Delta_x^r = c/n_c$). Partition refers to the block decomposition selected in x, y and z directions (i.e., $N_P^x \times N_P^y \times N_P^z$). Note that t_u is multiplied by 10^4 and expressed in seconds.

the small and large computational domains is presented in Figure 2.5. The equivalent unitary time is compared with the unitary time of case S_{uni} (t_u^{uni}), showing that the solver with a non-uniform grid is between $5 - 10$ times faster than the solver for a simulation run with a uniform grid with the same resolution and domain size.

The influence of the grid width ratio (r) and the stretch factor (ε) for the small and large computational domains can be observed in Figures 2.5*a* and 2.5*b*, respectively. The trend observed in all the curves is similar; at $r = 2$ the maximum t_u^{eq} is found, then it decreases with increasing r until its minimum value and later it continues growing with r. The value of r that minimizes t_u^{eq} coincides for the different stretch factors studied in each domain. However, it is found for $r = 8$ in the cases with the smaller domain and for $r = 16$ in the larger domain. This indicates that in order to asses the optimum performance of the code for a specific problem, it would be convenient to carry out a preliminary performance analysis like the one presented here. Also interesting is the plateau that appears for $\varepsilon = 0.005$ and $\varepsilon = 0.01$ in the small computational domain. The reason behind it is that the maximum r achieved with $\varepsilon = 0.005$ ($\varepsilon = 0.01$) in the small domain is ~ 8 (~ 16) and therefore, the same computational grid is obtained for larger values of r. Finally, it is worthy to note that the maximum shift of t_u^{eq} between different ε values (distance between blue and green lines) is smaller than the one obtained varying r. Hence, the maximum ratio between the maximum and minimum grid width seems to enhance the overall performance of the code more than the stretch factor in this particular problem.

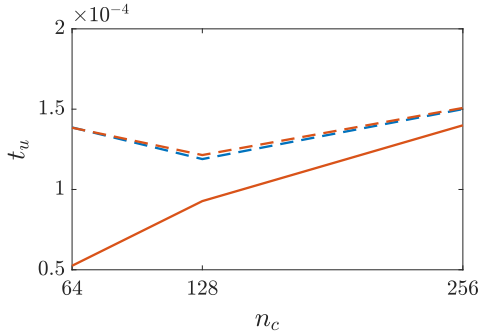

Figure 2.6: Unitary time (t_u) in seconds as a function of n_c. Simulations performed with TUCAN (TUCANREF) are colored in ( ). Simulations carried out with a block decomposition $N_P^x = 1$ $N_P^y = 2$ and $N_P^z = 60$ are represented with dashed lines ( ). The solid line ( ) depicts the simulation run with $N_P^x = 10$ $N_P^y = 2$ and $N_P^z = 6$.

The improvement in performance obtained with the change from a 2D block decomposition to a 3D block decompostion is addressed next. For this analysis, the simulation S_{uni} of Table 2.2 and two equivalent simulations with spatial resolution equal to $c/\Delta = 128$ and $c/\Delta = 64$ were carried out with TUCAN. The same three simulations were also performed with TUCANREF; first, keeping the same block decomposition used in TUCAN and later with a more coherent block decomposition for this grid size. The results obtained in this analysis and relevant information of the set of simulations carried out are detailed in Table 2.3. The unitary time (t_u) as a function of the number of points per chord (n_c) is also shown in Figure 2.6 to ease the visualization of the results depicted in Table 2.3. First, it can observed that TUCANREF (depicted in orange) behaves similar than TUCAN (colored in blue) when the same block decomposition ($N_P^x = 1$ $N_P^y = 2$ and $N_P^z = 60$) is used. The performance of both versions is almost equal and the unitary time remains roughly constant, close to $t_u = 1.4 \times 10^{-4}$. Moreover, since TUCANREF allows the division of processors in three dimensions (including the x direction), the grid points (N_G) can be split more uniformly between the different processors. For this particular grid size, this results in an improvement on the performance of the code (at least with the spatial resolutions studied). It should be noted that a priori, with an adequate partition of processors the area communicated between them is smaller and this is usually associated with better performance. Nonetheless, the parallelization depends on several factors apart from the area communicated between processors, like for instance the network connecting the computer nodes, which may drop the communication speed between cores of different nodes.

Finally, the reduction of the data storage obtained with TUCANREF is analyzed

through the cases $S\#\#$-$\#\#$ of Table 2.2. Note first that the output files which contains the statistics and the logs of the code are not considered in this analysis because their size is usually small (see section 2.1). Therefore, only the size of the larger output file (frame file) has been taken into account in the last column of $S\#\#$-$\#\#$ cases in Table 2.2. Comparing the column which shows the number of grid points (N_G) and the column where the size of the frame file is displayed, it seems that both present a similar decrease for the values of ε and r studied. As explained in section 2.1, the frame files contain several data sets, including input parameters, information of the meshes, forces calculated in the Lagrangian mesh, flow fields obtained in the Eulerian mesh, etc. These flow fields have a size N_G, which is much larger than the size of the rest of data sets saved in the frame files. Recall that by default, a simulation stores the three components of the velocity field and the pressure field with double precision, and therefore a simple estimation of the size of a frame file can be done in MB using

$$\text{size(frame file) [MB]} = \frac{4\,\text{prec[B]}\,N_G}{1024^2\text{[B]}/1\text{[MB]}}, \tag{2.7}$$

where prec is the precision used to save the data expressed in Bytes (B). The previous equation can be applied, for instance, to the simulation S_{uni}, yielding a estimated size of the frame file equal to 13062 MB, which accounts for nearly 90% of its actual size (see Table 2.2). Thus, the size of the frame file can be approximated as the number of grid points multiplied by a certain constant, which explains the similar trend observed between both columns (N_G and size) in Table 2.2. This evidence highlights the potential of TUCANREF to reduce the disk space required to save large simulations, since the total number of grid points can be reduced enormously using non-uniform grids.

2.4 Validation

In this section, the benchmarks used to validate TUCANREF are presented. The problems solved allow us to verify that the modifications implemented in TUCANREF have not altered the capabilities of TUCAN to solve incompressible flows with and without submerged rigid bodies.

Laminar Poisseuille flow

The first problem solved is a pressure-driven channel flow in laminar regime (i.e., a laminar Poiseuille flow), which has an analytical solution. The Reynolds number of the flow is $Re = hu_0/\nu$, where h is the semi-height of the channel and u_0 is the maximum velocity at its center line. Three different configurations have been carried out to test the implementation of the periodic boundary conditions in every direction. In the case LCx the pressure gradient is oriented in the x direction and the channel walls are placed

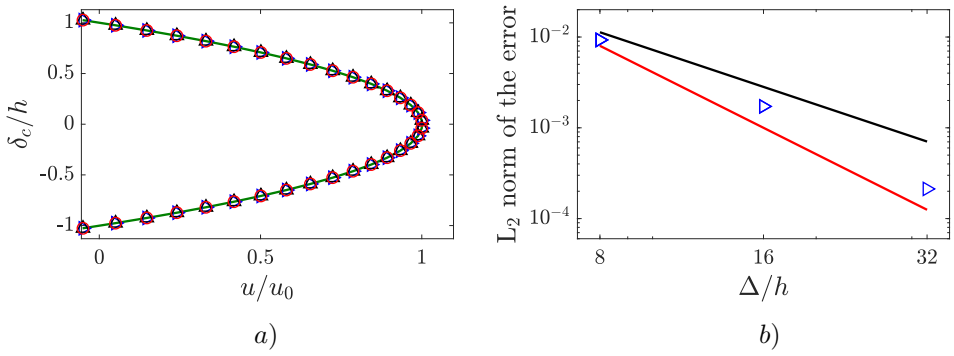

Figure 2.7: *a*) Streamwise velocity (u) along the direction perpendicular to the channel walls (δ_c) for LCx (▷), LCy (△) and LCz (○). *b*) L_2 norm of the error of u_x as a function of the spatial resolution used in the uniform grid spacings (Δ). In the left panel, the analytical solution of u is depicted with a green solid line (———). In the right panel, lines (———) and (———) have slopes of -2 and -3 respectively.

at the boundaries of the y direction, while in cases LCy and LCz the pressure gradients are oriented in y and z directions and their walls are located at the boundaries of the x and y directions, respectively. The computational domain of the channel of case LCx is $[2h \times 2h \times h]$ in the streamwise direction, direction perpendicular to the walls (δ_c), and lateral direction, respectively. In cases LCy and LCz the domain is rotated so that channel has the same size in the corresponding directions. The meshes of these three cases have uniform grid spacing along the two directions parallel to the walls of the channel with a spatial resolution $\Delta = h/16$ and variable grid spacing along δ_c. In the latter direction, the resolution is refined close to the wall ($\Delta^r \sim h/20$) and it increases towards the middle of the channel with a stretch factor $\varepsilon = 0.03$, where it reaches its maximum value ($\Delta^{\max} \sim h/13$). The time step, Δt, of these simulations has been selected so that the Courant Fredrich Levy number (CFL) is smaller than 0.1. Moreover, in order to obtain the convergence error, the case LCx has been run with two additional grids. These grids have a constant resolution along the two directions parallel to the walls of $\Delta = h/8$ and $\Delta = h/32$ and a minimum resolution near the wall of $\Delta^r \sim h/9$ and $\Delta^r = h/51$, respectively.

In Figure 2.7*a* the solution of the streamwise velocity of cases LCx (▷), LCy (△) and LCz (○) along δ_c is compared with the analytical solution, which is given by

$$u(\delta_c)/u_0 = 1 - (\delta_c/h)^2. \tag{2.8}$$

It can be observed that the four solutions coincide, reaching the maximum velocity (u_0) at the middle of the channel. Additionally, Figure 2.7*b* shows the convergence error

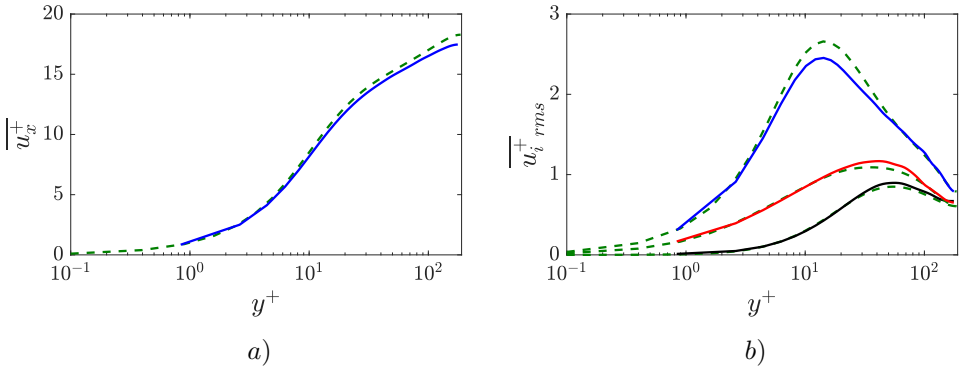

Figure 2.8: *a*) Time averaged mean and *b*) rms velocity profiles. Results of the velocities in the streamwise direction (———), vertical direction (———) and lateral direction (———), The solutions obtained by del Álamo and Jiménez [2003] are shown with green dashed lines (- - -).

of the streamwise velocity by means of the L_2 norm for the three different resolutions studied. As expected, the error of the numerical solution decreases as the resolution grows.

Turbulent flow in a plane channel

Since the previous analysis only allowed us to evaluate the linear (viscous) terms, in this second problem, all the terms (including also the pressure and the non-linear terms) are evaluated with a pressure-driven channel in turbulent regime (turbulent channel). This problem has been broadly studied in the literature and there are reliable statistics data of this flow on the internet to be used for comparison. The turbulent channel solved here is the one studied by Kim et al. [1987]. The pressure gradient in the streamwise direction is chosen so that the Reynolds number based on the friction velocity, u_τ, is $Re_\tau = h/\nu = 180$. The size of the simulated channel is $4\pi h$ and $4\pi h/3$ in the streamwise and lateral directions, respectively. Similarly than in the laminar Poiseuille flow studied before, the computational mesh chosen has a uniform grid spacing along the two directions parallel to the walls of the channel and a non-uniform grid spacing (with $\varepsilon = 0.03$) along its height. The cells with minimum resolution are located close to the walls is $\Delta^r \sim h/101$ and the maximum resolution found at the middle of the channel is $\Delta^{\max} \sim h/10$. In this simulation the time step selected keeps the CFL $\lesssim 0.3$.

In Figure 2.8 the time-averaged and the root-mean-squared (rms) velocity profiles obtained with TUCANREF are compared with the data of del Álamo and Jiménez [2003], which has been chosen as reference case. The mean streamwise velocity and the

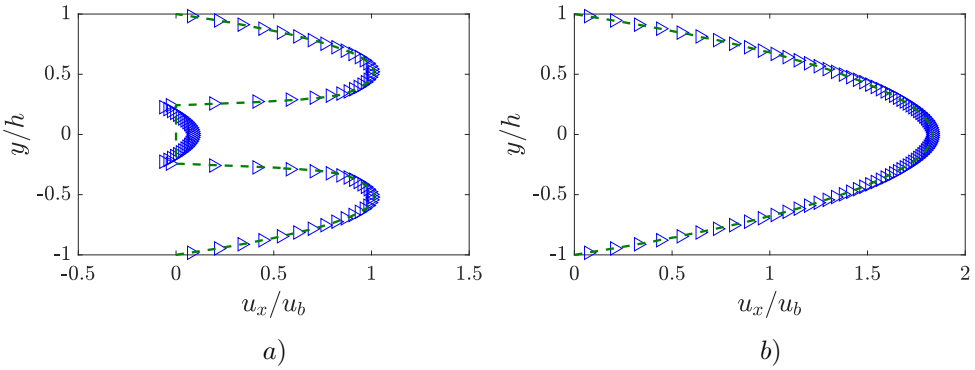

Figure 2.9: Streamwise velocity profiles at *a*) $z = 0$ and *b*) $z \mid h$. Results obtained with TUCANREF (▷) and with NEK5000 (---).

rms profiles in the vertical and lateral directions are similar to those obtained in the reference case. In the streamwise rms velocity, slightly larger differences are observed in the maximum value, where TUCANREF predicts a smaller peak. Note also that the resolution close to wall of our simulation ($\Delta y^+ \sim 0.8$) is considerably larger than the resolution selected in del Álamo and Jiménez [2003]. The source of the small differences shown in the velocity profiles can be due to an insufficient period of time averaging or a problem related with the larger resolution employed. Moreover, the mesh used in the reference case is twice as long as the one used in our simulations and also they used spectral methods instead of finite differences for the spatial discretization. Thus, the results obtained are considered similar enough to validate the problem.

Flow around a fixed sphere

In the third case of the validation, the immersed boundaries are tested solving the flow around a sphere placed inside a cubical channel of semi-height h [Uhlmann, 2006]. The flow is driven by a pressure gradient selected so that the $Re_b = u_b h/\nu \sim 275$, where u_b is the bulk velocity. The sphere is located at the middle of the channel and has a diameter $D/h = 0.4844$. The boundary conditions in the streamwise (x) and lateral (z) directions are periodic and in the vertical direction (y) a no-slip boundary condition is imposed. The results of TUCANREF are compared with a solution obtained using the spectral elements code NEK5000 [Fischer et al., 2008]. In our simulation, the channel has been discretized in space as the previous two cases (with a non-uniform mesh), keeping a region around the sphere with a constant resolution of $\Delta = h/64$. Regarding the Δt, it has been chosen so that CFL $\lesssim 0.5$. In Figure 2.9 the streamwise velocity profiles obtained with NEK5000 and with TUCANREF are shown along the

Code	u_b	Re_b	$\overline{c_d}$	diff [%]
NEK5000	0.8894	275.4	0.6726	-
TUCAN3REF	0.9946	275.0	0.7013	4.2625

Table 2.4: Parameters and drag results of both simulations. u_b is the bulk velocity, Re_b is the Reynolds number based on the bulk velocity, $\overline{c_d}$ is the mean drag coefficient and diff indicated the difference of $\overline{c_d}$ in % between both simulations.

vertical direction at two sections located at $x/h = 0$, $z/h = 0$ and $x/h = 0$, $z/h \sim 1$, respectively. Figure 2.9*a* shows that in the first section the flow encounters the sphere at $-D/2h \leq y/h \leq D/2h$, thus the streamwise velocity is zero at those positions. When the flow is studied away from the sphere (Figure 2.9*b*), a similar parabola to that observed in the laminar Poiseuille flow appears. The streamwise velocities distribution obtained with both codes are similar at the two sections analyzed. The difference observed in the section where the flow pass through the sphere (Figure 2.9*a*) is due to the immersed boundary method, but note that it does not affect the solution in the rest of the domain.

Additionally, the drag produced by the sphere is compared in Table 2.4, showing differences smaller than 5%. Given the fact that the simulations have been performed with different solvers, which use completely different methodologies, the results observed are considered acceptable in terms of the validation.

Flow around a moving sphere

After validating the immersed boundary conditions for a fixed sphere and the resulting forces on it, the last benchmark studied a sphere which is moving inside of a periodic channel. This benchmark is meant to test that TUCANREF is still able to move bodies across periodic domains. To that end, a sphere with a diameter $D/h = 0.4844$ is placed at the middle of a cubical channel with semi-height h, as in the previous benchmark. However, in this problem, no pressure gradient is imposed, instead the sphere starts moving towards the right-upper-north corner (see Figure 2.1*b*) with a constant velocity u_{sph}. The computational grid of the channel in this simulations is uniform in all directions, since the sphere is moving across the whole domain. Remind that, in order to solve the body-fluid interaction, TUCANREF requires that the body is placed inside a region with uniform grid spacing. The spatial resolution used in this problem is $\Delta = 64/h$ and the time step has been selected to keep CFL < 0.25.

In Figure 2.10 the time evolution of the streamwise force (——) and the streamwise position of the center of the sphere (- - -) are shown. Although not shown, the vertical and lateral forces are similar since the motion of the sphere is equal in the three directions. Note that at $tu_{sph}/h = 0$ in Figure 2.10, the sphere already intersects

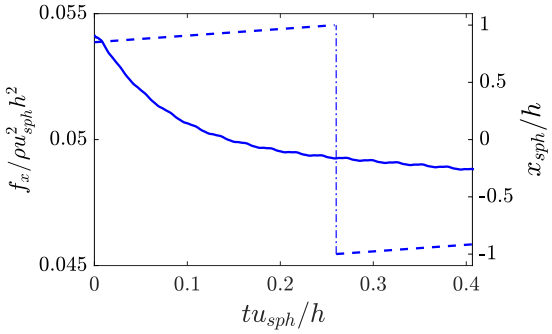

Figure 2.10: Time evolution of the streamwise force, f_x, (———) and the streamwise position of the center of the sphere, x_{sph}, (- - -).

with the corner. As the sphere goes through the corner, the streamwise force decreases smoothly and does not present any discontinuity. This indicates that the capability of TUCANREF to move bodies through periodic boundary conditions is intact.

CHAPTER

THREE

Problem statement

As discussed in chapter 1, the main difficulty when developing models that predict the aerodynamic forces is the broad parametric space that appears for the different kinematics and geometric parameters. From the point of view of the kinematics, in this thesis we want to analyze the transition from a heaving motion to a flapping motion in forward flight. This transition is achieved by rotating a wing with respect to an axis of rotation parallel to the free stream velocity and separated a distance from the root of the wing. From the point of view of the geometry, the effect of the aspect ratio of rectangular wings will be analyzed. Note that even with this relatively simple kinematics and geometry, there are several parameters that need to be defined, i.e. speed of the motion of the wing, shape of the wing sections, flow properties, etc.

In this chapter all these parameters are defined and specified, resulting in a database of direct numerical simulations. The details of the computational setup of these simulations are presented in the last section of this chapter. The results of these simulations will be analyzed in chapters 4, 5 and 6.

3.1 Problem description

The configuration considered in the present study consists of a pair of rectangular wings made of NACA 0012 airfoils, with two aspect ratios, $AR = b/c$, equal to 2 and 4 (where c and b are the maximum chord and span of the wing, respectively). The wing cross-section is a NACA 0012 airfoil, which is a standard choice in the literature [Isogai et al., 1999, Young and Lai, 2004]. The wings have no geometric twist, and rounded edges at the wing tips, as shown in Figure 3.1.

This pair of wings is placed side by side, as shown in Figure 3.1*a*, separated a distance $c/2$ (measured between the inboard wing tips). The wings perform a flapping motion (depicted in Figure 3.1*b*) as they fly forward at a constant velocity u_∞. The flapping motion consists in a rotation of each wing around an axis parallel to the forward flight direction (red line in Figure 3.1*b*), which is located at a distance R from the inboard wing tip. The flapping angle, measured from the horizontal plane, follows a sinusoidal

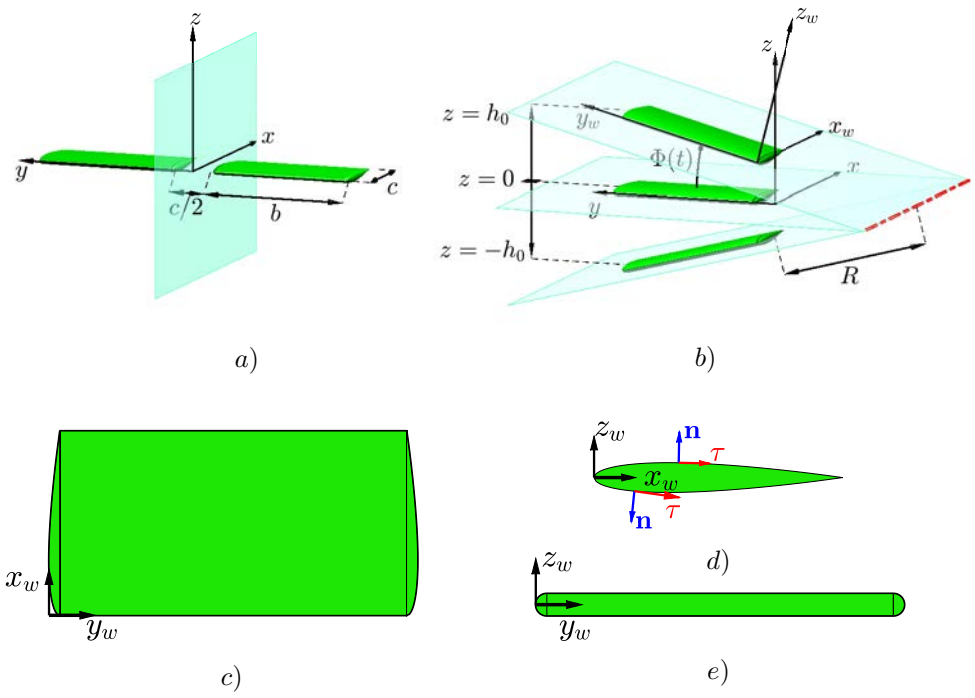

Figure 3.1: *a*) Sketch of the two wings configuration and *b*) sketch of the kinematics of the left wing. The wing chord, span of the wing and the radius of flapping motion, which is the distance between the inboard wing tip and the axis of rotation are denoted by c, b and R, respectively. *c*) Top view of the wing. *d*) Side view of the wing. *e*) Front view of the wing.

Case	AR	R/c	Ro	Φ_0	h_0/c	N_G (M)
AR2-R000	2	0	1.82	30.00°	1	89
AR2-R005	2	0.5	2.36	23.58°	1	89
AR2-R020	2	2	3.92	14.48°	1	89
AR2-R080	2	8	9.97	5.74°	1	89
AR2-inf	2	∞	∞	-	1	89
1W-AR2-inf	2	∞	∞	-	1	67
AR2-inf*	2	∞	∞	-	0.52	89
AR4-R000	4	0	3.92	14.48°	1	122
AR4-R000*	4	0	0.91	30.00°	2	153
AR4-R020	4	2	5.94	9.59°	1	122
AR4-R020	4	2	2.61	14.48°	1.5	136
AR4-R020*	4	∞	∞	-	1	122

Table 3.1: Parameters used to define the motion and the geometry of the wings in the simulations carried out for this study. AR is the aspect ratio of the wing, R is the radius of flapping motion, Ro is the Rossby number (see equation 3.3), Φ_0 is the amplitude of the flapping angle (in degrees), h_0 is the amplitude of the vertical displacement of the outboard wing tip and N_G is the total number of grid points of the computational domain.

law,

$$\Phi(t) = \Phi_0 \cos(\omega t), \tag{3.1}$$

where ω is the angular frequency and Φ_0 is the amplitude of the flapping motion which is defined as

$$\Phi_0 = \arcsin\left(\frac{h_0/c}{R/c + AR}\right) \tag{3.2}$$

As it can be observed in Table 3.1, most simulations have the same vertical displacement of the outboard wing tip, $h_0 = c$. As discussed below, there are three cases with $h_0 \neq c$: one with $AR = 2$ and two with $AR = 4$. Note that, for all the simulations with $h_0 = c$, the amplitude of the flapping motion varies with the radius of flapping motion, R, and the aspect ratio of the wing, AR. Also, for the cases with $h_0 = c$, equation (3.2) implies that the vertical velocity of the outboard wing tip is approximately the same for any value of R and AR (provided that the angular frequency remains the same). The parameters that define the motion of the wings and their geometry are shown in Table 3.1 for all the simulations.

Figure 3.1 also shows the two reference frames that will be used in the analysis of the results. First, an inertial reference frame x, y, z that moves with the wings at constant

velocity u_∞. In this reference frame, the forward motion results in an incoming free stream along the x (streamwise) direction. The vertical direction is z, and y is the direction along the span of the wing when $\Phi(t) = 0$. Figure 3.1*b* shows a non-inertial reference frame, x_w, y_w, z_w, which moves with the wing so that x_w is the chordwise direction, y_w is the spanwise direction along the wing, and z_w is a direction perpendicular to the mean surface of the wing. The leading edge of the wing is at $x_w = 0$, and it moves due to the flapping motion in the $x = 0$ plane. The inboard wing tip of the wing is at $y_w = 0$, while the outboard wing tip is at $y_w/c = AR$.

As shown in Table 3.1, several values of R are considered in the present study, varying from $R = 0$ (flapping with respect to the inboard wing tip) to $R \to \infty$ (heaving motion). For all cases, the reduced frequency is $k = \omega c/u_\infty = 1$ and the Reynolds number is $Re = u_\infty c/\nu = 500$. Note that, for completeness, the problem of a single wing of $AR = 2$ in heaving motion has also been considered. This last case is labeled 1W-AR2-Rinf in Table 3.1, while the cases with two wings are labeled AR#-R### (with the first digit corresponding to the numerical value of the AR and the last three digits to the numerical value of R/c).

Additionally, three cases with different vertical displacement of the outboard wing tip, h_0, have also been performed. The first one, is a heaving case with $AR = 2$ and $h_0 = 0.52$ (AR2-Rinf*). The other two cases are flapping cases with $AR = 4$ and $R = 0$ (AR4-R000*) and 2 (AR4-R020*). These two last simulations have been designed so that the motion from their inboard wing tip to their mid-span ($0 \leq y_w \leq 2$) is equal to the motion of the wings of cases with the same R and $AR = 2$ (i.e., AR2-R000 and AR2-R020, respectively). This is done by imposing the same amplitude of the flapping motion, Φ_0 of the $AR = 2$ cases. Thus, since they have an $AR = 4$, the vertical displacement of the outboard wing tip of each case is $h_0 = 2$ and 1.5 for case AR4-R000* and AR4-R020*, respectively (see equation 3.2). Note, that these three cases are labeled in Table 3.1 as the rest of the cases with two wings but with an * at the end of their name.

As discussed in the introduction, the Rossby number is the ratio between the advective terms in the Navier-Stokes equations and the Coriolis acceleration. For flapping wings in forward flight it is defined as

$$Ro = \frac{{u_\infty}^2/c}{(\omega\Phi_0)^2\,(R+b)} = \frac{1}{(k\Phi_0)^2}\frac{c}{R+b}. \tag{3.3}$$

For cases with $h_0 = c$, the amplitude of the flapping motion can be approximated to $\Phi_0 \approx c/(R+b)$, considering $R/c \gg 1$ (see equation 3.2). This yields

$$Ro \approx \frac{1}{k^2}\left(AR + \frac{R}{c}\right). \tag{3.4}$$

Since in the present study the reduced frequency is kept constant, $k = 1$, Ro of these cases varies only as a consequence of variations in the geometric parameters, as shown

in Lee et al. [2016]. Moreover, for cases with the same AR, any increment in R/c is translated (almost) linearly into an increment in the Rossby number. Note also that, in the cases with $h_0 = c$ the choice of $k = 1$ results in u_∞ being of the same order of magnitude as the vertical velocity of the outboard wingtip, $\Phi_0\omega(R + b)$. Hence, the Coriolis acceleration is of the same order of magnitude for all those cases.

Finally, in order to keep the configuration as simple as possible, pitching motion of the wing has not been considered.

3.2 Grid convergence study

In this section we present the grid refinement study carried out to select the resolution used in the simulations. This study is performed in 2D for its lower computational cost. Note that the resolution requirements of the 2D simulations are expected to be similar to those of the 3D configurations, since the geometry of the wing is somewhat smoother in the spanwise direction than in the streamwise and vertical directions (see Figures 3.1*c*, 3.1*d* and 3.1*e*).

We perform 2D simulations of a heaving NACA0012 airfoil, with heaving amplitude $h_0 = c$, Reynolds number $Re = 500$ and reduced frequency $k = 1$, varying the resolution from $n_c = 32$ to $n_c = 192$. Remind that n_c denotes the spatial resolution in number of grid points per chord length. The time step Δt is varied accordingly, keeping the same CFL for all the cases (lower than 0.3). The convergence is evaluated in terms of the aerodynamic force, using as reference the results of the case with the highest resolution ($n_c = 192$). The time evolution of the total force coefficient,

$$c_{tot} = \frac{|\boldsymbol{F}|}{\frac{1}{2}\rho {u_\infty}^2 c}, \tag{3.5}$$

of four of the simulations is reported in Figure 3.2*a*. In the previous expression $\boldsymbol{F}$ is the total aerodynamic force on the airfoil. While some deviations are observed for the resolution $n_c = 32$ with respect to the reference case, the results of the simulation with resolution $n_c = 56$ are very close to those of the reference case. In order to quantify these differences, Figure 3.2 shows the errors in the mean and root-mean-squared (rms) of the force

$$\overline{\epsilon_{tot}}(n_c) = \frac{\left|\overline{c_{tot}}_{,n_c} - \overline{c_{tot}}_{,192}\right|}{c^{rms}_{tot,192}} \tag{3.6}$$

$$\epsilon^{rms}_{tot}(n_c) = \frac{\left|c^{rms}_{tot,n_c} - c^{rms}_{tot,192}\right|}{c^{rms}_{tot,192}} \tag{3.7}$$

where the superindex rms denotes the root-mean-square of the fluctuation. Figure 3.2*b* shows the errors as a function of the resolution. As expected, the errors decrease with increasing resolution. Taking into account a compromise between the computational

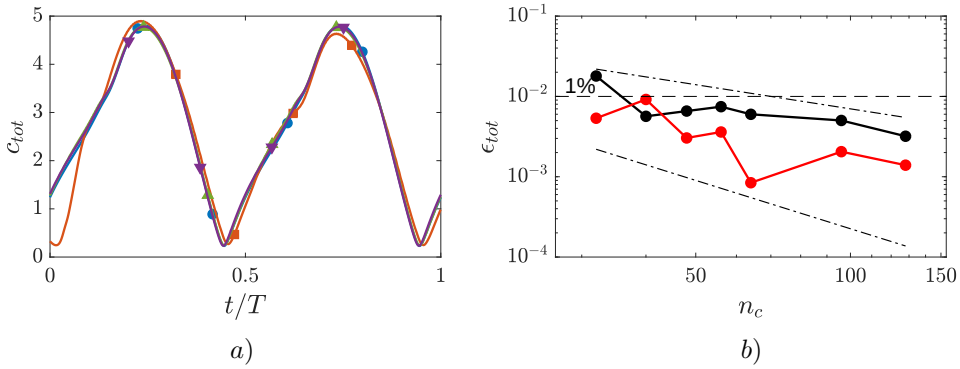

Figure 3.2: *a*) Total force coefficient c_{tot} during one cycle for 2D cases performed with resolutions $c/\Delta = 32$ ( ), $c/\Delta = 56$ ( ), $c/\Delta = 96$ ( ) and $c/\Delta = 192$ ( ). *b*) Errors of c_{tot} (ϵ_{tot}) obtained in mean ( ) and rms ( ). The black dash-dotted lines have logarithmic slopes -1 and -2.

cost and the accuracy of the results, a resolution of $n_c = 56$ is selected for all the simulations presented. With this resolution the errors for both mean and rms of the forces are smaller than 1%.

3.3 Numerical method

The problem described in the previous section is solved using DNS with the in-house code TUCAN, which solves the Navier-Stokes equations for an incompressible flow and has been described in detail in chapter 2. The presence of bodies of arbitrary shape (wings in this case) is modelled with the direct forcing IBM proposed by Uhlmann [2005]. The fluid domain is discretized with a uniform, staggered Cartesian grid and centered, second-order finite differences are used to approximate the spatial derivatives. The time is discretized with a fractional-step method, in which the time advancement is performed with a low-storage Runge-Kutta scheme of three stages.

In the present study, all the simulations with two wings are performed in a computational domain with the same clearance (i.e., minimum distance between the wing and the domain boundaries) in the streamwise, spanwise and vertical directions. As a consequence, the streamwise range of the computational domain is always $x/c = [-3, 9]$, leaving $3c$ upstream of the leading edge of the wing. The spanwise range is equal to $y/c = [0, 0.25 + AR + 3]$, leaving a clearance of $3c$ with the lateral boundary of the computational domain. The vertical range is $z/c = \pm(h_0/c + 3)$, leaving a clearance of $3c$ with the vertical boundaries of the computational domain.

As shown in Figure 3.1*a*, $y = 0$ is the symmetry plane between both wings (indicated with a shaded plane), hence only the wing in the $y > 0$ domain is contained in the computational domain. The effect of the wing in the $y < 0$ domain is simulated by imposing a symmetry condition at the plane $y = 0$. Hence, the boundary conditions in the computational domain are uniform free stream at the plane $x = -3c$, outflow (advective) boundary condition at $x = 9c$, and free slip at the vertical and spanwise boundaries.

Note that, even for completely symmetrical configurations, lateral instabilities might develop in the flow if the Reynolds number is sufficiently large, leading to non-symmetric aerodynamic forces on the wing [Sears, 1956]. As a consequence, the assumption of a symmetry condition at the center plane of the configuration is commonly used in the literature only for low to moderate Reynolds numbers [Trizila et al., 2011, Kang et al., 2012, Visbal et al., 2013]. For instance, Visbal et al. [2013] simulated the flow around a heaving wing at $Re = 10000$ using an implicit LES and a symmetry condition at the mid-span of the wing. In the present case, the lower Reynolds number of the flow makes the assumption of symmetry with respect to $y = 0$ even more reasonable.

For the case with only one wing (1W-AR2-Rinf), the computational domain is $x/c = [-3, 9]$, $y/c = [-2, 2]$ and $z/c = [-4, 4]$ and $y = 0$ corresponds to the mid-span section of the wing. The boundary conditions are the same as in the cases of two wings. Note that, even if this case is solved without the symmetry assumption, the resulting flow is completely symmetric with respect to the mid-span of the wing (not shown). This result confirms the validity of the assumption of symmetry with respect to the plane $y = 0$ for the cases of two wings.

The resolution employed in all computations is 56 grid points per chord length in all spatial directions ($\Delta = \Delta x = \Delta y = \Delta z = c/56$). This resolution, which is comparable to that used in previous studies at similar Re [Taira and Colonius, 2009], was chosen after the grid convergence study shown in the previous section. The total number of grid points of the computational domain for all cases is indicated in Table 3.1. In addition to the grid for the fluid domain, a Lagrangian grid for the wing needs to be defined. In the IBM of Uhlmann [2005], the area associated to each Lagrangian point has to be roughly the same as the square of the grid spacing for the fluid domain. This leads to a total number of 17,050 Lagrangian points evenly distributed on the surface of the wing of $AR = 2$ (36,538 for the wings of $AR = 4$).

All cases in Table 3.1 are simulated with the same initial condition, $u = u_\infty$ and $v = w = 0$ (i.e., unperturbed free-stream velocity). The simulations are run until the velocity field and the forces on the wing reach a periodic state, with period $T = 2\pi/\omega = 2\pi c/ku_\infty$, imposed by the motion of the wing. This periodic state is reached after a transient of approximately $10T$, for all cases except for AR4-R000*. The first four cycles are run with a lower resolution. Then, the velocity field is interpolated onto the fine

grid, and run for another 6 cycles. Note that the aerodynamic forces converge after 2-3 cycles while the flow downstream of the airfoil needs a longer time integration interval to converge. After that transient, the variation in the aerodynamic forces or flow velocities between consecutive cycles are negligible (relative differences smaller than 10^{-5}). For case AR4-R000*, the non-periodicity of the forces is related with the development of 3D instabilities in the flow, as discussed in chapter 6. However, the forces vary from consecutive periods less than 2.5%. Note also that the fact that the flow develops 3D instabilities suggests that the hypothesis of a symmetry plane between the wings is probably not appropriate for this case.

It is important to take into account that one of the advantages of the algorithm implemented in TUCAN is that it provides directly the distribution of aerodynamic forces per unit area on the surface of the wing, $\mathbf{f}$. This feature was exploited by Chan-Braun et al. [2011] to analyze the hydrodynamic force distribution on the surface of spherical particles in a low-Reynolds number turbulent flow and by Arranz et al. [2018b] to analyze the force distribution on the wing of a winged-seed in autorotation. In the present study, the force per unit area is decomposed during post-processing as the sum of two vectors, namely, a vector normal to the surface and a vector tangent to the surface,

$$\mathbf{f}_{n*} = (\mathbf{f}\cdot\mathbf{n})\,\mathbf{n} \qquad \text{and} \qquad \mathbf{f}_{\tau} = \mathbf{f} - \mathbf{f}_{n*}. \tag{3.8}$$

Note that $\mathbf{n}$ is the local unit vector normal to the surface, pointing towards the fluid, as shown in Figure 3.1*d*. Note that from a physical point of view, $\mathbf{f}_{n*}$ corresponds to the forces due to the pressure and the normal viscous stresses, while $\mathbf{f}_{\tau}$ corresponds to the skin friction (i.e. the tangential shear stresses acting on the surface of the wing). Finally, for convenience we also define

$$\mathbf{f}_{n} = \mathbf{f}_{n*} - \left(\frac{1}{S}\int_S (\mathbf{f}\cdot\mathbf{n})\,\mathrm{d}S\right)\mathbf{n}, \tag{3.9}$$

where S stands for the wetted surface of the wing. Note that equation (3.9) is roughly equivalent to removing the ambient pressure from $\mathbf{f}_{n*}$. In any case, the differences between $\mathbf{f}_n$ and $\mathbf{f}_{n*}$ are small, less than 10%. Note also that the total force resulting from integrating $\mathbf{f}_n$ and $\mathbf{f}_{n*}$ over the (closed) surface of the wing is exactly the same.

Finally, the IBM used to simulate the presence of the moving wing has limitations to describe the force distribution near the trailing edge of the wing. Such limitations have been recently addressed by Maertens and Weymouth [2015], though not implemented in this study. The problem arises due to the discrete representation of the Dirac's delta employed to transfer the forces from the wing's grid to the mesh where the fluid is solved (regularized delta functions, see [Peskin, 2002]). In the present calculations, we use a 4-point regularized delta function, which introduces a spurious interaction between the

upper and lower surfaces of the wing when the distance between them is smaller than 2Δ. For the present geometry and resolution, this corresponds to $x_w \gtrsim 0.85c$. In this region (indicated with a dashed black line in the force distributions shown in chapter 4, Figures 4.4 and 4.8) the distributions of $\mathbf{f}, \mathbf{f}_\tau$ and $\mathbf{f}_n$ are not reliable. However, the spurious interactions between the upper and lower surface cancel each other, so that the total force (integrated over the whole wing) is not affected by this phenomenon [Moriche et al., 2016, Moriche, 2017, Moriche et al., 2017].

CHAPTER
FOUR

Force analysis in wings of $AR = 2$[1]

In this chapter, the transition from flapping to heaving is studied for the database cases with wings of $AR = 2$. In this transition, the spanwise-averaged effective angle of attack of the wing increases, $\langle \alpha_e \rangle$, while the effect of the Coriolis acceleration becomes weaker (i.e., the Rossby number decreases). The cases analyzed in this chapter and some of their parameters have been extracted from Table 3.1 and are presented along with some relevant dynamic information in Table 4.1. The study focuses on the characterization of the aerodynamic forces, both in terms of the overall forces on the wing and their surface distribution. These forces are correlated with specific flow features that appear close to the wing by means of 2D and 3D flow visualizations. Finally, the results of the DNS are used to evaluate the performance of an unsteady panel method, and to explain its deficiencies.

4.1 Aerodynamic forces

Figure 4.1 shows the time evolution of the net force coefficients,

$$C_x = \frac{1}{\frac{1}{2}\rho {u_\infty}^2 bc} \int_S \mathbf{f} \cdot \mathbf{e}_x \mathrm{d}S, \qquad C_z = \frac{1}{\frac{1}{2}\rho {u_\infty}^2 bc} \int_S \mathbf{f} \cdot \mathbf{e}_z \mathrm{d}S, \tag{4.1}$$

where ρ is the density of the fluid, $\mathbf{e}_x$ and $\mathbf{e}_z$ are the unit vectors in the streamwise (x) and vertical (z) directions, respectively. The corresponding time-averaged force coefficients during the downstroke (i.e., half cycle) are reported in Table 4.1 ($\overline{C_x}$ and $\overline{C_z}$). The pitching moment coefficient is defined as

$$C_{My} = \frac{1}{\frac{1}{2}\rho {u_\infty}^2 bc^2} \int_S (\mathbf{x}_P \times \mathbf{f}) \cdot \mathbf{e}_{y_w} \mathrm{d}S, \tag{4.2}$$

where $\mathbf{x}_P$ is the position vector from the origin of the non-inertial reference frame (x_w, y_w, z_w) to any point of the wing surface and $\mathbf{e}_{y_w}$ is the unit vector along the wing span. For completeness, we also include in Table 4.1 the values of $\overline{C_{My}}$, the pitching moment coefficient averaged over half cycle.

[1] The contents of this chapter have been accepted for publication in the *Journal of Fluids and Structures*.

Cases	R/c	Ro	Φ_0	h_0/c	$\langle\alpha_e\rangle_{\max}$	$\overline{C_x}$	$\overline{C_z}$	$\overline{C_{My}}$
AR2-R000	0.0	1.82	30.00°	1.00	27.64°	0.143	0.859	-0.258
AR2-R005	0.5	2.36	23.58°	1.00	31.69°	0.132	1.052	-0.319
AR2-R020	2.0	3.92	14.48°	1.00	37.16°	0.115	1.356	-0.420
AR2-R080	8.0	9.97	5.74°	1.00	42.03°	0.094	1.670	-0.531
AR2-Rinf	∞	∞	-	1.00	45.00°	0.080	1.888	-0.615
1W-AR2-Rinf	∞	∞	-	1.00	45.00°	0.081	1.808	-0.579
AR2-Rinf*	∞	∞	-	0.52	27.64°	0.142	0.877	-0.251

Table 4.1: Parameters and main results of DNS cases simulated. R is the radius of flapping motion, Ro is the Rossby number (see equation 3.3), Φ_0 is the amplitude of the flapping angle (in degrees), h_0 is the amplitude of the vertical displacement of the outboard wing tip and $\langle\alpha_e\rangle_{\max}$ is the maximum absolute value of the effective angle of attack averaged along the wing span (in degrees), which occurs at mid-stroke. The coefficients $\overline{C_x}$, $\overline{C_z}$ and $\overline{C_{My}}$ are the streamwise force coefficient, the vertical force coefficient and the pitching moment coefficient with respect to the leading edge of the wing, respectively. All three coefficients are time-averaged during the downstroke of the wing.

Due to the vertical symmetry of the motion, the vertical force (Figure 4.1a) generated during the downstroke is equal in magnitude to the vertical force generated during the upstroke, but with opposite sign. With increasing radius of flapping motion, the peak of C_z increases, so that the maximum force is obtained for the heaving wing case, AR2-Rinf. Interestingly, case 1W-AR2-Rinf has peak values of C_z slightly lower than case AR2-Rinf. Note also, that the peak is reached slightly before the mid-downstroke for all cases shown in Figure 4.1a, at a time that does not seem to depend on R.

While for the present configuration the peak of C_z increases with R, a different trend has been reported for revolving wings [Dickson and Dickinson, 2004, Lentink and Dickinson, 2009, Jardin and David, 2014, Lee et al., 2016]. These studies found that the maximum of C_z is greater for wings rotating with smaller R, and this result was attributed to a stabilization of the LEV produced by the Coriolis force. The reason behind this discrepancy might be found in a fundamental difference concerning the effective angle of attack of the wing, α_e, in revolving wings with respect to the present configuration. In revolving wings, the effective angle of attack is just the geometrical angle of attack of the wing, constant for all spanwise positions and independent of R. For flapping wings in forward flight, the effective angle of attack is given by the ratio of the vertical velocity at each spanwise section, $w_w(y_w, t)$, and the forward flight velocity, resulting in

$$\alpha_e(y_w, t) = \arctan\left(\frac{w_w(y_w, t)}{u_\infty}\right) = \arctan\left(\frac{(R + y_w)\mathrm{d}\Phi/\mathrm{d}t}{u_\infty}\right), \tag{4.3}$$

It is also useful to define the effective angle of attack averaged over the wing span

$$\langle \alpha_e \rangle(t) = \frac{1}{b} \int_0^b \alpha_e(y_w, t) \mathrm{d}y_w. \tag{4.4}$$

Hence, for a constant value of h_0 the flapping wing moves faster as R increases, resulting in larger $\langle \alpha_e \rangle$ (see Table 4.1), and larger C_z during the downstroke. Recall that, by design (see equation 3.2), the vertical velocity of the outboard wing tip is approximately the same for the cases with $h_0 = c$, and therefore α_e is roughly independent of R at the outboard wing tip. When $R \to \infty$, both $w_w(y_w, t)$ and $\alpha_e(y_w, t)$ become uniform over the wing, maximizing the aerodynamic force. Hence, we hypothesize that the larger α_e along the wing span is responsible for the increase of C_z with R.

In order to confirm this hypothesis, we have performed an additional simulation in heaving motion, case AR2-Rinf*. The heaving amplitude, $h_0/c = 0.52$, has been selected so that the effective angle of attack of the wing is the same as the spanwise-averaged effective angle of attack of the case with $R = 0$ (case AR2-R000), see Table 4.1. The profiles of C_z as a function of time for both cases (2W-R000 and 2W-Rinf*) are shown in Figure 4.1*a*. They are found to be very similar, with a small variation of the peak values and the time when they are reached. Thus, it is confirmed that for the present configuration the variation of the aerodynamic forces with R is mainly governed by the resulting variation of the effective angle of attack, with little influence of Ro (i.e., inertial terms seem to be dominant over the apparent acceleration terms). Note that the value of $\overline{C_z}$ reported in Table 4.1 for AR2-R000 is marginally smaller (about 2%) than for AR2-Rinf*. Although this difference might be too small to be significant in the present case, it is qualitatively consistent with the results of Guerrero Guerrero [2010], who reported larger aerodynamic forces for heaving wings than for flapping wings, at a somewhat lower Re and higher k than the present cases.

In terms of the forces in the streamwise direction (Figure 4.1*b*), the evolution of C_x is the same during the upstroke and during the downstroke, owing to the symmetry of the motion. For all cases, the values of C_x during the downstroke/upstroke are essentially positive, indicating that net drag is being produced. This result indicates that the wing kinematics employed in this study should not have practical utility to sustain forward flight. However, as mentioned above, the kinematics do illustrate the effect of R in a configuration as simple as possible.

Figure 4.1*b* also shows that the maximum value of C_x is reached during the transitions between upstroke and downstroke, around $t/T = 0$ and 0.5. The dependence of the positive peak values of C_x with R is weak for the cases with the same h_0, and the magnitude ($C_{x,\max} \approx 0.2$) is similar to the drag coefficient of a rectangular flat plate of $AR = 2$ at zero angle of attack and a comparable Reynolds number, $Re = 300$ Taira and Colonius [2009]. However, the time to $C_{x,\max}$ varies significantly with R for these cases, although it remains close to $t/T = 0$ and 0.5 for all cases. On the other hand,

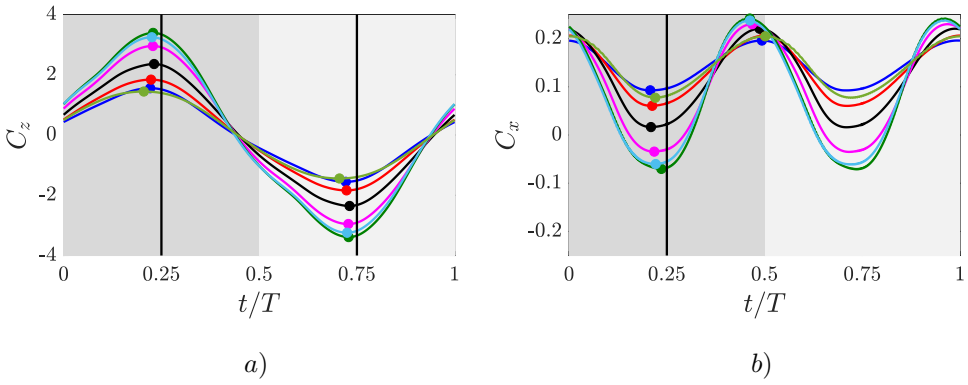

Figure 4.1: Forces coefficients *a*) C_z and *b*) C_x during one cycle of DNS cases AR2-R000 ( ), AR2-R005 ( ), AR2-R020 ( ), AR2-R080 ( ), AR2-Rinf ( ), 1W-AR2-Rinf ( ) AR2-Rinf* ( ). Maximum and minimum values of the forces coefficients are depicted with (●). Dark and light greys regions represent downstroke and upstroke motions respectively.

the minimum value of C_x (i.e., when the wing is closer to produce thrust) is obtained at the mid-downstroke and mid-upstroke, $t/T = 0.25$ and 0.75, when the effective angle of attack is maximum over the wing. The effect of R in the magnitude of $C_{x,\min}$ is apparent for the cases with the same h_0. Indeed, cases AR2-R080 and AR2-Rinf show negative values of C_x at mid-upstroke and mid-downstroke, indicating thrust production.

Finally, note that, for the cases with the same $\langle\alpha_e\rangle$, AR2-R000 and AR2-Rinf*, the differences between the peaks of C_x are similar to those found in C_z, even if the time-averaged streamwise force during the downstroke motion ($\overline{C_x}$) of both cases is roughly the same (see Table 4.1). At the mid-downstroke ($t/T = 0.25$), the minimum of C_x is larger for AR2-Rinf* than for AR2-R000, indicating less drag production. Interestingly, for these two cases that isolate the effect of R from the effect of the effective angle of attack, the trend of $C_{x,\min}$ with R is the same as that found for the cases with $h_0 = c$. This suggests that the effect of both R and α_e is to produce more negative streamwise forces, i.e. less drag or more thrust.

In order to evaluate the origin of the changes in C_z and C_x at mid-stroke (more lift and more thrust as R and $\langle\alpha_e\rangle$ increase), the contributions from the normal and tangential forces to C_x and C_z are analyzed next. These contributions are defined as

$$C_i^n = \frac{\int_S \mathbf{f}_n \cdot \mathbf{e}_i \mathrm{d}S}{\frac{1}{2}\rho {u_\infty}^2 bc}, \qquad C_i^\tau = \frac{\int_S \mathbf{f}_\tau \cdot \mathbf{e}_i \mathrm{d}S}{\frac{1}{2}\rho {u_\infty}^2 bc}, \tag{4.5}$$

where the subindex i stands for x or z. Recall that, from a physical point of view, C_i^n is related to the pressure forces mainly, while C_i^τ is the contribution from the viscous

skin friction.

Although not shown, C_z is dominated by the contribution from the normal force (i.e., pressure forces), while the contribution from tangential forces is smaller than 13% in all cases. In other words, pressure is dominant in the generation of lift. On the other hand, the contribution of normal and tangential forces to C_x is more balanced. This can be observed in Figure 4.2 where the time history of C_x^n and C_x^τ are shown for all the cases with two wings with $AR = 2$. The contribution of C_x^n (Figure 4.2*a*) corresponds to thrust during most of the cycle, while the contribution of C_x^τ (Figure 4.2*b*) always corresponds to drag. This suggests that the pressure forces are responsible for the lift and the thrust contributions generated by the wing during the downstroke. The thrust provided by the normal forces increases with $\langle\alpha_e\rangle$, the same as C_z in Figure 4.1*a*. Note that the two cases with different R but same $\langle\alpha_e\rangle$ have roughly the same C_x^n, suggesting that the effect of R on the surface integral of the pressure forces is limited in the cases with the same AR.

Interestingly, the contribution from the skin friction to the drag is larger for case AR2-R000, which shows in Figure 4.2*b* a fairly constant value of C_x^τ over the whole cycle. The time-averaged C_x^τ of cases AR2-R000 and 2W-Rinf* are almost the same, although the instantaneous values of C_x^τ of the latter present stronger oscillations than the former. In the cases with $h_0 = c$, as $\langle\alpha_e\rangle$ increases, C_x^τ decreases during both the downstroke and the upstroke. Indeed, the effect of $\langle\alpha_e\rangle$ on the contribution from the tangential forces seems to be larger than on the contribution from the normal forces, with absolute variation between AR2-Rinf and AR2-R000 of 0.11 and 0.06 for C_x^τ and C_x^n, respectively. Finally, it is interesting to note that the dependence of the time to $C_{x,\max}$ with $\langle\alpha_e\rangle$ is associated to the tangential force contribution (compare Figures 4.1*a* and 4.2*b* around $t/T = 0$ and 0.5).

4.2 Tangential force distribution

The analysis of C_i^n and C_i^τ in the previous section seems to suggest that R and $\langle\alpha_e\rangle$ affect differently normal (pressure) and tangential forces (skin friction). In this section, we focus on the latter, specifically on the contributions to C_x^τ from the different parts of the wing. To that end, we define

$$c_x^\tau(x_w) = \frac{1}{bc}\int_0^b \int_0^{x_w} c_\tau(\xi,\eta)\,\boldsymbol{\tau}\cdot\mathbf{e}_x \mathrm{d}\xi\mathrm{d}\eta, \tag{4.6}$$

where $\boldsymbol{\tau}$ is a local unit vector tangent to the wing surface pointing towards the streamwise direction, as shown in Figure 3.1*d*, x_w is the chordwise coordinate on the reference frame of the wing and $c_\tau(x_w, y_w)$ is the local tangential force coefficient on the wing surface,

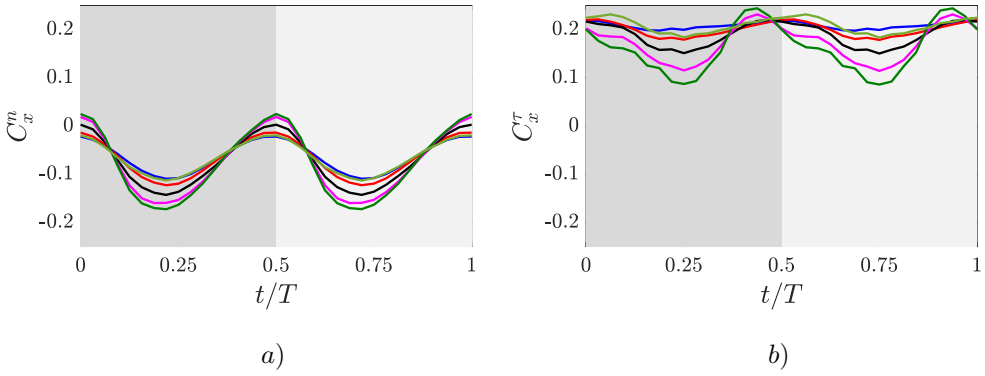

a) *b)*

Figure 4.2: Streamwise force coefficient *a)* normal (C_x^n) and *b)* tangential (C_x^τ) components during one cycle of the cases with two wings AR2-R000 ( ), AR2-R005 ( ), AR2-R020 ( ), AR2-R080 ( ), AR2-Rinf ( ) and AR2-Rinf* ( ). Dark and light greys regions represent downstroke and upstroke motions respectively. Note that the vertical scale has been chosen so that Figures can be compared with Figure 4.1*b*

defined as

$$c_\tau = \frac{\mathbf{f}_\tau \cdot \boldsymbol{\tau}}{\frac{1}{2}\rho {u_\infty}^2}. \tag{4.7}$$

Note that the surface integral in equation (4.6) extends over the whole span of the wing, and from the leading edge to the chordwise coordinate x_w both over the upper and lower surfaces of the wing. From a physical point of view, $c_x^\tau(x_w)$ is the contribution to C_x^τ from the surface of the wing located between the leading edge and the chordwise coordinate x_w, so that $c_x^\tau(c) = C_x^\tau$.

Figure 4.3*a* shows $c_x^\tau(x_w)$ at the mid-downstroke ($t/T = 0.25$), the time instant when the differences in C_x^τ in Figure 4.2 are maxima. Near the leading edge of the wing, $c_x^\tau(x_w)$ presents a minimum for all the cases. This peak value decreases with R for all the cases with the same h_0 and is similar for the cases with the same $\langle\alpha_e\rangle$ (AR2-R000 and AR2-Rinf*). After that minimum, $c_x^\tau(x_w)$ grows with x_w at a similar rate for all the cases. This suggests that the differences in C_x^τ observed in Figure 4.2*b* are mainly due to the behaviour of the flow close to the leading edge of the wing.

In order to evaluate the origin of these negative contributions to C_x^τ (i.e., thrust due to skin friction) near the leading edge of the wing, Figures 4.3*b* and 4.3*c* show the relative velocity at the mid-span of the wing at mid-downstroke for cases AR2-R000 and AR2-Rinf, respectively. In both Figures, the stagnation point can be identified in the pressure side of the wing, in the region between the two spanwise vorticity contour lines shown in blue (clockwise) and red (anticlockwise). These plots show that the negative

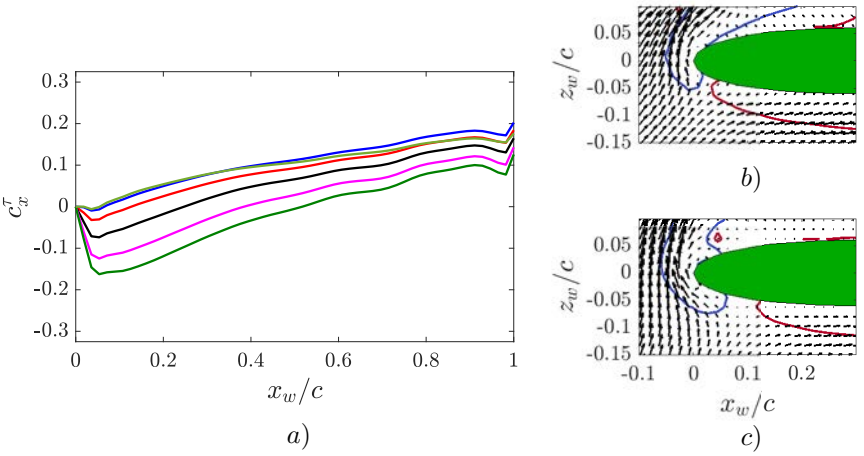

Figure 4.3: *a*) Streamwise contribution of the local tangential force coefficient (c_τ) to C_x^τ as a function of x_w at the mid-downstroke ($t/T = 0.25$). AR2-R000 ( ), AR2-R005 ( ), AR2-R020 ( ), AR2-R080 ( ), AR2-Rinf ( ) and AR2-Rinf* ( ). *b*) and *c*) relative velocity field at the wing span section $y_w/b = 0.5$ for cases AR2-R000 and AR2-Rinf, respectively. Two spanwise vorticity contour lines ($\omega_y c/u_\infty = 5$ and $\omega_y c/u_\infty = -5$) are shown in blue and red, respectively. The wing section is displayed in green.

peak of $c_x^\tau(x_w)$ for $x_w \lesssim 0.1c$ is due to the skin friction of the boundary layer developing from the stagnation point to the leading edge of the wing. Since the stagnation point is located further away from the leading edge for the case AR2-Rinf than for case AR2-R000, the minimum of $c_x^\tau(x_w)$ of the former has a larger absolute value than the latter. Although not shown here, the stagnation point for the heaving case (AR2-Rinf*) with equal $\langle\alpha_e\rangle$ than AR2-R000 is located at the same x_w than the latter, resulting in a similar magnitude of the negative peak in $c_x^\tau(x_w)$ in Figure 4.3*a*. Therefore, independently of R, the results shown in Figure 4.3 suggest that in sections with larger α_e, the flow moves faster around the leading edge (from the pressure side to the suction side), generating more thrust. This faster flow also results in a normal suction force at the leading edge, which will be discussed below.

4.3 Normal force distribution

We now turn our attention to the vertical force. Unlike the streamwise force, the vertical force is dominated by the contribution of the normal force, which represents almost 90% of the total C_z in the cases studied. Thus, in order to better characterize the combined effect of R and α_e on C_z, the distribution of the normal force on the surface of the wing

is analyzed first. This distribution is studied in the lower and upper surfaces separately, to allow the detailed analysis of the effect of the LEV on C_z. First, the local normal force coefficient given by

$$c_n = \frac{\mathbf{f}_n \cdot \mathbf{n}}{\frac{1}{2}\rho {u_\infty}^2}, \tag{4.8}$$

is characterized at the mid-downstroke ($t/T = 0.25$, see Figure 4.4), approximately when aerodynamic forces are maxima. Note that c_n is analogous to the (minus) pressure coefficient: positive c_n corresponds to suction, which results in positive contributions to the lift in the upper surface and negative contributions to the lift in the lower surface.

The c_n distributions displayed in Figure 4.4 show that suction is dominant in the upper surface, while positive pressure (i.e., negative c_n) is dominant in the lower surface. Very close to the leading edge, c_n tends to be positive both in the upper and lower surface, which explains the negative sign of C_x^n (thrust) in Figure 4.2*a* at mid-downstroke. Near the trailing edge, the sign of c_n tends to change. Note however that this occurs in the region where the distance between the upper and lower surface is too small for the IBM to provide accurate surface distributions of the force (as discussed in section 3.3).

For $R \to \infty$ (AR2-Rinf, see Figure 4.4*i* and 4.4*j*), the c_n distribution is roughly symmetric with respect to the mid-span of the wing. In the cases with $h_0 = c$, the magnitude of c_n in the inboard wing tip ($y_w = 0$) decreases with R, resulting in a force distribution along the spanwise direction that peaks near the outboard wing tip Indeed, the local normal force distribution near the outboard wing tip is qualitatively the same in these five cases with $AR = 2$, although the intensity of the suction peak in the upper surface slightly increases with R. The c_n distribution in the lower surface is more uniform than over the upper surface, although the effect of α_e on the spanwise distribution of c_n is clearly discernible too. Note that, besides the apparent differences in the c_n distribution in the upper and lower surfaces, both surfaces of the wing contribute in a similar percentage to C_z.

Finally, Figure 4.4 shows that $\partial c_n/\partial x_w \lesssim 0$ over the upper surface, which is consistent with an adverse pressure gradient (as typically observed in the suction side of wings). As R decreases, this adverse pressure gradient is relieved in the region close to the inboard wing tip, where the effective angle of attack becomes smaller. Besides that, all cases shown in Figure 4.4 exhibit a region with $\partial c_n/\partial x_w \approx 0$ on the upper surface of the wing (i.e., the region where the x_w distance between consecutive iso-lines of c_n is larger, highlighted with a red dashed rectangle in Figure 4.4). This region is located around the mid-span of the wing for case AR2-Rinf, but moves towards the outboard wing tip as R decreases. The fact that $\partial c_n/\partial x_w \approx 0$ could be an indicator of the presence of a stagnation region where the boundary layer is separated or the flow is recirculating. In the lower surface of the wing, the chordwise gradients of c_n are smaller but positive,

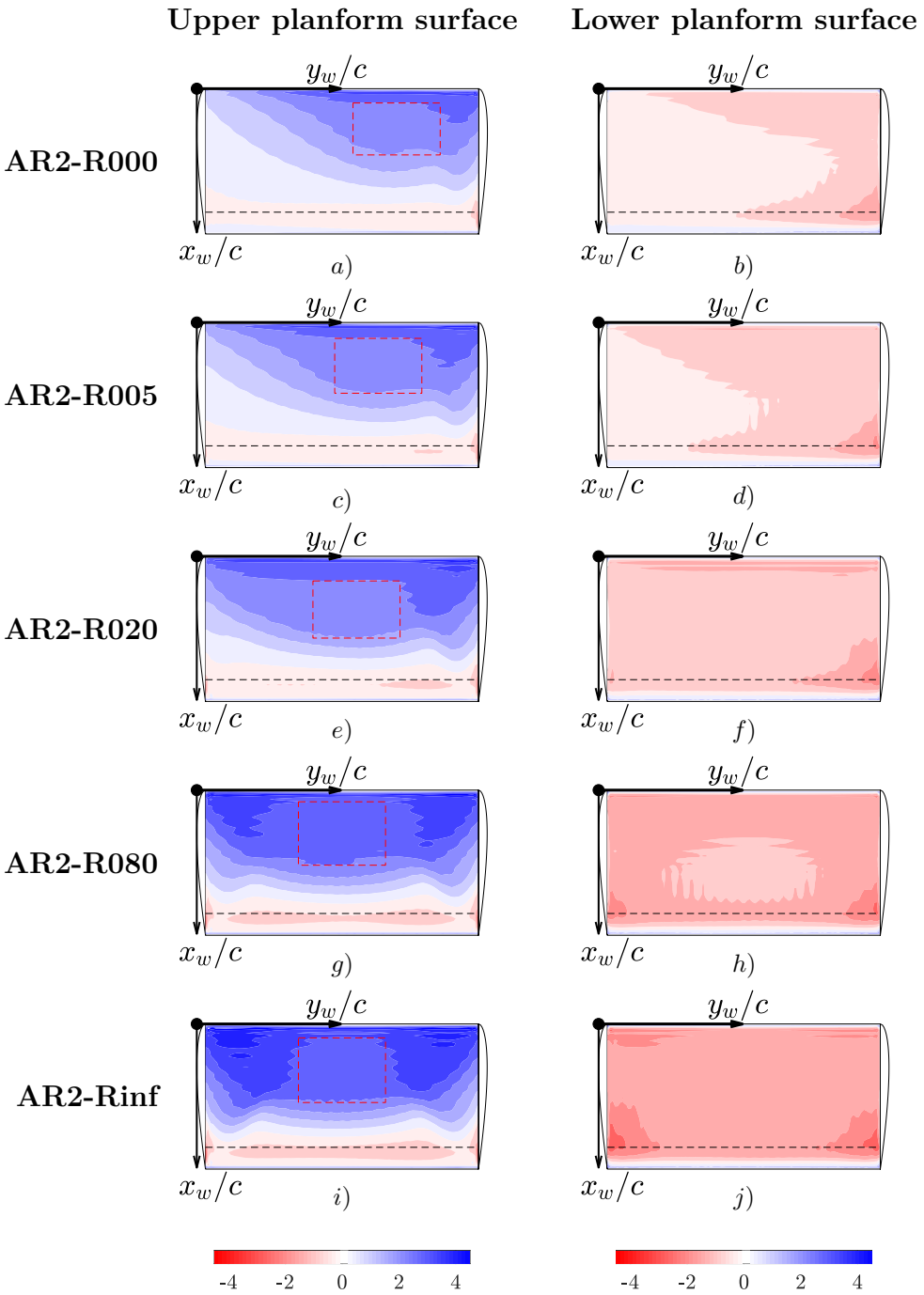

Figure 4.4: Distribution of the local normal force coefficient (c_n) at the mid-downstroke. (a), (c), (e), (g), (i) upper surface. (b), (d), (f), (h), (j) lower surface. (a)-(b) Case AR2-R000. (c)-(d) Case AR2-R005. (e)-(f) Case AR2-R020. (g)-(h) Case AR2-R080. (i)-(j) Case AR2-Rinf. The red dashed rectangle indicate approximately the regions where $\partial_x c_n \approx 0$. The black dashed line at $x_w/c = 0.85$ limits the region where the IBM is not providing an accurate description of c_n, as discussed in section 3.3.

resulting in a slightly favorable pressure gradient in most of the wing (except near the wing tips), showing no indication of separation of the boundary layer.

These interpretations of the distributions of c_n over the upper surface of the wing are supported by flow visualizations. This is clearly visible in corresponding animations (not shown) an in Figure 4.5 for the mid-downstroke of all cases $h_0 = c$. The left row of panels in Figure 4.5 shows vortical structures, identified using two isosurfaces of the second invariant of the velocity gradient tensor Q, namely the Q-criterion of Hunt et al. [1988]. The two isosurfaces of Q shown in the Figure correspond to $Q = \sigma/8$ (light blue) and $Q = \sigma/4$ (dark blue), where σ is the standard deviation of Q calculated in a box of size $2.5c \times 4.5c \times 3c$, centered at $x_w/c = 0.5$ and $y_w/c = z_w/c = 0$. Note that the value of Q can be interpreted as a measure of the intensity of the vortex, hence light blue structures correspond to weak vortices, while dark blue structures (surrounded by a light blue isosurface) correspond to intense vortices. The central and right rows of the Figure show the spanwise vorticity (ω_{y_w}) at two x_w-z_w planes, $y_w/b = 0.5$ (mid-span) and $y_w/b = 0.75$ (closer to the outboard wing tip), respectively. For reference, these x_w-z_w cuts also include the iso-contours of $Q = \sigma/4$, plotted in dark blue in the left row. Note that positive ω_{y_w} (blue) corresponds to clockwise rotating vortices.

The following remarks concerning the overall evolution of the vortices in the upper and lower surfaces of the wings are based on careful observations of flow animations (not shown here). Some of the phenomena are also visible in the Figures shown below. As the downstroke begins, a strong LEV forms in the upper surface of the wing, flanked by wing tip vortices. The structure of these vortices at mid-downstroke ($t/T = 0.25$) can be observed in the left row of Figure 4.5. The wing-tip vortices are clearly visible in the outboard wing tip of the five cases, but their intensity (i.e., volume of the Q isosurfaces) in the inboard wing tip quickly decreases with R, due to the reduced pressure difference between the pressure and suction sides in that region (i.e., see c_n distributions near the inboard wing tip in Figure 4.4). At or close to the stroke reversal ($t/T = 0.5$), the LEV and the tip-vortices are shed into the wake, generating the ring-like structures that can be observed in the wakes shown in the left row of Figure 4.5. These ring-like vortices are very similar to those reported in previous works [Guerrero, 2010, Von Ellenrieder et al., 2003, Triantafyllou et al., 2004]. For relatively large radius of flapping motion, $R/c \gtrsim 2$, these ring-like vortices are quite symmetric (see Figures 4.5g, 4.5j and 4.5m), becoming less clear for AR2-R005 and AR2-R000.

Besides the wing-tip vortices of the inboard wing tip and the ring-like structures in the wake, the radius of flapping motion R and the effective angle of attack α_e have a strong influence on the structure of the LEV. At the mid-downstroke, the left row of Figure 4.5 shows that the LEV becomes less intense (i.e., smaller volume in the Q isosurface) in the inboard side of the wing as R and α_e decrease. However, its structure near the outboard wing tip, where α_e is similar for the cases with $h_0 = c$,

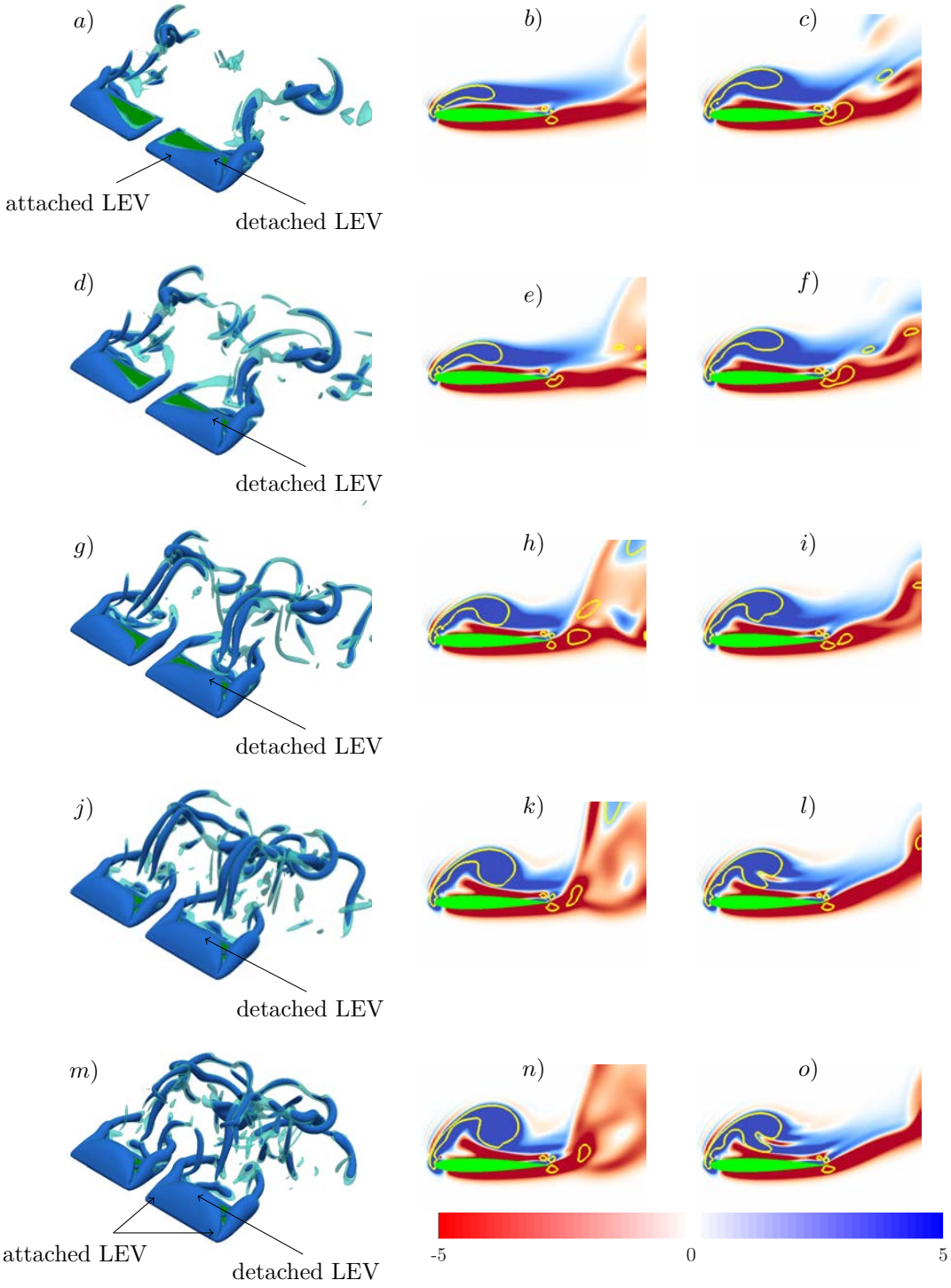

Figure 4.5: (caption in the facing page)

Figure 4.5: Flow visualization at $t/T = 0.25$ of cases AR2-R000 (a, b, c), AR2-R005 (d, e, f), AR2-R020 (g, h, i), AR2-R080 (j, k, l) and AR2-Rinf (m, n, o). In the left panels two different isosurfaces of $Q = \sigma/8$ (light blue) and $Q = \sigma/4$ (dark blue) are shown. In the central (right) panels, x_w-z_w cuts of the spanwise vorticity at $y_w/b = 0.5$ ($y_w/b = 0.75$) are shown in a red-blue colormap. The yellow line represents the x_w-z_w cut of the dark blue isosurface of Q shown in the left panels. Wings are displayed in green.

remains practically unchanged. This variation is qualitatively similar to that reported in previous works for revolving wings [Jardin et al., 2012, Jardin and David, 2014, Bross and Rockwell, 2014, Carr et al., 2013, Harbig et al., 2014].

The weakening of the LEV in the inboard wing tip for cases with small R is consistent with the distribution of $\alpha_e(y_w, t)$. It also correlates with the evolution of the c_n distributions in the upper surface of the wing (Figure 4.4). This is indeed expected, since previous studies have associated the suction peaks near the leading edge to the LEV [Visbal, 2011a, 2012, Chen and Skote, 2015]. For the present cases, the x_w-z_w cuts shown in Figure 4.5 display that the LEV is indeed being shed into the wake shortly after mid-downstroke, and that the region where this occurs moves towards the outboard wing tip as R decreases (i.e. where α_e is higher). This is also visible in corresponding animations (not shown). For instance, it is possible to observe in Figure 4.5k and 4.5n that cases AR2-R080 and AR2-Rinf have a separated LEV at mid-span, in the sense of having an LEV relatively far from the wing surface. However, at the same spanwise section, Figure 4.5b shows a developing LEV for case AR2-R000, which could be considered to be attached (i.e., closer to the wing surface). Closer to the outboard wing tip, at $y_w/b = 0.75$ (see Figure 4.5c), the LEV is located further away from the wing surface, with a distribution of vorticity beneath the vortex similar to that shown in Figure 4.5k and 4.5n, suggesting that the LEV is separated. Although not shown, closer to the outboard wing tip, the contours of Q become closer to the surface of the wing, suggesting that the LEV remains anchored to the wing in that region. Indeed, the left row of Figure 4.5 seems to suggest that the tip vortices, when present, act as an anchoring structure for the LEV, as suggested by Birch and Dickinson [2001]. Summarizing, the LEV separates at the mid-span for $R \to \infty$, while separation occurs closer to the outboard wing tip as R decreases.

After analyzing qualitatively the influence of R and $\langle \alpha_e \rangle$ on the LEV separation and how it correlates with the normal force distribution on the upper surface of the wing, we proceed with a more quantitative analysis. Recall that the lift increases while the LEV is attached to the wing [Saffman and Sheffield, 1977, Pitt Ford and Babinsky, 2013], C_z increases with α_e (as shown in Figure 4.1a) and depends mainly on the contribution from the pressure forces (i.e. normal forces). Then, it might be considered that the local

separation of the LEV at a given spanwise wing section occurs when the contribution of c_n to the vertical force at that section peaks (and drops) before the maximum α_e is reached (at the mid-downstroke, $t/T = 0.25$).

In Figure 4.6*a*, the contribution of the local normal force coefficient to the vertical force

$$c_z^n(y_w, t) = \frac{1}{c}\int_0^c c_n(\xi, t)\,\mathbf{n}\cdot\mathbf{e}_z \mathrm{d}\xi, \tag{4.9}$$

is shown during the downstroke at two sections along the span ($y_w/b = 0.5$ and $y_w/b = 0.75$). Three cases are shown in the Figure, namely, heaving (AR2-Rinf), flapping (AR2-R000) and an intermediate configuration (AR2-R020). The corresponding flow in these two sections at mid-downstroke is shown in the middle and right panels of Figure 4.5, in the top, middle and bottom rows. For the heaving case, $c_z^n(y_w = 0.5b, t)$ peaks at $t/T \approx 0.2$, well before mid-downstroke. On the other hand, closer to the outer wing tip the peak of $c_z^n(y_w = 0.75b, t)$ occurs later, closer to the mid-downstroke. These observations suggest that the LEV separates first in the mid-span of the wing, and later closer to the wing tips. Interestingly, the behavior of the flapping case with $R = 0$ (AR2-R000) is the opposite, suggesting that for this case the separation of the LEV starts closer to the wing tips. For the intermediate case, the peak of c_z^n is achieved roughly at the same time at both locations, $y_w = 0.5b$ and $y_w = 0.75b$. Overall, the results in Figure 4.6*a* seem to suggest that, as observed qualitatively in Figure 4.5, the location where the separation of the LEV occurs can be found closer to the outboard wing tip as R decreases.

To better characterize this behavior, the time to maximum c_z^n at each spanwise section, $t_{c_z^n,max}$, is shown in Figure 4.6*b* (i.e., the time when the separation of the LEV starts at each spanwise section). In agreement with the discussion of Figure 4.6*a*, the heaving case (AR2-Rinf) shows a roughly uniform region around mid-span (i.e., $0.6 \lesssim y_w/c \lesssim 1.4$) where the LEV separation occurs at about $0.2T$. Note that the spanwise extension of this region roughly corresponds to that of the region with $\partial c_n/\partial x_w \approx 0$ in Figure 4.4 (highlighted with the red rectangle). As R decreases, the region where the maximum of c_z^n is attained first can be found closer to the outboard wing tip, consistently with the previous discussion. Moreover, for the case AR2-R000, the maximum of c_z^n in the region $y_w \lesssim 0.5b$ occurs at mid-downstroke, which could be interpreted as sections where the separation of the LEV is very weak (or inexistent).

4.4 Comparison with unsteady panel methods

While direct numerical simulations provide accurate predictions of the aerodynamic forces on flapping wings, their computational cost is extremely high for practical applications. It is therefore interesting to explore the ability of less expensive methods, as

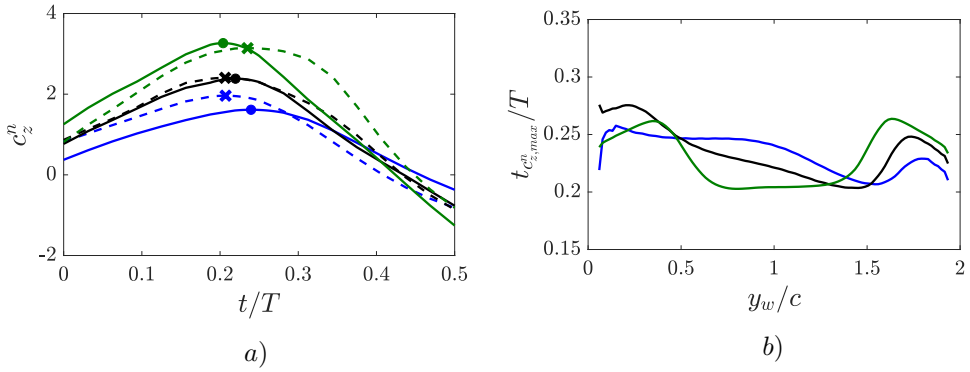

Figure 4.6: *a*) Contribution of the local normal force coefficient to the vertical force, $c_z^n(y_w, t)$. Two spanwise sections are considered, $y_w/b = 0.5$ (——) and $y_w/b = 0.75$ (- - -). *b*) Time to maximum c_z^n ($t_{c_{z,max}^n}$), plotted as a function of the spanwise coordinate of the wing (y_w). The cases represented in both Figures are AR2-R000 (——), AR2-R020 (——) and AR2-Rinf (——).

unsteady panel methods (UPMs) [Katz and Plotkin, 2001] to predict the aerodynamic forces on flapping wings. These methods are based on a potential description of the velocity field that assumes that the Reynolds number of the flow is sufficiently high, the flow is incompressible and the incoming free-stream is irrotational. Despite these strict assumptions, UPMs have been used by several authors to study flapping flight of birds and insects [Vest and Katz, 1996, Long and Fritz, 2004, Persson et al., 2012, Roccia et al., 2013], and some of the limitations of UPMs for the modeling of Micro Air Vehicles have been already discussed in the literature [Ansari et al., 2006]. In this section, we report the aerodynamic forces obtained for the present configuration using the UPM of Arranz and Flores [2016]. The results of the UPM are compared to the DNS results presented in the previous section, to evaluate the appropriateness of a UPM to model the aerodynamic forces in the present case.

The UPM of Arranz and Flores [2016] uses an indirect formulation, discretizing the 3D surface of the wing with trapezoidal panels with uniform distributions of sources and doublets. The wake is allowed to move with the flow, adjusting the doublets in the panels shed into the wake at each time step imposing the Kutta condition at the wing trailing edge. After being shed, the intensity of the doublets in the wake panels remains constant. The interested reader can find further details in Arranz and Flores [2016]. It should be noted that the present implementation of the UPM only considers a vortex sheet shed at the trailing edge, while other methods also consider a vortex sheet shed at the leading edge [Roccia et al., 2013]. The latter strategy allows a certain level of modelling of the LEV, which is not available in the present implementation of the UPM.

As discussed below, this will have a strong effect on the prediction of the suction force at the leading edge.

For the present calculations, the resolution is the same as in Arranz and Flores [2016], discretizing the wings with $M_x \times M_y = 24 \times 32$ panels in each wing, and truncating the wake $12c$ downstream of the trailing edge. All configurations with two $AR = 2$ wings and $h_0 = c$ (see Table 4.1) have been simulated, but for brevity only the cases AR2-R000, AR2-R020 and AR2-Rinf are discussed below.

For the comparison between the DNS and the UPM, and since viscous effects are absent in UPMs, only the contribution from the normal forces (C_z^n and C_x^n) are considered. These two quantities are displayed in Figure 4.7 as a function of time during one cycle, together with the lift and drag coefficients obtained with the UPM. Concerning the lift coefficient, Figure 4.7*a*, the agreement between DNS and UPM is remarkable. Both the shape of the profile and the intensity of the peaks are well predicted by the UPM. On the contrary, the UPM fails to provide a good estimation of the drag coefficient, as shown in Figure 4.7*b*. While the peak thrust coefficient (due to normal forces) predicted by the DNS is small, $C_x^n \approx -0.15$ (see Figure 4.2*a*), a much larger value is predicted by the UPM, C_x^n between -0.5 and -1.5 depending on the case considered. Only during the stroke reversals, when the velocity of the wing due to the flapping motion is close to zero, both DNS and UPMs provide similar values for the drag coefficient. At that time instant, the UPM sheds a strong vortex into the wake [Arranz and Flores, 2016], resulting in a vortical structure qualitatively similar to that observed in Figure 4.5, which seems to be correlated with the similarities observed in C_z^n between the UPM and the DNS.

The fact that C_z^n is well predicted by the UPM but C_x^n is not hints that the distribution of c_n in the DNS and UPMs are different. This is confirmed in Figure 4.8, which displays contours of c_n in the upper surface of the wing for AR2-Rinf and AR2-R000 at mid-downstroke. Figure 4.8 shows that, although the UPM captures qualitatively the spanwise changes in the force distribution, the chordwise distribution of c_n are very different for both AR2-Rinf and AR2-R000. Indeed, the UPM predicts a suction area (positive c_n) confined to a small region near the leading edge of the wing (note the saturation of the color scale in Figure 4.8*b* and 4.8*d*). However, the DNS data show larger suction regions, covering more than 2/3 of the wing surface (Figure 4.8*a* and 4.8*c*). Hence, while the maximum c_n for the DNS calculations of AR2-Rinf is $c_n \sim 4$, located at $x_w/c \sim 0.04$ and $y_w/c \sim 0.08$, the maximum in the UPM simulations is ten times larger ($c_n \sim 40$) and is reached at $x_w/c \sim 0.01$ and $y_w/c \sim 1.20$. A similar observation can be done for case AR2-R000. Note that this implies that the UPM shows a stronger suction peak closer to the leading edge, where the local $\mathbf{n}$ is reasonably aligned with $\mathbf{e}_x$, explaining the difference of more than one order of magnitude in the C_x^n computed from DNS and UPM (see Figure 4.7*b*). Although not shown, the differences between DNS

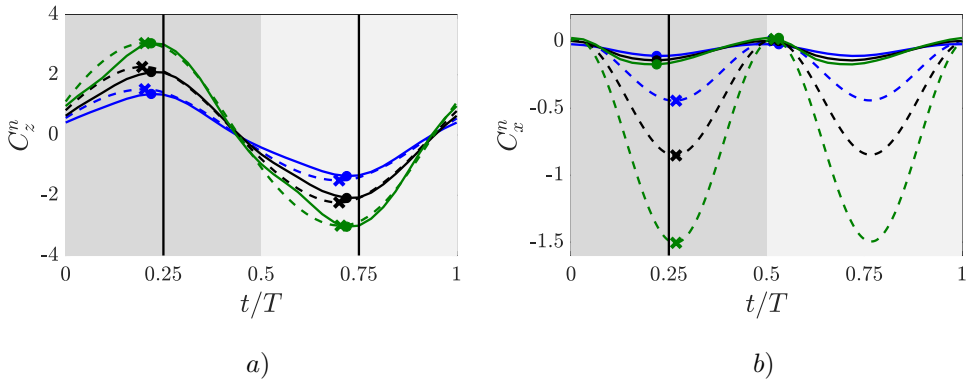

Figure 4.7: Normal force coefficients (*a*) C_z^n and (*b*) C_x^n of cases AR2-R000 (———), AR2-R020 (———) and AR2-Rinf (———) during one cycle. (———) lines represent DNS cases and (- - -) lines stand for 3D unsteady panel method simulations. Maximum and minimum values of the force coefficients are depicted with (●) for DNS simulations and with (✖) for 3D unsteady panel method simulations. Dark and light greys regions represent downstroke and upstroke motions respectively.

and UPM in the c_n distribution on the lower surface are less relevant.

It seems reasonable to assume that the differences in the c_n distributions between both methods are related to the presence of the LEV in the DNS (and its absence in the UPM). Indeed, the presence of the LEV in the DNS explains the broad suction peak near the leading edge, while in the UPM the need for an attached boundary layer at the leading edge results in a very strong suction peak close to $x_w \approx 0$. A bit more puzzling is the good agreement in terms of C_z^n between UPM and DNS, where the former is able to produce a spanwise distribution of bound circulation compatible with the overall pressure difference between suction and pressure surfaces in the DNS. It should be noted that the agreement in C_z^n between the DNS and the UPM in Figure 4.7 is worse during the first half of the stroke than during the second half. Interestingly, during the first half of the stroke the LEV is being developed, while it is shed into the wake shortly after the mid-stroke.

Finally, it is interesting to note that Moriche et al. [2017] reported that in 2D flapping airfoils the force due to circulatory effects is roughly perpendicular to the chord of the airfoil. A model for this phenomenon was proposed rather early by Polhamus [1966] in the framework of the separated leading edge vortices appearing on delta wings. This suggests that it should be possible to modify simple UPMs like the one used here to keep the component of the force perpendicular to the wing, discarding the component of the force along the chord (i.e. C_x^n in the present case).

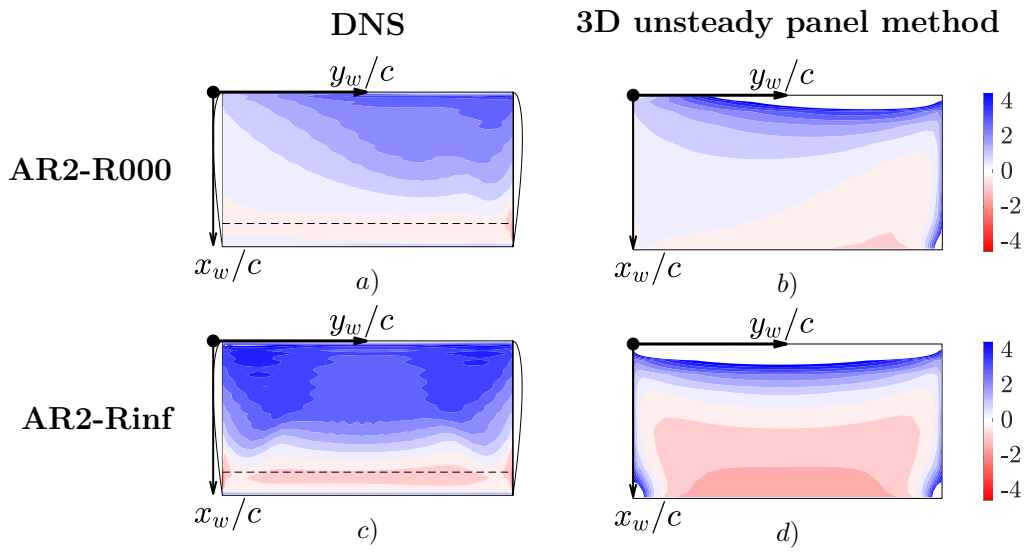

Figure 4.8: Normal force coefficient (c_n) at the mid-downstroke ($t/T = 0.25$), on the upper surface of the wing. (a) and (b), case AR2-R000. (c) and (d), case AR2-Rinf. Panels (a) and (c) show DNS results. Panels (b) and (d) show UPM results.

CHAPTER

FIVE

LEV identification method[1]

In the previous chapter, we have observed that the LEV is crucial for the generation of aerodynamic forces in flapping wings. In this chapter, we describe a methodology developed to provide a quantitative description of the LEV, which can be split in three steps. Section 5.1 explains the first step which consists of the identification of the vortical structures surrounding the wing using a vortex identification criterion. In the second step, described in 5.2, the core of the LEV is identified using a thinning algorithm. Then, chapter 5.3 details the process through which relevant flow quantities are computed along the LEV core, by averaging in planes perpendicular to the local vorticity at the LEV core points. After the detailed description of the algorithm, section 5.4 shows an application of this algorithm to the cases AR2-R000 and AR4-R000 described in chapter 3. The results show the robustness of the LEV identification method, and highlights the importance of the LEV development, motion and break up in the local force coefficients over the wing.

5.1 Identification of the vortical structure containing the LEV

Since the wing kinematics required to perform most of the relevant flight maneuvers in unsteady aerodynamics (forward flight, hover, perching,...) include one or more rotations, the flow surrounding the wing is typically studied in a non-inertial reference frame fixed to it. Then, the relative velocity $\mathbf{u}'$ at any point of the fluid ($\mathbf{r}$) is defined as

$$\mathbf{u}' = \mathbf{u} - \mathbf{u}_{O'} - \mathbf{\Omega} \times (\mathbf{r} - \mathbf{r}_{O'}), \tag{5.1}$$

where $\mathbf{u}$ is the absolute velocity of the fluid at $\mathbf{r}$, $\mathbf{u}_{O'}$ is the velocity of the origin of the non-inertial reference frame fixed to the wing (O'), $\mathbf{\Omega}$ is the instantaneous angular velocity of the non-inertial reference frame and $\mathbf{r}_{O'}$ is the position of O'. Taking the rotor of equation (5.1), the relative vorticity $\boldsymbol{\omega}' = \nabla \times \mathbf{u}'$ can be related to the absolute

[1] The contents of this chapter have been submitted for publication to the *Journal of Fluid Mechanics*.

vorticity $\boldsymbol{\omega} = \nabla \times \mathbf{u}$,

$$\boldsymbol{\omega}' = \boldsymbol{\omega} - 2\boldsymbol{\Omega}. \tag{5.2}$$

In order to define and identify the instantaneous vortical structures, the second invariant of the velocity gradient tensor of the relative velocity (Q') is used here [Hunt et al., 1988]. Hence, vortical structures are defined as 3D regions of the flow where $Q' > Q'_{th}$, as previously used in several works [Taira and Colonius, 2009, Visbal, 2011b,a, Visbal et al., 2013, Harbig et al., 2013, 2014, Jantzen et al., 2014, Jardin, 2017]. Note that in the present case, the choice of Q'_{th} is not trivial. The use of relative velocities imposes a lower bound on Q', which is related to the angular velocity of the wing, $\boldsymbol{\Omega}$. This lower bound is made explicit when Q' is expressed in terms of Q, the second invariant of the gradient of the absolute velocity,

$$Q' = Q + \|\boldsymbol{\Omega}\|^2 - \boldsymbol{\Omega} \cdot \boldsymbol{\omega}. \tag{5.3}$$

The direct consequence is that far upstream from the wing, where the velocity is homogeneous and both Q and $\boldsymbol{\omega}$ are zero, $Q' = \|\boldsymbol{\Omega}\|^2$. This is illustrated in Figure 5.1, where the probability density function (p.d.f.) of Q' upstream of the wing with $AR = 4$ is compared at two different instants: at the beginning of the downstroke ($t/T = 0$) when $\boldsymbol{\Omega}$ is zero, and at the mid-downstroke ($t/T = 0.25$) when $\boldsymbol{\Omega}$ is maximum. It can be observed that at both instants the p.d.f. peaks just before the value of $\|\boldsymbol{\Omega}\|^2$ at that time, indicated by the vertical dashed lines in the Figure. The value of the p.d.f. for $Q' > \|\boldsymbol{\Omega}\|^2$ in the region upstream of the wing is essentially zero at both instants. Therefore, the maximum value of $\|\boldsymbol{\Omega}\|^2$ during the cycle can be considered as the minimum value of Q'_{th}, necessary to avoid the identification of spurious vortical structures, generated exclusively by the choice of reference frame.

On the other hand, there is not an *a priori* limit on the maximum value of the threshold. Obviously, if the threshold is too high no vortical structures are detected. Hence, a certain range of Q'_{th} needs to be scanned to ensure the robustness of the method, as shown in the next section.

Finally, it should be noted that, as discussed by Chakraborty et al. [2005], the Q-criterion is equivalent to other identification methods (like the discriminant of the velocity gradient tensor, or the swirling strength) when appropriate thresholds are used. The present choice of the Q-criterion is based on the fact that this method only requires to calculate low order spatial derivatives of the velocity field and products of quadratic order, minimizing the computational resources and the time required by the algorithm. However, it has been checked that the results presented in the next sections are very similar when the λ_2 criterion is used, with an equivalent threshold in terms of the volume occupied by the identified vortical structures.

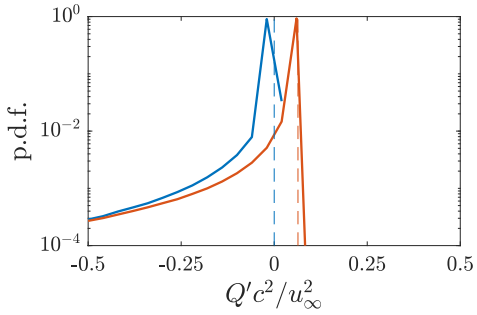

Figure 5.1: p.d.f. of Q' in a volume immediately upstream of the wing. Two time instants are shown, namely, the beginning of the downstroke, $t/T = 0$ (———) and the mid-downstroke, $t/T = 0.25$ (———). Dashed lines (- - -) and (- - -) represent the values of $\|\mathbf{\Omega}\|^2$ at $t/T = 0$ and $t/T = 0.25$, respectively.

Once a vortex identification method and a threshold has been selected, the next step in the LEV characterization method is to discriminate the vortical structure containing the LEV from other vortical structures in the flow (i.e., mostly the vortical structures shed to the wake in the previous flapping cycle). This is accomplished in the present study by computing Q' in a volume of fluid surrounding the wing, given by $x \in [-0.5c, 2c]$, $z \in [-1.5c, 1.5c]$ and $y \in [-1.25c, (1.25 + AR)\, c]$ Only the largest coherent object satisfying $Q' > Q'_{th}$ in this volume is kept for the next step. This procedure assumes that the LEV is the largest vortical structure in the region near the wing, which is always true for the present configurations. As an example, Figure 5.2*a* shows all the vortical structures identified with a threshold $Q'_{th} = 4{u_\infty}^2/c^2 \gg \|\mathbf{\Omega}\|^2$ for the case with $AR = 4$, while the translucent surface in Figure 5.2*b* corresponds to the vortical structure with the largest volume. It is important to note that the latter contains the LEV, but also the TiV around the outboard wing tip and a segment of a TEV.

5.2 Identification of the skeleton of the LEV

After the vortical structure is identified, the core or skeleton of the aforementioned structure is computed. This task is done with the thinning algorithm proposed by Lee et al. [1994] and implemented in MATLAB by Kerschnitzki et al. [2013]. The algorithm extracts the medial axes centerline of 3D objects, preserving their topological and geometrical conditions. Graphically, the process performed by the algorithm can be described as the peeling of an onion, being the onion the 3D object satisfying $Q' > Q'_{th}$ and the core of the onion its medial axes centerline. Voxels (volumetric pixels) at the

surface of the vortical structure are discarded, until only the set of points that define the skeleton of the vortical structure are left.

The skeleton provided by the thinning algorithm for the case used as an example in the previous subsection is shown in Figure 5.2*b* with red and green dots. The resulting skeleton follows reasonably well the overall shape of the vortical structure (i.e., the translucent object), although near the leading edge of the wing the skeleton shows extensive branching. The origin of this branching is related to the shape of the vortical structure in those locations, which resembles a cylindrical vortex joined to the leading edge by a thin shear layer. The chordwise oriented branches develop along this shear layer. This seems to be a spurious result of the thinning algorithm, and can be easily reproduced by applying the thinning algorithm to 3D objects obtained by joining a slender cylinder with a flat plate.

It is also clear from Figure 5.2*b* that not all of the points of the skeleton belong to the LEV. At the present threshold, the LEV is linked to the tip vortex (TiV) appearing on the outboard tip of the wing, and also to a section of a trailing edge vortex (TEV) shed at an earlier time. In order to discriminate the part of the identified core belonging to the LEV, we consider two geometrical criteria based on the position of the points of the skeleton, and the orientation of the vortical structure at these points.

The determination of the orientation of the vortical structure at each point of the skeleton is not completely trivial, since the distribution of points provided by the thinning algorithm is not smooth and the skeleton has branches. To avoid these difficulties, the orientation of the vortical structure is defined in terms of the direction of the local vorticity averaged in a region surrounding each point of the skeleton. Somewhat arbitrarily, this region is defined as the largest sphere inscribed in the isosurface $Q' = Q'_{th}$ and centered at each skeleton point. These spheres are defined as collections of voxels, and points in the skeleton whose corresponding sphere has only one voxel are discarded. The volume associated to the k-th point of the skeleton is denoted V_s^k, and the corresponding direction is denoted by the unit vector $\mathbf{n}_s^k$. These quantities are shown in Figure 5.2*c* for selected points along the skeleton of the vortical structure. It is interesting to note that points within the branches appearing near the leading edge of the wing have roughly the same direction of the local vorticity, basically pointing to the outboard wing tip. On the segments of the vortical structure that look like TiV and TEV, the local vorticity is mostly chordwise and spanwise (towards the inboard wing tip), respectively.

Once the local direction of the points of the skeleton of the vortical structures is defined and computed, the LEV points are defined as those satisfying the following conditions:

$$\left[\mathbf{n}_s^k - (\mathbf{n}_s^k \cdot \mathbf{e}_{z_w})\mathbf{e}_{z_w}\right] \cdot \mathbf{e}_{y_w} \leq \cos(\theta_{th}), \tag{5.4}$$

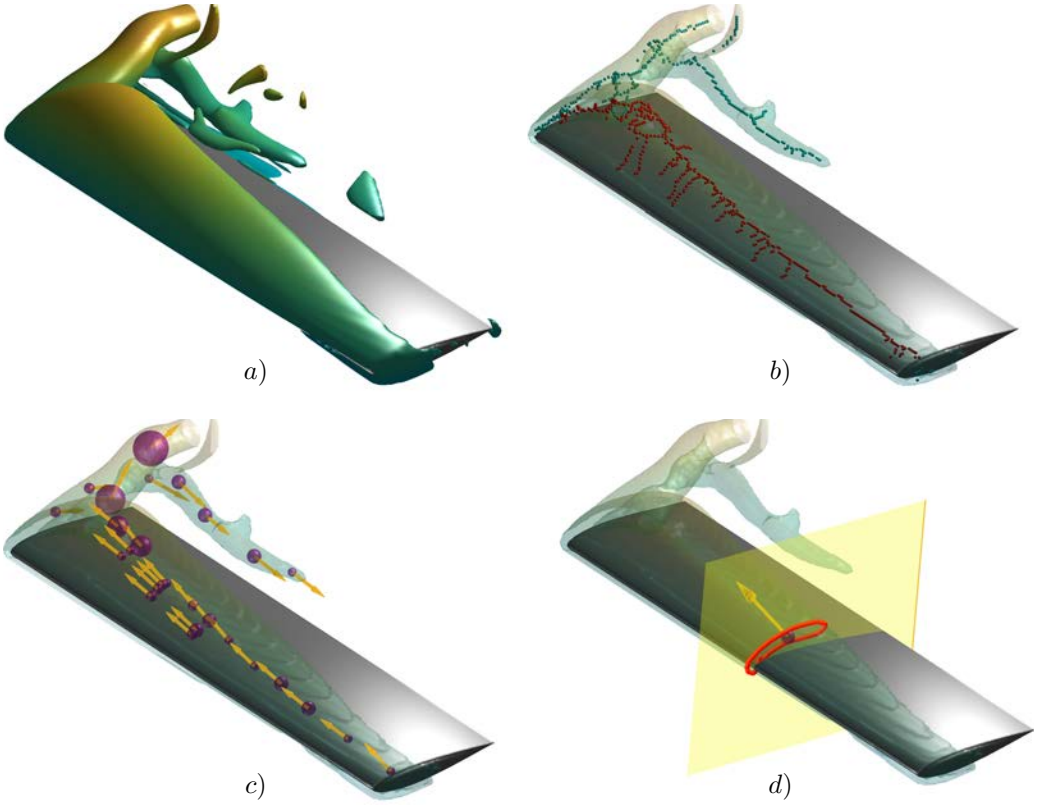

Figure 5.2: (*a*) Isosurface of $Q' = 4u_\infty^2/c^2$ at mid-downstroke ($t/T = 0.25$). (*b*) Skeleton of the vortical structure given by $Q' = 4u_\infty^2/c^2$ (translucent). Points corresponding to the LEV in red, rest in green. (*c*) Spheres (in magenta) inscribed in the $Q' = 4u_\infty^2/c^2$ isosurface, centred on selected points of the skeleton. The yellow arrows are $\mathbf{n}_s^k$, the direction of the relative vorticity averaged in the corresponding sphere. (*d*) Plane (in yellow) perpendicular to $\mathbf{n}_s^k$, for a particular point in the skeleton. The red contour corresponds to the boundary of $\mathcal{C}^k$ for that point of the skeleton.

$$z^k_{w,s} \geq 0, \tag{5.5}$$

where $z^k_{w,s}$ is the vertical coordinate of the k-th point of the skeleton. From a physical point of view, equation (5.4) requires that the angle between the spanwise direction of the wing (i.e., $\mathbf{e}_{y_w}$) and the projection of $\mathbf{n}^k_s$ onto the $x_w - y_w$ plane is smaller than a certain angle, θ_{th}. For moderate to small values of θ_{th}, this is equivalent to requiring that the direction of the vortex skeleton is more or less aligned with the spanwise direction. Note that this requirement originates in the rectangular shape of our wings. For more general wing geometries it might be convenient to consider the angle of $\mathbf{n}^k_s$ with a local direction parallel to the leading edge of the wing (i.e., with a θ_{th} varying with y_w). Finally, equation (5.5) discriminates points of the skeleton in the lower surface of the wing, since we are analyzing the downstroke only.

Figure 5.2*b* shows the result of applying these geometrical conditions on the core of the vortex, for a time corresponding to the mid-downstroke. Points satisfying equations (5.4) and (5.5), with $\theta_{th} = 30°$, are colored in red and they correspond to the section of the vortical structure that is easily identified with the LEV. Points failing to satisfy all conditions are colored in green, and they correspond to the TiV and TEV. It should be noted that, although not shown here, several values of θ_{th} have been tested in the present case. The observed differences where negligible when $25° \leq \theta_{th} \leq 60°$, except (maybe) at the end of the downstroke, when the displacement of the LEV is maximum (see discussion in section 5.4).

5.3 Computing averaged quantities along the LEV

The last step of the method is to evaluate flow variables along the LEV. This is done with a procedure analogous to that used in previous works [Jones and Babinsky, 2011, Jardin and David, 2014, Calderon et al., 2014, Arranz et al., 2018a]. At each point of the skeleton belonging to the LEV, a plane perpendicular to $\mathbf{n}^k_s$ is defined. The intersection of that plane with the volume satisfying $Q' > Q'_{th}$ is denoted $\mathcal{C}^k$ (shown in Figure 5.2*d*). Any physical variable of interest, φ, is averaged over $\mathcal{C}^k$ to provide φ^k_s. This applies to the velocity, vorticity and pressure. The local circulation in this plane is defined as

$$\Gamma^k_s = \int_{\mathcal{C}^k} \boldsymbol{\omega}' \cdot \mathrm{d}\boldsymbol{S}, \tag{5.6}$$

where $\mathrm{d}\boldsymbol{S}$ is the differential element of surface. Note that in previous works the chosen plane is a chordwise-vertical plane, which assumes a LEV aligned with the spanwise direction [Jones and Babinsky, 2011, Jardin and David, 2014, Calderon et al., 2014, Arranz et al., 2018a]. The present choice of plane is more general, allowing for a deformed LEV, reasonably aligned (i.e., see θ_{th} in equation 5.4) with the leading edge of the wing.

It should be noted that the objective of the method presented here is to provide a quantitative description of the LEV along its core. In the present case, the core is roughly aligned along the spanwise direction. Hence, the positions and physical quantities on the skeleton of the LEV, $(x^k_{w,s}, y^k_{w,s}, z^k_{w,s})$ and φ^k_s, are averaged in spanwise bins, to characterize the LEV as a function of the spanwise coordinate y_w and time. The position of the LEV core in a spanwise bin of width H (i.e., $y_w \pm H/2$) is given by the point of the skeleton with the largest sphere volume, $V_{\max}(y_w) = \max(V^k_s)$. Since this volume is computed as a sum of voxels, it is possible to find several points within a bin with the same V^k_s. Hence, formally, the position of the LEV core, $\mathbf{x}_{w,c}$, is defined as the averaged position of the points of the skeleton inside the bin whose V^k_s is equal to the maximum V^k_s on the bin. Mathematically,

$$\mathbf{x}_{w,c}(y_w) = \frac{1}{N_k} \sum_k \mathbf{x}^k_{w,s} \quad \{k \mid y^k_{w,s} \in [y_w \pm H/2], V^k_s = V_{s,\max}(y_w)\}, \tag{5.7}$$

where N_k is the number of points in the skeleton satisfying the condition in equation (5.7). The same average is used to define physical quantities along the core (i.e., pressure, velocity, vorticity and local circulation),

$$\varphi_c(y_w) = \frac{1}{N_k} \sum_k \varphi^k_s \quad \{k \mid y^k_{w,s} \in [y_w \pm H/2], V^k_s = V_{s,\max}(y_w)\}, \tag{5.8}$$

Note that the definitions of $x_{w,c}$ and φ_c in equations (5.7) and (5.8) are explicitly designed to deal with the branching appearing in 5.2. The points in the branches usually have smaller spheres (i.e., smaller V^k_s), as the vortical structure around them is thinner. Since the core of the LEV is expected to be associated to the thicker region of the vortical structure, the definition of the position of the LEV core ($x_{w,c}$ in equation 5.7) and the physical quantities inside it (φ_c in equation 5.8) only considers the largest spheres in the bin. However, the points along the chordwise branches have essentially the same orientation as the point at the intersections, as observed in Figure 5.2*c*. Hence, φ_c defined in equation (5.8) is virtually indistinguishable from a standard or volume-weighed average over all the points of the skeleton in the bin, due to the little variation of $\mathbf{n}^k_s$ along the branches.

5.4 Results

The identification method has been applied to two cases described in chapter 3 (AR2-R000 and AR4-R000). For both cases, the LEV skeleton is obtained at various instants during the downstroke using $\theta_{th} = 30°$. Several values of the threshold Q'_{th} have been used, to asses the effect that the threshold has on the characterization of the LEV. Finally, positions and physical variables along the vortex core are computed using equations (5.7) and (5.8) with spanwise bins of width $H = 4\Delta$, where $\Delta = c/56$ is the grid

spacing of the simulation. The uncertainty in the position of the LEV is measured with the maximum and minimum coordinates of all the points of the skeleton within a bin. The uncertainty in the physical variables (φ_c) is computed as the standard deviation of φ_s^k for all skeleton points inside two consecutive bins with respect to the mean value of φ_c in these two bins. These uncertainties are shown with shaded contours in the Figures below.

Figure 5.3 shows the streamwise ($x_{w,c}$) and vertical ($z_{w,c}$) position of the LEV core as a function of the spanwise coordinate at a fixed time instant, $t/T = 0.25$ (mid-downstroke). At that time instant the LEV is already developed. In fact, although not shown here, a peak of lift appears slightly before the mid-downstroke [Gonzalo et al., 2018]. Panels *a* and *b* of Figure 5.3 show that, for both cases, the LEV separates vertically from the wing close to the outboard wing tip. Panels *c* and *d* of Figure 5.3 show that the LEV core is found further downstream when increasing the spanwise coordinate, except very close to the wing tip. The uncertainty in the position of the LEV core is small except for $x_{w,c}$ in the region where the LEV is farther away from the wing and branching of the LEV skeleton is more apparent (see red points in Figure 5.2*b*). Comparing both cases, Figures 5.3*a* and 5.3*b* show that the maximum height of the LEV core seems to be independent of AR. This might be related to the design of the cases, both having the same vertical displacement of the outer wing tip. With respect to the streamwise position of the LEV core, it seems that there is indeed a non-negligible difference between the cases with $AR = 2$ and $AR = 4$ analyzed, panels *c* and *d* of Figure 5.3. However, this difference is difficult to quantify since it is of the same order as the uncertainty.

Next, the influence of the threshold in the position of the LEV core is assessed. Overall, the agreement observed in Figure 5.3 for the various thresholds is good. Note that $x_{w,c}(y_w)$ and $z_{w,c}(y_w)$ are rather irregular. However, the observed irregularities do not correspond to a drift when varying the threshold. The amplitude of these irregularities seems to be larger for $x_{w,c}$ than for $z_{w,c}$. This might be related to the shape of the LEV at this time instant (Figure 5.2*d*), which is thin along the vertical direction. Hence, the variations found in the streamwise position of the LEV core are not translated into its vertical position. It is also worth noting that, increasing the threshold, Q'_{th}, leads to smaller vortical structures. In the present case, this happens more clearly near the inboard wing tip, where the LEV is less intense. As a consequence, the LEV and the corresponding lines in Figure 5.3 become shorter in the spanwise direction with increasing threshold. Note also that the identification of a smaller LEV in this regions results in the LEV core appearing closer to the leading edge (i.e., near the inboard wing tip, $x_{w,c} \to 0$ as Q'_{th} increases).

In order to characterize the LEV some relevant flow quantities are analyzed along the LEV core. The variables considered here are the pressure, p_c, the local circulation,

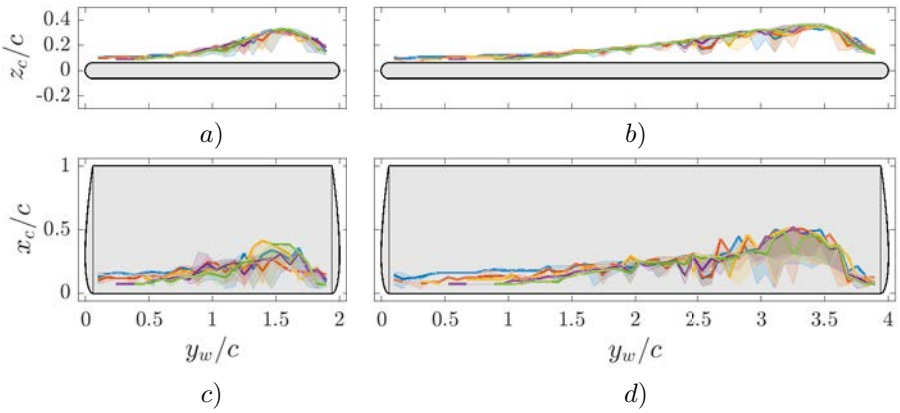

Figure 5.3: (a, b) Vertical and (c, d) streamwise coordinate of the LEV core along the wing span at mid-downstroke ($t/T = 0.25$). (a) and (c) correspond to $AR = 2$, (b) and (d) to $AR = 4$. Lines correspond to $Q'_{th}c^2/u_\infty^2 = 4$ ( ), $Q'_{th}c^2/u_\infty^2 = 6$ ( ), $Q'_{th}c^2/u_\infty^2 = 8$ ( ), $Q'_{th}c^2/u_\infty^2 = 10$ ( ) and $Q'_{th}c^2/u_\infty^2 = 12$ ( ). The colored shaded area indicates the uncertainty in the position of the LEV. The wing is displayed in grey.

Γ_c, and the vorticity and velocity components along the LEV core, $\omega_c = \boldsymbol{\omega}'_c \cdot \mathbf{n}_c$ and $u_c = \mathbf{u}'_\mathbf{c} \cdot \mathbf{n}_c$, respectively. These variables are of interest in the LEV dynamics, as shown by previous works [Birch et al., 2004, Jardin and David, 2014, Jardin, 2017, Arranz et al., 2018a]. Figure 5.4 shows the results for the case with $AR = 4$. As in the case of Figure 5.3, profiles corresponding to various thresholds are displayed. Figure 5.4a shows that p_c is minimum close to the outboard wing tip. Roughly at the same location, Γ_c is maximum (Figure 5.4c). On the other hand, the axial vorticity (Figure 5.4b) is more uniform, specially for the lower thresholds considered in the Figure. Finally, the axial velocity (5.4d) shows an outboard flow over most of the wing. In the region close to the outboard wing tip, the effect of the wing tip vortex yields an inboard flow (i.e., negative u_c).

In terms of the effect of the threshold, Figure 5.4 suggests that its effect is somewhat limited in pressure, velocity and circulation. This is more true for pressure and axial velocity than for the local circulation, since the latter is the result of an integral over an area that increases with Q'_{th}. Not surprisingly, the strongest dependency with the threshold is observed in the axial vorticity: increasing Q'_{th} results in a stronger LEV, and consequently the axial vorticity of the LEV increases. This dependency is more acute near the inboard wingtip, which suggests that the distribution of vorticity within the LEV is more uniform near the outboard wing tip. Finally, the uncertainty in pressure, local circulation, axial velocity and vorticity is small for all thresholds, except maybe

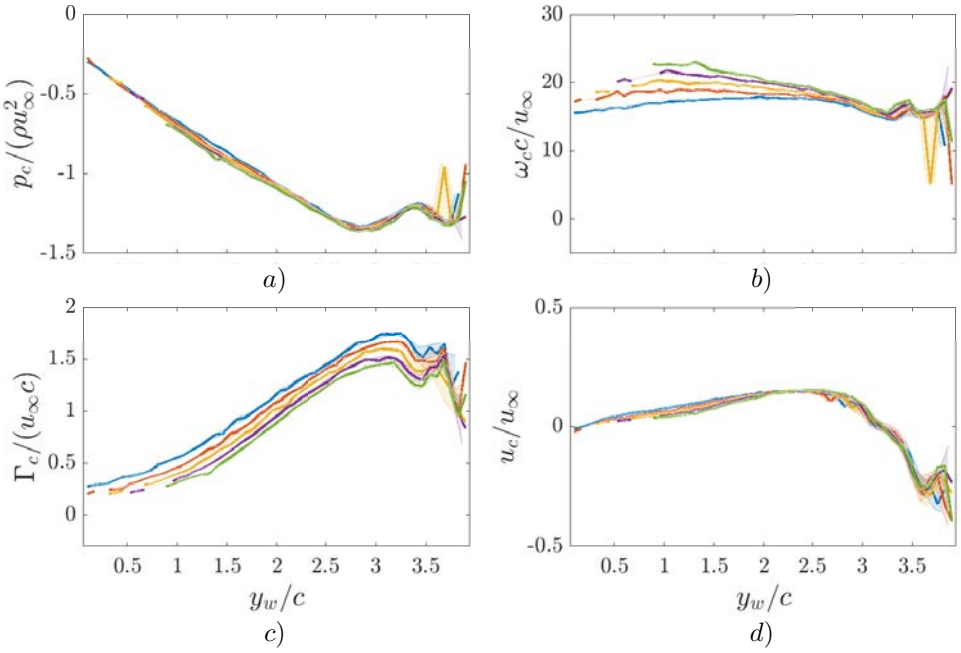

Figure 5.4: (*a*) Pressure inside the LEV. (*b*) Vorticity along the LEV core. (*c*) Local circulation. (*d*) Relative velocity along the LEV core. All quantities are shown as a function of y_w and are evaluated at mid-downstroke ($t/T = 0.25$). Colored lines as in Figure 5.3. The colored shaded area indicates the corresponding uncertainty.

near the outboard wing tip.

From the point of view of the characterization of the LEV over flapping wings, it is also necessary to address its evolution in time. Figure 5.5 shows the time evolution of $x_{w,c}$ and $z_{w,c}$ for the case with $AR = 4$, at three positions corresponding to 25, 50 and 75% of the span of the wing. Near the inboard wing tip (i.e., 25% of the span, see panels *a* and *b*), the LEV position changes little during the downstroke. The effect of Q'_{th} on the vertical position is small, while $x_{w,c}$ decreases as the threshold increases, as already discussed in Figures 5.3*b* and 5.3*d*. Note that in this spanwise section, the LEV is only detected in the interval $0.2 \lesssim t/T \lesssim 0.3$ (i.e., around mid-downstroke) for the highest threshold, while it is detected during (almost) the whole downstroke for the lowest threshold.

More interesting is the evolution of $x_{w,c}$ and $z_{w,c}$ in the 50 and 75% spanwise sections. During the first half of the downstroke the LEV moves downstream and vertically, with little uncertainty and scatter between the different thresholds. However, both uncertainty and scatter increase considerably around mid downstroke (i.e., $t/T = 0.25$). During the second half of the downstroke, $x_{w,c}$ moves downstream at a roughly constant velocity of about $0.4u_\infty$ (i.e., see black dashed line in Figures 5.5*c* and 5.5*e*). Meanwhile, $z_{w,c}$ increases and reaches a shallow maximum at a vertical distance from the wing that increases with y_w. Note that the vertical distance from the LEV core to the wing is relatively small ($z_{w,c} \lesssim 0.5c$ at 75%, and $z_{w,c,\max} = 0.63c$ at 76%), even if the chordwise motion of the LEV core seems to suggest that its kinematics are somehow detached from the wing's motion.

The origin of the uncertainty and the scatter in $x_{w,c}$ and $z_{w,c}$ during the second half of the downstroke is investigated in Figure 5.6. This Figure shows the points of the skeleton of the LEV in two spanwise bins, corresponding to 50% and 75% of the span of the wing. The points are represented by their corresponding inscribed spheres. The LEV is represented by the isosurface $Q' = 4{u_\infty}^2/c^2$ (translucent), as well as the intersection of the isosurface with chordwise-vertical planes at the sections 50% (blue) and 75% (orange) of the wing span. At $t/T = 0.25$, as already discussed above, the LEV shape is elongated in streamwise direction and thin in vertical direction. As time increases, the LEV evolves by growing in the downstream part while remaining thin near the leading edge. Eventually, a bottleneck is produced between the thicker part (downstream) and the thinner part, at $t/T \approx 0.3$. Somewhat later, pinch off takes place, so that the LEV splits into two structures, the first one remaining near the leading edge and the second one traveling downstream. This phenomenon does not happen simultaneously over the whole span, but rather it starts near the outer wing tip and progresses towards the inboard wing tip as time increases. Thus, pinch off is observed at $t/T \approx 0.34$ at 75% of the wing span and at $t/T \approx 0.4$ at 50% of the wing span. Note that these times are dependent on the particular Q'_{th} selected for the visualization.

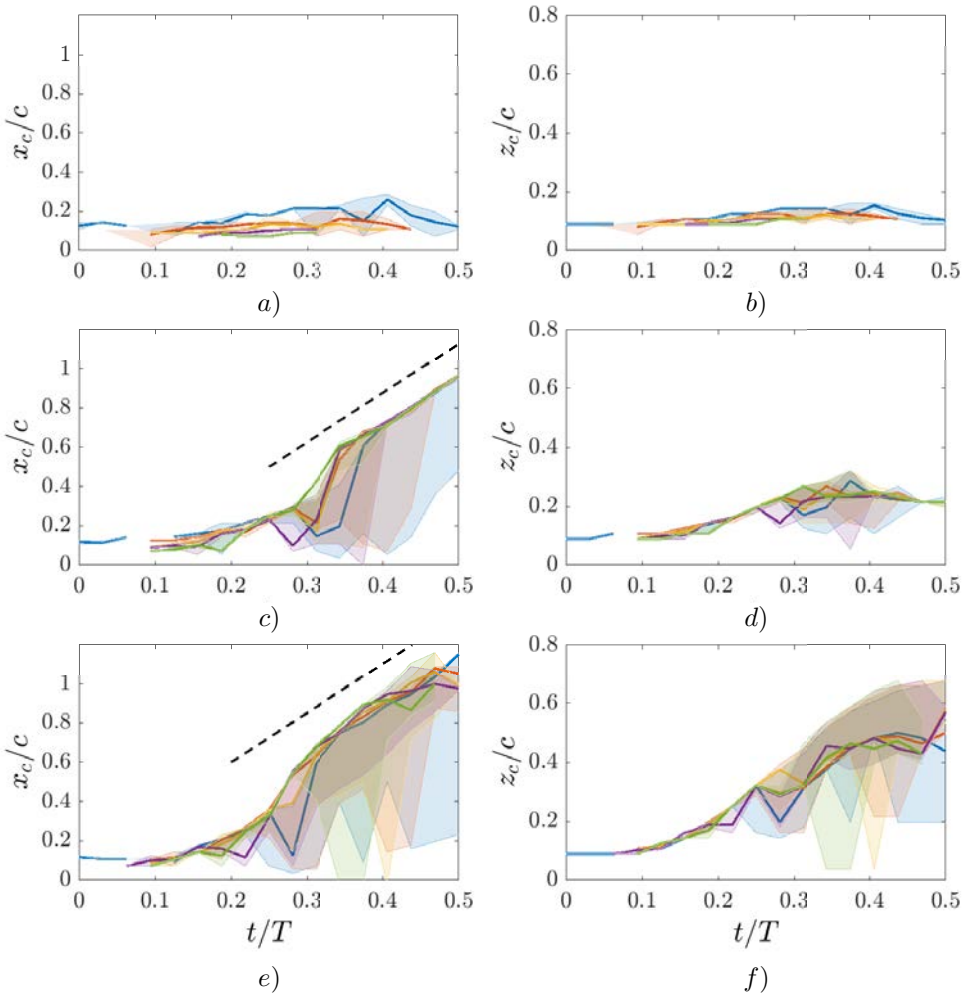

Figure 5.5: (a, c, e) Streamwise and (b, d, f) vertical coordinate of the LEV core for the case with $AR = 4$ as a function of time during the downstroke. The spanwise sections considered are $y_w = 0.25b$ (a, b), $y_w = 0.5b$ (c, d), and $y_w = 0.75b$ (e, f). Colored lines as in 5.3. The colored shaded area indicates the uncertainty in the position of the LEV. The black dashed lines in panels (c) and (e) are parallel to $x_{w,c} = 0.4u_\infty t$.

In summary, the LEV evolution can be described as an elongated structure in the spanwise direction that grows and splits with the shape of the letter "y", similar to that observed in previous works [Harbig et al., 2013, Jardin and David, 2014]. The weaker (i.e., smaller) leg remains close to the leading edge, and eventually disappears at the end of the stroke. The strongest (i.e., larger) leg of the vortical structure remains relatively close to the wing surface, traveling downstream at a roughly constant velocity. Note that near the end of the downstroke, the LEV branch that remains closer to the leading edge splits again (see Figure 5.6f).

Figure 5.6 also shows that the uncertainty in $x_{w,c}$ and $z_{w,c}$ observed in Figure 5.5 for the times and spanwise sections where the LEV is split is associated to the presence of points of the skeleton of the LEV in both branches of the "y"-shaped LEV. On the other hand, the effect of Q'_{th} on the time of the pinch off results in the aforementioned scatter in the lines in Figures 5.5c to 5.5f.

Although not shown here, a similar picture is obtained for the $AR = 2$ wing: the development of a "y"-structure in the LEV, with the downstream branch of the vortex being advected downstream at a roughly constant velocity (i.e., $0.4u_\infty$) while its vertical coordinate relative to the wing remains within $z_{w,c} \lesssim 0.5c$.

One of the most elusive features of the dynamics of the LEV is the precise definition of its separation (and/or breakdown), and the effect that such separation might have in the aerodynamic forces over the wing [Lentink and Dickinson, 2009, Jardin and David, 2014, Birch et al., 2004, Ozen and Rockwell, 2012]. The results obtained from force decomposition algorithms in 2D configurations [Moriche et al., 2017, Martín-Alcántara et al., 2015, Chang, 1992] suggest that the effect of the vortices on the lift are important provided that the vortices are sufficiently close to the wing, roughly within one chord from the wing. From that point of view, the effect of the LEV on the forces of the present configurations should still be relevant, even while the LEV core is being advected downstream during the second half of the stroke. Hence, the methodology proposed here to quantify the LEV core position and physical properties is used next to evaluate the evolution of the circulation of the LEV vortex and its effect on the aerodynamic forces on the wing.

Figure 5.7 shows the local circulation of the LEV core for case $AR = 4$, at the spanwise positions 25% and 75%. Near the inboard wing tip, Figure 5.7a, the circulation increases smoothly during most of the downstroke, peaking at times well past the mid-downstroke (i.e., when the vertical speed of the wing and the effective angle of attack is maximum). As expected, the value of the threshold limits the time interval when the LEV core is detected, as well the value of the local circulation. On the other hand, as shown in Figure 5.7b, the local circulation at the 75% spanwise section increases steadily during the downstroke, to suddenly reach a more or less constant value after a slight overshoot. Comparison of Figures 5.7b and 5.5e shows that the time at which Γ_c reaches

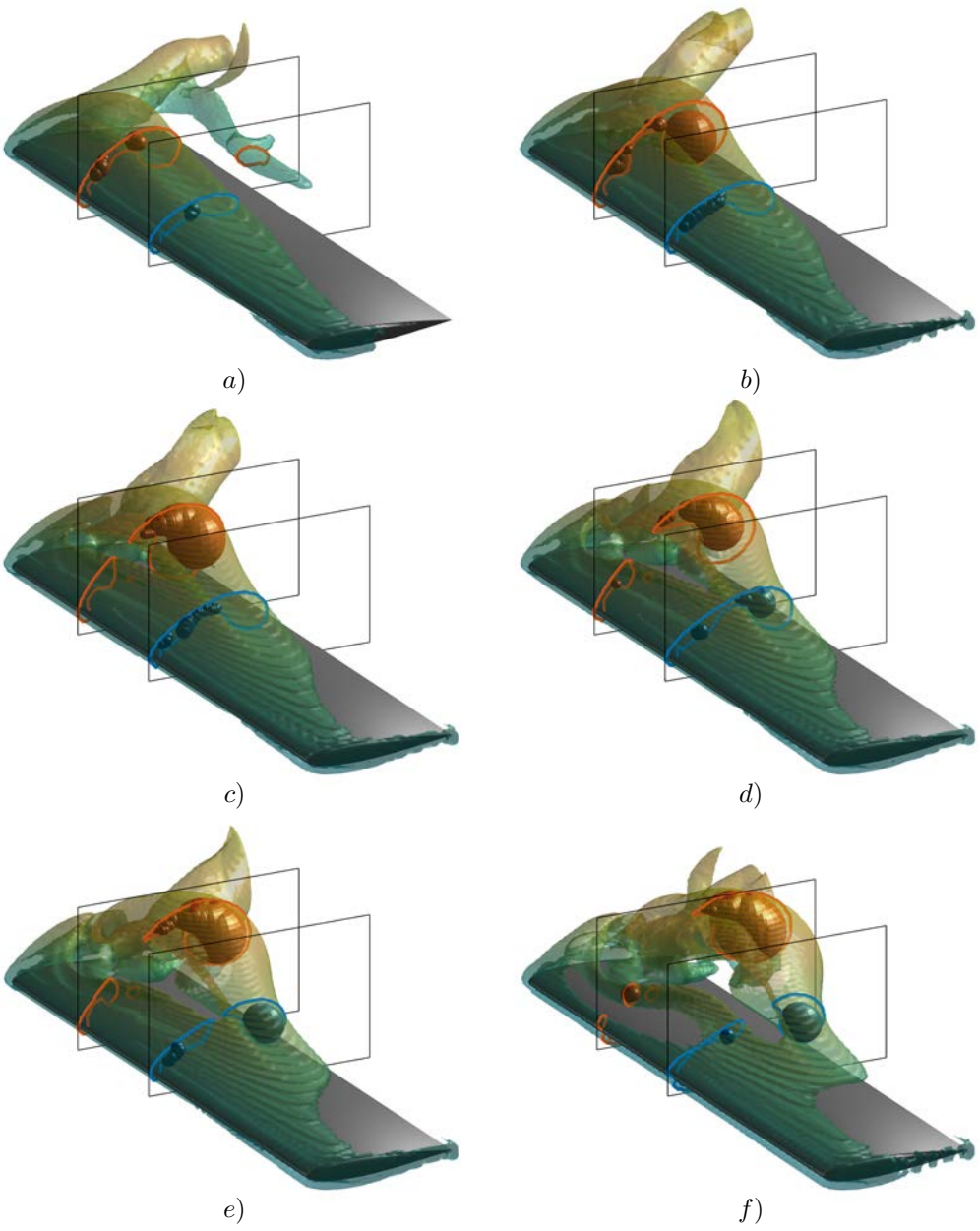

Figure 5.6: Isosurfaces of $Q' = 4.0u_\infty^2/c^2$ for the case of $AR = 4$ at (a) $t/T = 0.25$, (b) $t/T = 0.31$, (c) $t/T = 0.34$, (d) $t/T = 0.38$, (e) $t/T = 0.41$ and (f) $t/T = 0.47$. Panels also display the intersection of the planes $y_w/b = 0.5$ (———) and $y_w/b = 0.75$ (———) with the isosurfaces. The inscribed spheres associated to the skeleton points at these two spanwise location are also shown.

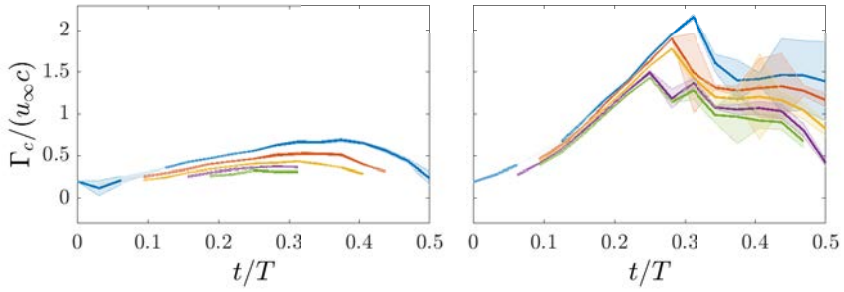

Figure 5.7: Circulation on the LEV core (Γ_c) as a function of time during the downstroke at (a) $y_w = 0.25b$ and (b) $y_w = 0.75b$. Colored lines as in Figure 5.3. The colored shaded area indicates the corresponding uncertainty.

a plateau roughly coincides with the advection of the LEV core at a constant velocity (i.e., when $x_{w,c}$ grows linearly with time in Figure 5.5e). Not surprisingly, the time when Γ_c reaches a plateau and the magnitude of the overshoot depend on Q'_{th}. Also, the uncertainty in Γ_c during the overshoot and subsequent plateau increases, probably due to the "y"-shape of the LEV and the difference in Γ_s^k for points in the upstream or downstream branches of the "y"-shaped LEV (see Figure 5.6). Although not shown, the evolution of Γ_c at the 50% spanwise position is qualitatively similar to that obtained at 75%.

Conceptually, Figures 5.5 and 5.7 suggest that the evolution of the LEV has two distinct phases. During (roughly) the first half of the downstroke, the LEV develops and grows increasing its circulation. Then, the LEV splits, and its downstream section is advected towards the wake while keeping its circulation approximately constant. The picture is very similar to that reported by Jardin and David [2014] in revolving wings using 2D visualizations, with values for the peak and plateau of the circulation of the same order of magnitude as those reported here.

Finally, Figure 5.8 evaluates the link between the local circulation of the LEV core and the local aerodynamic force, characterized here with the sectional lift coefficient

$$c_l(y_w) = \frac{l(y_w)}{1/2\rho {u_\infty}^2 c}, \tag{5.9}$$

where $l(y_w)$ is the sectional lift per unit span, i.e. the resultant of the aerodynamic forces in the vertical direction (inertial system of reference) at a spanwise section (y_w). The Figure shows c_l as a function of Γ_c during the downstroke for cases with $AR = 4$ (Figure 5.8a) and with $AR = 2$ (Figure 5.8b). Three spanwise sections are plotted with different line colors, 25% (blue), 50% (yellow) and 75% (orange). The local circulation is

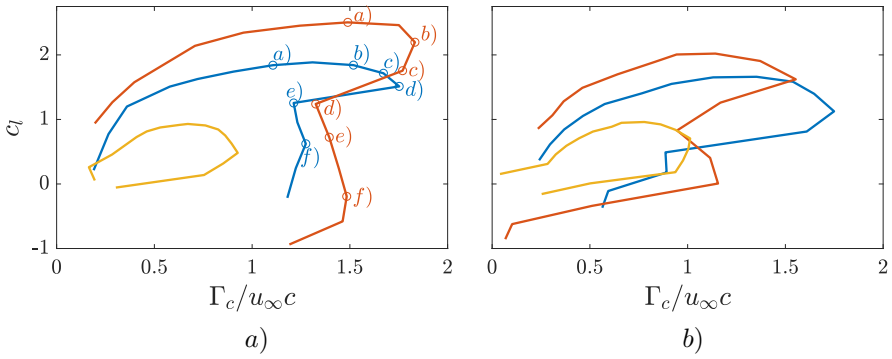

Figure 5.8: Evolution of the sectional lift coefficient, c_l, vs. the circulation of the LEV core, Γ_c, during the downstroke. Lines correspond to spanwise sections $y_w = 0.25b$ ( ), $y_w = 0.5b$ ( ) and $y_w = 0.75b$ ( ). (a) case with $AR = 4$, (b) case with $AR = 2$. The letters corresponds to the panels (i.e., times) shown in Figure 5.6.

computed for $Q'_{th} = 4{u_\infty}^2/c^2$, although similar plots are obtained for other thresholds. For the case with $AR = 4$ (Figure 5.8a), the labels on the lines for 50% and 75% of the span corresponds to the labels of Figure 5.6, so that time increases in clockwise direction for all loops in the Figure.

Focusing first in the case with $AR = 4$, Figure 5.8a shows that the maximum c_l (which occurs shortly after mid-downstroke, $t/T \gtrsim 0.25$) is obtained before the peak value of Γ_c. Indeed, between the maximum c_l and the maximum Γ_c, the local circulation still increases by about 20-30%. At the 25% spanwise section, the evolution of both c_l and Γ_c is smooth. However, and consistently with the time histories shown in Figure 5.7, at the spanwise sections 50% and 75% there is a sudden decrease in Γ_c just after its maximum. During the subsequent plateau in Γ_c, the value of the sectional lift coefficient decreases monotonically, as the LEV core is advected downstream.

Similar observations can be made for the case with the smaller aspect ratio, shown in Figure 5.8b. In this case, the reduced AR results in a less clear plateau of Γ_c, although the main characteristics observed in Figure 5.8a can still be identified: maximum c_l while Γ_c is still growing, sudden decrease of Γ_c after its maximum for 50% and 75% spanwise sections, etc.

CHAPTER
SIX

Comparison between wings with different AR

In this chapter, the cases of the database with wings of $AR = 4$ are analyzed and compared with some cases of $AR = 2$ in terms of value and surface distribution of the aerodynamic forces, and in terms of 3D flow visualizations. Moreover, a quantitative description of their LEVs is done, using the algorithm explained in the previous chapter, with the aim of understanding their effect on the aerodynamic forces. In table 6.1 all the cases analyzed in this chapter are shown along with relevant geometric and dynamic information.

In section 6.1, a brief discussion justifying the usefulness of the analyzed cases is provided. The subsequent sections analyze the effect of AR and R on the forces (sections 6.2, 6.3 and 6.4), the LEV structure (section 6.5), and the time evolution of the LEV (section 6.6).

6.1 Selected cases

In order to evaluate the effect of the AR on the transition from flapping motion to heaving, three values of R (namely, $R = 0$, $R = 2$, and $R \to \infty$) are considered for both $AR = 2$ and $AR = 4$. These six cases (shown in Table 6.1) have the same vertical displacement of the outboard wing tip, h_0. Thus, the region close to the outboard wing tip moves similarly for these cases when R is equal, independently of their AR.

According to the results obtained for $AR = 2$ in chapter 4, the effective angle of attack, α_e, is the governing parameter to the aerodynamic forces. Therefore, the comparison of regions with similar α_e in wings with different AR could isolate the effect of the later parameter in the forces. This type of comparison is enabled by cases AR4-R000* and AR4-R020* which have the same motion near the inboard wing than the flapping cases with $AR = 2$ AR2-R000 and AR2-R020. The wings of AR4-R000* and AR4-R020* move with the same amplitude of the flapping motion, Φ_0, than the cases with $AR = 2$ and equal R (see Table 6.1). Thus, all these configurations present the same values of α_e between $0 \leq y_w/c \leq 2$. Additionally, the cases AR4-R000* and AR4-R020* can be also compared with the other flapping cases with $AR = 4$ and equal R to isolate the effect of $\langle \alpha_e \rangle$ in the force coefficients and in the LEV position.

Case	AR2-R000	AR4-R000	AR4-R000*	AR2-R020	AR4-R020	AR4-R020*	AR2-Rinf	AR4-Rinf
AR	2	4	4	2	4	4	2	4
R/c	0	0	0	2	2	2	∞	∞
Ro	1.82	3.92	0.91	3.92	5.94	2.61	∞	∞
Φ_0	30.00°	14.48°	30.00°	14.48°	9.59°	14.48°	-	-
h_0/c	1.0	1.0	2.0	1.0	1.0	1.5	1.0	1.0
$\langle\alpha_e\rangle_{\max}$	26.04°	25.34°	41.40°	36.79°	33.14°	44.09°	45.00°	45.00°
$\left(\alpha_e^{tip}\right)_{\max}$	46.32°	45.31°	64.48°	45.31°	45.13°	56.59°	45.00°	45.00°
$\left(\frac{u_{\text{eff}}}{u_\infty}\right)^2_{\max}$	1.27	1.26	2.10	1.57	1.45	2.02	2.00	2.00
$\left(\frac{u_{\text{tip}}}{u_\infty}\right)^2_{\max}$	2.10	2.02	5.39	2.02	2.01	3.30	2.00	2.00
$\overline{C_x}$	0.14	0.12	-0.02	0.12	0.10	0.02	0.08	0.04
$\overline{C_z}$	0.86	1.05	2.45	1.36	1.45	2.26	1.89	2.22
$\overline{C_x^n}$	-0.06	-0.07	-0.13	-0.07	-0.08	-0.12	-0.08	-0.11
$\overline{C_x^\tau}$	0.21	0.20	0.11	0.19	0.18	0.15	0.16	0.16
$C_{x,\max}$	0.20	0.21	0.20	0.22	0.23	0.23	0.24	0.23
$C_{x,\min}$	0.09	0.05	-0.22	0.02	-0.02	-0.20	-0.07	-0.17
$C_{z,\max}$	1.55	1.73	4.64	2.36	2.39	4.11	3.39	3.99

Table 6.1: Parameters and main results of DNS cases presented in this chapter. AR is the aspect ratio of the wing, R is the radius of flapping motion, Ro is the Rossby number (see equation 3.3), Φ_0 is the amplitude of the flapping angle (in degrees), h_0 is the amplitude of the vertical displacement of the outboard wing tip, $\langle\alpha_e\rangle_{\max}$ is the maximum absolute value of the effective angle of attack averaged along the wing span (in degrees), which occur at mid-stroke, $\left(\alpha_e^{tip}\right)_{\max}$ is the maximum absolute value of the effective angle of attack at the outboard wing tip (in degrees), which also occur at mid-stroke, $\left(\frac{u_{\text{eff}}}{u_\infty}\right)^2_{\max}$ is the ratio between the squared effective velocity at the mid-span of the wing and the squared flying speed of the wings, $\left(\frac{u_{\text{tip}}}{u_\infty}\right)^2_{\max}$ is the ratio between the squared effective velocity at the outboard wing tip and the squared flying speed of the wings. Note that u_∞^2 has been used to normalized the forces. Regarding the dynamic parameters, the coefficients $\overline{C_x}$ and $\overline{C_z}$ are the streamwise force coefficient and the vertical force coefficient, respectively. $\overline{C_x^n}$ and $\overline{C_x^\tau}$ are the contribution of normal and tangential forces to C_x. All four coefficients are time-averaged during the downstroke of the wing. $C_{x,\max}$, $C_{x,\min}$ and $C_{z,\max}$ are the maximum and minimum values of the streamwise force coefficient and the maximum value of the vertical force coefficient, respectively.

Finally, it is important to note that as discussed before in section 3.3, for case AR4-R000*, the non-periodicity of the forces is related with the development of weak 3D secondary instabilities in the flow. For completeness, the envelope of the force signal obtained with all the periods have been depicted in Figures 6.1*a*, 6.2*a*, 6.3*a* and 6.3*b* through shaded contours and with error bars in Figures 6.2*b*, 6.3*c* and 6.3*d*. When the error bar is smaller than the symbol used to identify the case, it has not been included (Figure 6.1*a* and $C_{x,\max}$ in Figure 6.2*b*). Note however that the streamwise and vertical force coefficients vary from consecutive periods less than 2.5% and 0.6%, respectively. Since this difference between cycles is small, only the average value has been considered in the discussion. However, it is interesting to note that since weak 3D secondary instabilities develop in this flow, lateral instabilities might also appear. Therefore, the hypothesis of a symmetry plane between the wings should be evaluated for this particular case, which is outside of the scope of this thesis and is left for future work.

6.2 Aerodynamic forces

Figure 6.1*a* shows the time evolution of the vertical net force coefficient (C_z). Colors indicates the value of R, while the line type (dashed or solid) indicates the AR. First, it can be observed that C_z behaves similarly during the cycle for cases with $AR = 4$ (dashed lines) and cases with $AR = 2$ (solid lines). The peaks of C_z are found at the mid-downstroke and at the mid-upstroke, when the velocity of the wings is maximum. Besides, C_z generated during the downstroke is equal in magnitude to C_z generated during the upstroke, but with opposite sign. The cases with the same values of h_0 and R (see Table 6.1) present very similar curves of C_z during the cycle, even if they have different AR. However, the peaks of C_z are slightly larger for the $AR = 4$ than for the $AR = 2$ cases. This result is in agreement with classical aerodynamics theory which predicts larger lift force coefficient for wings with higher AR. Furthermore, both for $AR = 4$ and $AR = 2$, the peaks of C_z increase with R (see also Figure 4.1). Therefore, among the cases with same h_0, the maximum instantaneous lift force is obtained in the heaving wing cases (AR2-Rinf and AR4-Rinf). On the other hand, cases AR4-R000* and AR4-R020* reach peaks of C_z approximately two times larger than cases AR2-R000 and AR2-R020 respectively, and even larger than both heaving wing cases. Note that AR4-R000* (AR4-R020*) has the same Φ_0 than AR2-R000 (AR2-R020). This means that, in case AR4-R000* (AR4-R020*) the wing sections located between $0 \leq y_w/c \leq 2$ are moving equal than the wing sections of case AR2-R000 (AR2-R020) and hence, those sections have the same α_e. However, for sections placed at $y_w/c > 2$ the $AR = 4$ wing has larger values of α_e, yielding in a larger effective angle of attack averaged over the wing span, $\langle \alpha_e \rangle$.

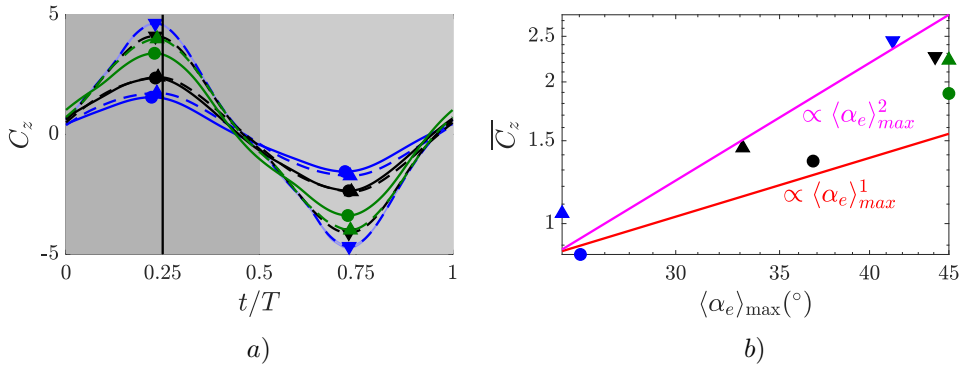

Figure 6.1: *a*) Vertical force coefficient (C_z) during one cycle and *b*) time-averaged C_z during the downstroke motion ($\overline{C_z}$) as a function of the maximum effective angle of attack averaged over the wing span ($\langle\alpha_e\rangle_{\max}$). Case AR2-R000 (●), AR2-R020 (●), AR2-Rinf (●), AR4-R000 (▲), AR4-R020 (▲), AR4-Rinf (▲), AR4-R000-* (▼) and AR4-R020-* (▼). In the left panel, simulations with wings of $AR = 2$ and $AR = 4$ are depicted with solid lines (———) and dashed lines (- - -), respectively. The location of the symbol indicates the maxima and minima. Dark (light) grey region indicates downstroke (upstroke) motion. The black vertical line indicates the mid-downstroke ($t/T = 0.25$). In the right panel, lines (———) and (———) have slopes of 1 and 2 respectively.

As discussed in chapter 4 for cases with wings of $AR = 2$, the differences in C_z seem to be related with the $\langle\alpha_e\rangle$. In order to confirm it, $\overline{C_z}$ is shown as a function of $\langle\alpha_e\rangle_{\max}$ (i.e., $\langle\alpha_e\rangle$ at the mid-upstroke) in Figure 6.1*b*. Both, in cases with $AR = 2$ and in cases with $AR = 4$, $\overline{C_z}$ increases proportional to $\langle\alpha_e\rangle^n_{\max}$, where the exponent is bounded between $1 \leq n \leq 2$. This increase is somewhat larger than the linear behavior of C_z with $\langle\alpha_e\rangle$ expected from potential theory. It is also important to note that the force coefficients have been normalized with ${u_\infty}^2$. Thus, the normalization is not taking into account that the local effective velocity (u_{eff}) of different wing sections changes from the inboard wing tip to the outboard tip (except for the heaving wing cases).

Regarding the net force in the streamwise direction during the cycle (Figure 6.2*a*), the same C_x is obtained during the downstroke and the upstroke due to the symmetry of the wing motion. Contrary to what happen with C_z (Figure 6.1*a*), the shape of C_x as a function of t/T is more affected by the AR. The minimum value of C_x occurs at the mid-downstroke for $AR = 4$ cases, slightly lagged with respect to the minimum of the $AR = 2$ cases with the same h_0 (see Table 6.1). To ease the visualization of the behavior of C_x peaks with R, Figure 6.2*b* has been included. This Figure shows that the maximum of C_x is roughly independent of R and AR (i.e., it remains nearly constant for all the cases), while the minimum value of C_x ($C_{x,\text{min}}$) decreases similarly with R

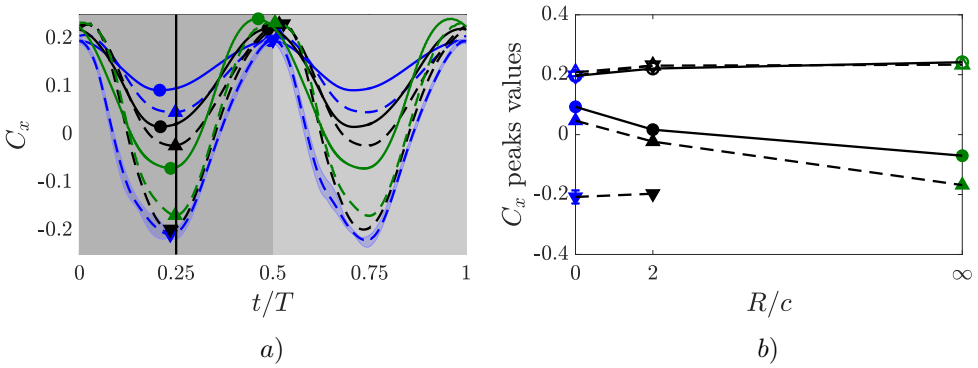

Figure 6.2: *a*) Streamwise force coefficient (C_x) during one cycle and *b*) maximum and minimum values of C_x as a function of the radius of flapping motion (R). The cases are identified as in Figure 6.1. Note that in the right panels, the maxima of C_x are represented by empty symbols, while the minima of C_x are depicted with filled symbols. In the left panel, the black vertical line indicates the mid-downstroke ($t/T = 0.25$).

for cases with $AR = 2$ and $AR = 4$ with the same h_0. Note that, $C_{x,\text{min}}$ is slightly smaller in the latter cases ($AR = 4$) than in the former ($AR = 2$). The minimum value of C_x is almost equal for cases AR4-R000* and AR4-R020*. Although, contrary to the cases with equal h_0, this minimum increases slightly with R. Additionally, $C_{x,\text{min}}$ of these two cases is considerably smaller than those found in the cases with the same R (independently of the AR), providing thrust (negative C_x) instead of drag (or almost not thrust) at the mid-strokes. These differences seem to be responsible to the net thrust force obtained in case AR4-R000* and the almost zero net drag production obtained in case AR4-R020* during the cycle.

As it has been observed in chapter 4 for wings of $AR = 2$, analyzing the contribution of normal (C_x^n) and tangential (C_x^τ) forces to C_x, allows to study the effect of R and $\langle\alpha_e\rangle$ on the generation of thrust and drag separately. Therefore, Figure 6.3*a* and 6.3*b* show the time evolution of C_x^n and C_x^τ during the cycle, respectively. The generation of thrust and drag seems to be similar for cases with $AR = 2$ and cases with $AR = 4$. Overall, C_x^n contributes to the thrust, while C_x^τ produces a drag force. Figure 6.3*a* shows that the thrust provided by C_x^n increases with AR and with R for the cases with equal h_0. Similarly, for these cases the reduction of drag observed in Figure 6.3*b* also increases with both parameters (R and AR). On the other hand, cases AR4-R000* and AR4-R020* show a thrust generation similar between them and slightly larger than the one provided by case AR4-Rinf (see Figure 6.3*a*). However, Figure 6.3*b* shows larger differences between them in the drag generation. The curves of C_x^τ of cases AR4-R020* and AR4-Rinf almost coincide, while the case AR4-R000* shows a considerably large

drag reduction respect the other two cases between the beginning of the strokes and the mid-strokes.

The dependency of $\overline{C_x^n}$ and $\overline{C_x^\tau}$ with $\langle\alpha_e\rangle$ is shown in Figures 6.3*c* and 6.3*d*, respectively. Note that, in order to plot the force coefficients in a logarithmic scale, Figure 6.3*c* shows $-\overline{C_x^n}$. According to potential theory, the growth of C_x with α_e should be quadratic, but in the cases presented in Figure 6.3*c* this growth is slower than linear. This difference might be due to the behavior of the flow near the leading edge of the wing. In potential theory the flow is completely attached to the wing, while in the cases presented here the flow is separated from the wing surface, forming an LEV. The trend of $\overline{C_x^\tau}$ with $\langle\alpha_e\rangle_{\max}$ (Figure 6.3*d*) is similar to that observed in C_x^n, but with a negative slope. Interestingly, $\overline{C_x^\tau}$ of the aperiodic case (AR4-R000*) shows a completely different behavior than the rest of the cases with $AR = 4$. Since AR4-R000* has a similar value of $\langle\alpha_e\rangle_{\max}$ than the cases AR4-R020* and AR4-Rinf, a comparable value of $\overline{C_x^\tau}$ could be expected. That discrepancy seems to be linked to the different shape of C_x^τ between the beginning of the strokes and the mid-strokes discussed in Figure 6.3*b*.

Finally, although not shown, it is important to note that the contribution of normal (C_z^n) force to C_z represents almost 90% of the total vertical force in the cases with $AR = 4$. Thus, as in cases with $AR = 2$, the pressure forces govern the lift generation in the configurations studied here.

6.3 Tangential force distribution

As in section 4.2, first, the contribution of the tangential force coefficient, c_τ (see equation 4.7), to the net streamwise force is analyzed in detail. Additionally to the streamwise contribution of c_τ to C_x^τ along x_w (defined in equation 4.6), its contribution along y_w is also considered. Thus, $c_x^\tau(y_w)$ is defined as

$$c_x^\tau(y_w) = \frac{1}{c}\int_0^c c_\tau(\xi,\eta)\,\boldsymbol{\tau}\cdot\mathbf{e}_x \mathrm{d}\xi. \tag{6.1}$$

From a physical point of view, $c_x^\tau(y_w)$ is the local contribution of a wing section located at y_w to C_x^τ, so that $\frac{1}{b}\int_0^b c_x^\tau(\eta)\,\mathrm{d}\eta = C_x^\tau$. On the other hand, recall that $c_x^\tau(x_w)$ takes into account the contribution to C_x^τ from a surface region of the wing (instead of only a wing section). This surface region is located between the leading edge and the chordwise coordinate x_w, so that $c_x^\tau(c) = C_x^\tau$.

Although not shown, $c_x^\tau(x_w)$ at the mid-downstroke presents the same behavior in cases of $AR = 4$ and equal h_0 than in cases with $AR = 2$ (see Figure 4.3*a*). Near the leading edge ($x_w/c \lesssim 0.1$) it reaches a minimum value which decreases with R, then, for $x_w/c \gtrsim 0.1$ it grows at the same rate for all the cases. As discussed for the cases with $AR = 2$, this minimum is the responsible of the differences in C_x^τ observed at $t/T = 0.25$

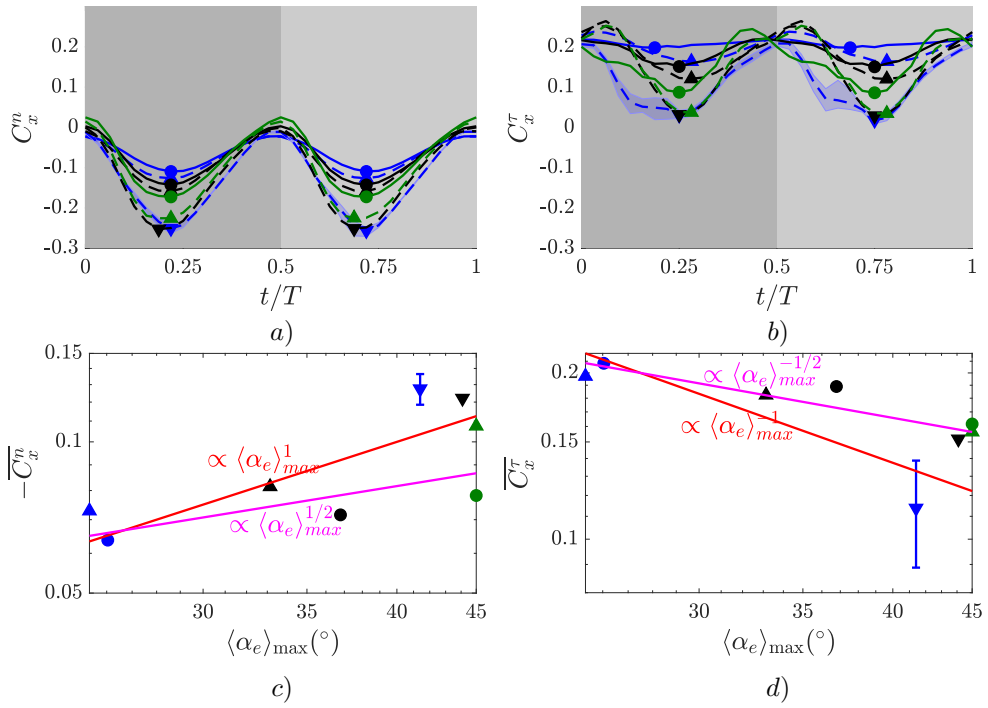

Figure 6.3: Streamwise force coefficient *a*) normal (C_x^n) and *b*) tangential (C_x^τ) components during one cycle and time-averaged *c*) C_x^n and *d*) C_x^τ during the downstroke motion as a function of $\langle\alpha_e\rangle_{\max}$. The cases are identified as in Figure 6.1. In the upper panels the peaks also coincide with the location of the symbols that identify the cases. Moreover, in those panels, dark (light) grey region indicates downstroke (upstroke) motion and the vertical scale has been chosen so that both figures can be compared with Figure 6.1*a*. In the lower panels, line (———) has a slope of 1/2 and −1/2, and the slope of line (———) is 1 and −1, respectively.

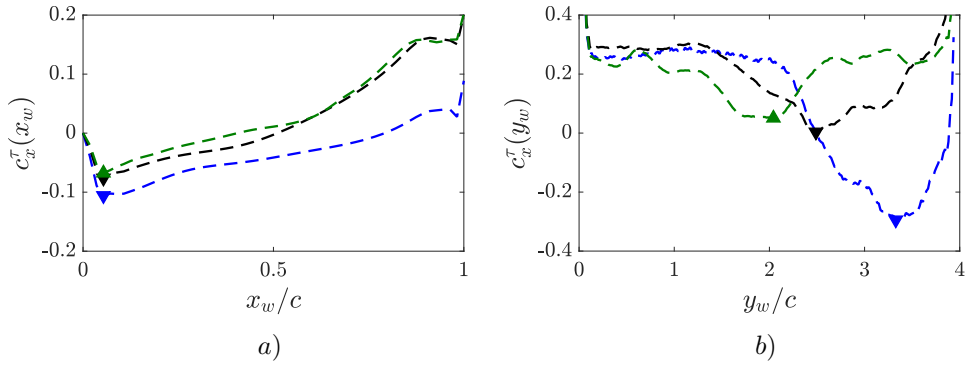

Figure 6.4: Streamwise contribution of the local tangential force coefficient (c^τ) to C_x^τ as a function of *a*) x_w and *b*) y_w at $t/T = 0.125$. AR4-R000* (▼), AR4-R020* (▼) and AR4-Rinf (▲).

for cases with different R (Figure 6.3*b*). Besides, in Figures 4.3*b* and 4.3*c* it was shown that the minimum was due to the skin friction of the boundary layer developing from the stagnation point to the leading edge of the wing. Since the stagnation point is reached at x_w closer to the leading edge for cases with smaller R, i.e., smaller $\langle\alpha_e\rangle$ (see Figures 4.3*b* and 4.3*c*), the region where the skin friction generates positive C_x^τ decreases with R, which translates into a smaller net drag reduction.

More interesting is to investigate the source of the difference found in C_x^τ between the case AR4-R000* and the cases AR4-R020* and AR4-Rinf (Figure 6.3*b*). In order to locate the wing region where the differences appear between those cases, $c_x^\tau(x_w)$ and $c_x^\tau(y_w)$ are studied (Figures 6.4*a* and Figure 6.4*b*, respectively) at $t/T = 0.125$, when the difference of C_x^τ is maximum. In figure 6.4*a* the minimum of $c_x^\tau(x_w)$ discussed above for $t/T = 0.25$ also appears for $x_w/c \lesssim 0.1$. At this time instant, despite case AR4-R000* shows a lower value of $c_x^\tau(x_w)$ at that region than the cases AR4-R020* and AR4-Rinf, it does not seem responsible for the large difference observed in C_x^τ. However, for $x_w/c \gtrsim 0.5$ the distribution of $c_x^\tau(x_w)$ of case AR4-R000* grows significantly slower than the other two cases. On the other hand, the distribution of $c_x^\tau(y_w)$ shown in Figure 6.4*b* presents larger differences between the cases than $c_x^\tau(x_w)$. The minimum of $c_x^\tau(y_w)$ is found at larger values of y_w as R decreases. For the cases AR4-R020* and AR4-Rinf this minimum is found close to the mid-span of the wing ($y_w/c \sim 2$ $y_w/c \sim 2.5$, respectively) and its value is similar and close to zero. Nonetheless, for the case AR4-R000* the minimum of $c_x^\tau(y_w)$ is found near the outboard wing tip ($y_w/c \sim 3.3$) and it is smaller than in the other cases ($c_x^\tau(y_w) \sim -0.3$).

In order to evaluate the origin of the differences of c_x^τ observed between the case AR4-

R000* and the other two cases, flow visualizations near the wing are analyzed. Figures 6.5*a* and 6.5*b* show the vortical structures developed near the wings at $t/T = 0.125$ for cases AR4-R000* and AR4-R020*, respectively. In case AR4-Rinf, the vortical structures are very similar to those observed in case AR4-R020* and therefore they are not shown for the shake of brevity. The vortical structures are identified through two isosurfaces of Q depicted in light (dark) blue, which corresponds to $Q = \sigma/8$ ($Q = \sigma/4$). Remind that Q can be interpreted as a measure of intensity of the vortex. Thus, larger values of Q corresponds to more intense vortices, as discussed in Figure 4.5. Note that σ (defined previously in 4.3) is the standard deviation obtained in a clipped volume of flow domain that includes the wings. According to the results shown in Figures 6.4*a* and 6.4*b*, greater differences should be observed close to the outboard wing and for $x_w/c \gtrsim 0.5$. This region is highlighted in Figures 6.5*a* and 6.5*b* with a red circumference and it is zoomed to facilitate its visualization in Figures 6.5*c* and 6.5*d*, respectively. In the zoomed Figures, a somewhat more developed LEV can be observed close to the outboard wing tip in the case AR4-R000* (Figure 6.5*c*) than in the case AR4-R020* (Figure 6.5*d*). Moreover, the structure of the outboard wing TiV is smooth in the case AR4-R020* and at a region close to the leading edge of the wing in the case AR4-R000*. However, the TiV of the later case breaks down after the mid-chord, at the region where the large difference on $c_x^\tau(x_w)$ between both cases was found. This seems to suggest that the smooth TiV found in case AR4-R020* is generating a larger drag force due to the tangential force than the broken down TiV of case AR4-R000*.

6.4 Normal force distribution

In section 6.2, the contribution of the normal force to the streamwise (C_x^n) and vertical (C_z^n) net forces have been discussed. While C_x^n represented approximately half of the total contribution to C_x, C_z^n was dominant in the generation of lift. Hence, this section focuses in the characterization of the effect of the AR and the effective angle of attack (α_e) on C_z for the cases with different R studied.

The distribution of the normal force coefficient, c_n (see equation 4.8), is analyzed in the upper surface of the wing at the mid-downstroke ($t/T = 0.25$), when C_z is maximum. At mid-downstroke the lift is enhanced by an attached LEV that is formed precisely in the upper surface of the wing. The comparison of the distribution of c_n for cases with different AR is performed so that the wing span sections with similar/equal α_e of $AR = 2$ cases overlap with those of $AR = 4$ cases (see sketch in Figure 6.6). Thus, in the right panels of Figures 6.8 and 6.9 the distribution of c_n on the upper surface of cases with $AR = 4$ is shown with colored contours and the contours of the $AR = 2$ cases are included with black lines. Note that to ease the comparison, the black contours of the $AR = 2$ cases are split in two halves following the procedure explained

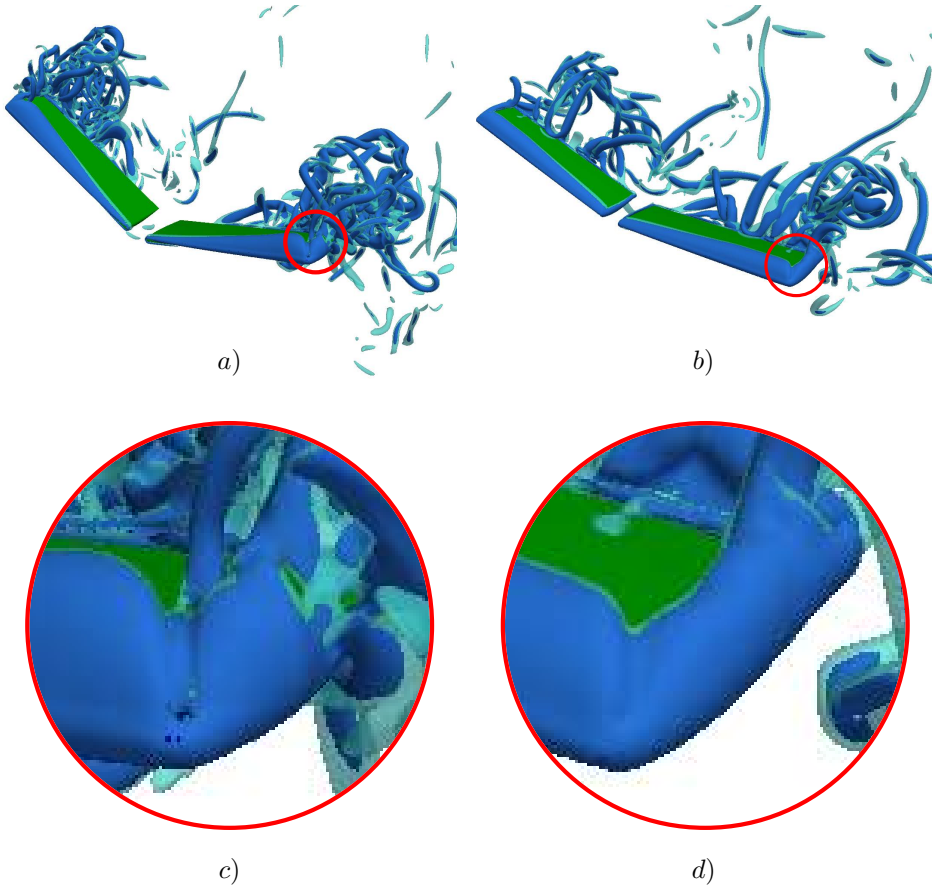

Figure 6.5: Flow visualization at $t/T = 0.125$ of cases *a*) AR2-R000* and *b*) AR4-R020*. Light blue surfaces correspond to $Q = \sigma/8$ and dark blue surface corresponds to $Q = \sigma/4$ for each case. Wings are displayed in green in these figures. The red circumferences highlights the region of interest (i.e., a region near the outboard wing tip). This region is zoomed in *c*) and *d*) for the cases AR2-R000* and *b*) AR4-R020*, respectively.

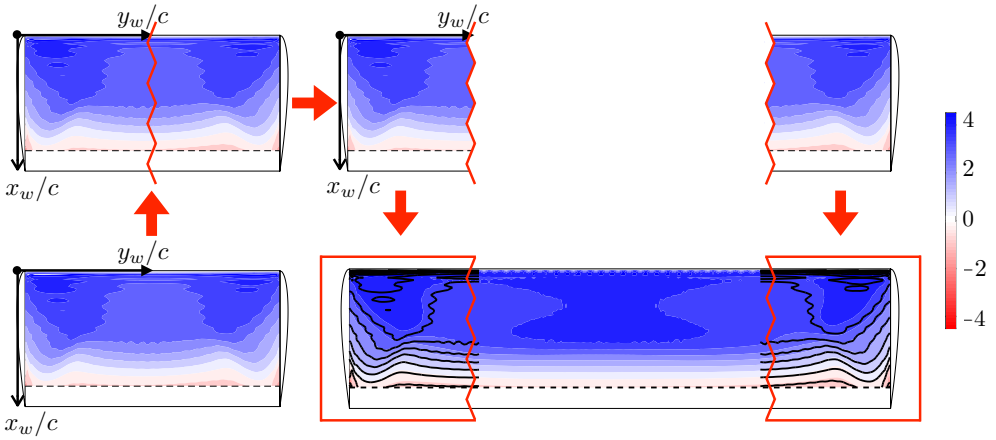

Figure 6.6: Sketch of the procedure follows to show the distribution of the local normal force coefficient (c_n) on the upper surface of the wing for cases with different AR. To illustrate the procedure, the distribution of c_n on the upper surface of cases AR2-Rinf and AR4-Rinf at the mid-downstroke have been used. In the lower left panel, the c_n distribution of the case AR2-Rinf is shown through colored contours. After, the upper left panel shows how the $AR = 2$ upper wing surface with the colored contours of the case AR2-Rinf are split in two halves. Then, in the upper right panel both halves are separated until the inboard and outboard wing tips of the case AR2-Rinf coincide with those of the case AR4-Rinf. Finally, the lower right panel shows the c_n distribution on the upper surface of the case AR4-Rinf with colored contours along with the split and separated contours of the case AR2-Rinf included with black lines. The black dashed line at $x_w/c = 0.85$ limits the region where the IBM is not providing an accurate description of c_n, as discussed in section 3.3.

in Figure 6.6. Note also that the overlapping regions are similarly affected by the TiVs. For completeness, the left panels of Figures 6.8 and 6.9 show the distribution of c_n on the upper surface of $AR = 2$ cases with colored contours.

Since α_e changes along the wing span for the flapping cases, it is analyzed in Figure 6.7 as a function of y_w at the mid-downstroke before comparing the c_n distributions. This Figure shows that the effective angle of attack remains constant along the wing span for both heaving cases (green lines), while it increases with y_w for all the flapping cases (blue and black lines). The growth of α_e with y_w in the latter cases is more pronounced in cases with $AR = 2$ than in cases with $AR = 4$. Thus, despite all the cases with equal h_0 have a similar value of α_e at the outboard wing tip ($y_w/c = 4$ in Figure 6.7), it rapidly differs between cases for smaller y_w. These differences become larger more quickly for cases with smaller R, i.e., in that region the values of α_e differs more between cases AR2-R000 and AR4-R000 than between cases AR2-R020 and AR4-R020. Interestingly, cases AR2-R020 and AR4-R000 have the same α_e along $3 \leq y_w/c \leq 4$. Note however

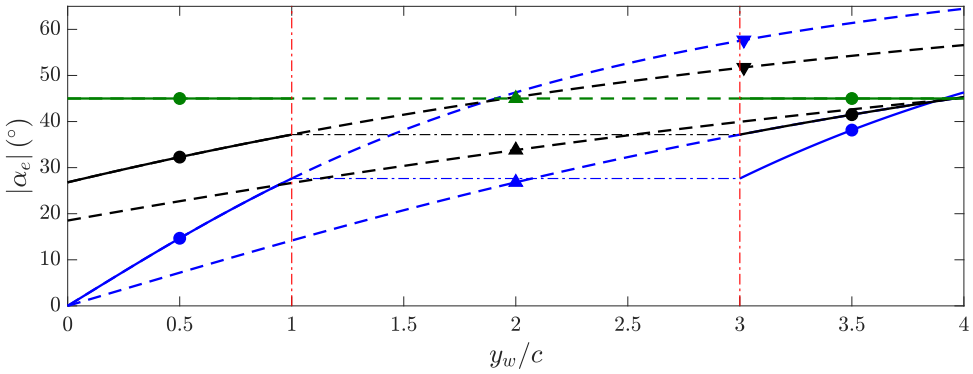

Figure 6.7: Local effective angle of attack (α_e) as a function of the wing span direction (y_w). Cases with $AR = 2$ and $AR = 4$ are depicted with solid lines (———) and dashed lines (- - -), respectively. Case AR2-R000 (●), AR2-R020 (●), AR2-Rinf (●), AR4-R000 (▲), AR4-R020 (▲), AR4-Rinf (▲), AR4-R000-* (▼) and AR4-R020* (▼). Note that, the wing span of the cases with $AR = 2$ has been split and separated following the procedure explained in Figure 6.6. To ease the identification of the split $AR = 2$ wings of the flapping cases, they are joined with horizontal dashed-dotted lines, (·-·-·) for case AR2-R000 and (- - ·-· - -) for case AR2-R020.

that for the case AR2-R020 this region is in fact located at $1 \leq y_w/c \leq 2$ in the $AR = 2$ wing. In the region near the inboard wing tip, α_e is completely different in the flapping cases with the same h_0 and equal R. Conversely, in cases AR2-R000 (AR2-R020) and AR4-R000* (AR4-R020*) α_e is equal at that region, since the same motion was imposed between $0 \leq y_w/c \leq 2$ in both cases.

Next, the distribution of c_n is compared at the mid-downstroke ($t/T = 0.25$) for the cases with $AR = 2$ and $AR = 4$ that have the same h_0 (Figure 6.8). Recall that c_n is analogous to the (minus) pressure coefficient and therefore positive c_n corresponds to suction, which in the upper surface of the wing contributes to the lift production. In all the cases with the same h_0 (see Table 6.1), the suction is dominant in the upper wing surface, i.e., they are generating lift force. This positive c_n is specially larger close to the leading edge of the wing. Near the region where the IBM can not provide accurate surface distributions of the force ($x_w/c \gtrsim 0.85$, see section 3.3), c_n changes of sign independently of AR or R.

For both cases with $R \to \infty$ (Figures 6.8*a* and 6.8*b*), the distribution of c_n is almost symmetric. Moreover, despite the α_e is the same along the wing span, the suction ($c_n > 0$) peaks near the tips. In the case AR4-Rinf, there is also a region with the same suction magnitude at the mid-span of the wing that is probably due to the effect of the LEV. Interestingly, this region is not present in the case AR2-Rinf. This suggests that for wings of $AR = 2$, the LEVs are not completely developed due to the interactions

with the TiVs.

For cases with $R = 2$ (Figures 6.8*c* and 6.8*d*) and with $R = 0$ (Figures 6.8*e* and 6.8*f*), c_n peaks near the outboard wing tip ($y_w/c = b$). At that location, the wing sections have similar α_e than the cases with $R \to \infty$. Note however that the magnitude of the suction in that region is somehow smaller as R decreases. In these four cases, c_n decreases progressively from the outboard wing tip to the inboard wing tip ($y_w = 0$) as it happened to α_e in Figure 6.7. In addition, the decay of c_n seems slightly smoother in the cases with $AR = 4$ (AR4-R020 and AR4-R000) than in the cases with $AR = 2$ (AR2-R020 and AR2-R000), coinciding with the decrease rate of α_e observed also in Figure 6.7. As expected, near the inboard wing tip where smaller α_e are found for cases with smaller R, the c_n distribution also decreases with R.

Finally, the comparison of the overlapped contours depicted in Figures 6.8*b*, 6.8*d* and 6.8*f* shows that near the outboard wing tip the distribution of c_n of cases with different AR and the same R is similar. Although, it is more alike as R increases because α_e is comparable along a larger wing span region (see Figure 6.7). Near the inboard wing tip only the cases with $R \to \infty$ are similar, since they are almost symmetric respect the mid-span. On the other hand, the cases with $R = 0$ and $R = 2$ shows a completely different distribution of c_n in that region between cases with $AR = 2$ and $AR = 4$. This is possibly due to the large differences of α_e observed between those cases near the wing tip ($0 \leq y_w/c \leq 1$).

In the previous Figure, a correlation between α_e and the distribution of c_n along y_w has been discussed. Therefore, in order to confirm it, Figure 6.9 shows the c_n distribution on the upper surface at $t/T = 0.25$ for flapping cases with different AR that have the same α_e in regions near the inboard or outboard wing tip. According to the observations made in Figure 6.7, cases AR2-R000 and AR4-R000* (Figures 6.9*a* and 6.9*b*), and cases AR2-R020 and AR4-R020* (Figures 6.9*c* and 6.9*d*) have equal α_e near the inboard wing tip (highlighted with a red rectangle). Predictably, the distribution of c_n at that region is very similar for cases that have the same R and move identically from $0 \leq y_w/c \leq 2$. However, it is still possible to appreciate small differences between them and these differences are slightly larger between cases with smaller R. In Figure 6.7 the cases AR2-R020 and AR4-R000 (Figures 6.9*e* and 6.9*f*) shown equal values of α_e near the outboard wing tip (identified with a red rectangle). Surprisingly, despite these two cases do not have the same R, they present an agreement between the c_n contours at the outboard tip which is even better than the one observed in the previous cases at the inboard tip. This confirms the large influence of α_e on the distribution of c_n in the upper surface of the wing.

The c_n distributions in the upper surface do not depend exclusively of the α_e and the AR. For instance, in the heaving wing cases, the c_n distribution changes along the wing span, even though the value of α_e is the same in all wing sections. As discussed

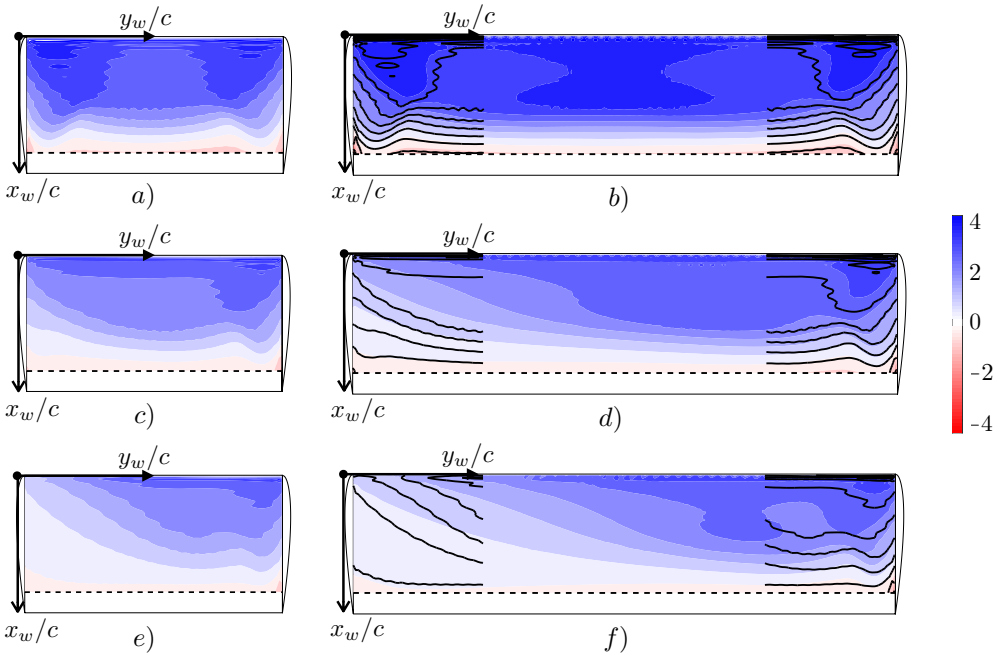

Figure 6.8: *a*),*c*),*e*) Distribution of the local normal force coefficient (c_n) on the upper surface of the wing at $t/T = 0.25$ for cases AR2-Rinf, AR2-R020 and AR2-R000, respectively. *b*),*d*),*f*) Distribution of c_n on the upper surface of the wing at $t/T = 0.25$ for cases AR4-Rinf, AR4-R020 and AR4-R000, respectively. The black dashed line at $x_w/c = 0.85$ limits the region where the IBM is not providing an accurate description of c_n, as discussed in section 3.3. Note that in the right panels, the contours of distribution of c_n of the cases with $AR = 2$ are included with black lines (following the procedure explained in the sketch of Figure 6.6).

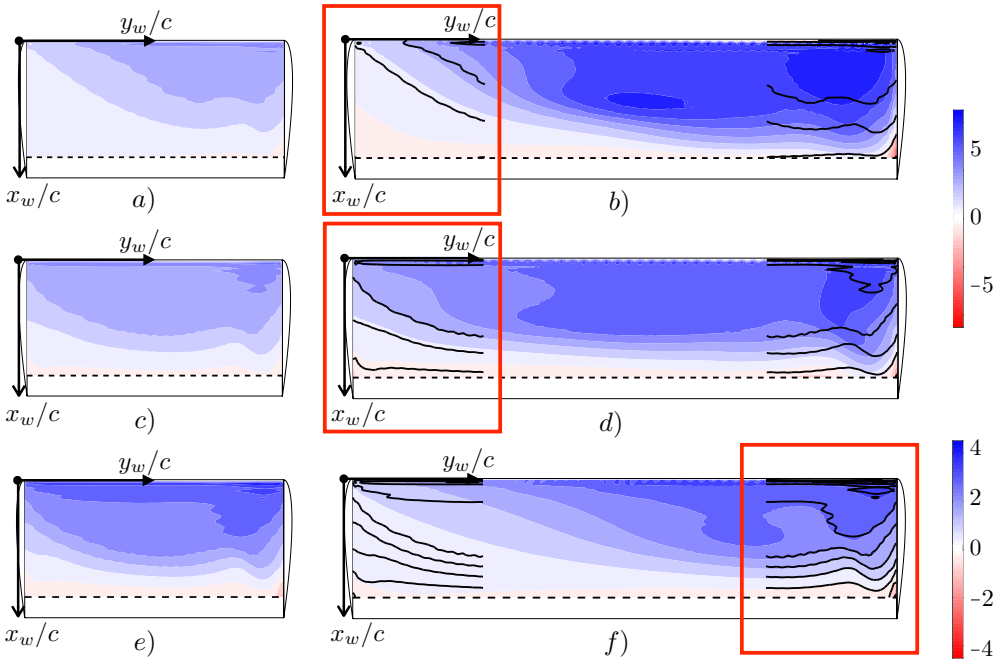

Figure 6.9: *a*),*c*),*e*) Distribution of the local normal force coefficient (c_n) on the upper surface of the wing at $t/T = 0.25$ for cases AR2-R000, AR2-R020 and AR2-R020, respectively. *b*),*d*),*f*) Distribution of c_n on the upper surface of the wing at $t/T = 0.25$ for cases AR4-R000*, AR4-R020* and AR4-R000, respectively. The black dashed line at $x_w/c = 0.85$ limits the region where the IBM is not providing an accurate description of c_n, as discussed in section 3.3. Note that although *c*) and *e*) panels show the c_n distribution of the same case, the color scale selected for each panel is different. Note also that in the right panels, the contours of distribution of c_n of the cases with $AR = 2$ are included with black lines (following the procedure explained in the sketch of Figure 6.6). The regions where the cases with different AR have the same α_e are approximately highlighted with red rectangles.

above, those changes seem to be associated to the effect of the vortical structures located near the wing. These hypothesis are supported by the flow visualizations at the mid-downstroke shown in Figure 6.10 and by animations (not shown). The vortical structures are identified as in Figure 6.5, i.e., with light blue and dark blue structures which corresponds to weak and intense vortices, respectively.

For the cases with $AR = 4$ and the same h_0 than the cases of $AR = 2$ the evolution of the flow structures near the wing during the cycle is similar independently of the AR. Therefore in the $AR = 4$ cases, a strong LEV also starts to develop in the upper surface of the wing from the beginning of the downstroke ($t/T = 0$), TiVs with similar shape and intensity are formed in the outboard wing tips at the mid-downstroke ($t/T = 0.25$), the intensity of the inboard TiV observed at this time instant decreases with R and close to the stroke reversal ($t/T = 0.5$) the LEV and the TiVs are shed into the wake generating ring-like structures. Those ring-like vortices are also very similar between wings with $AR = 2$ and $AR = 4$, being quite symmetric for cases with $R/c \gtrsim 2$ (Figures 6.10*a*-6.10*d*). Although, they are larger in the span direction (y_w) for the $AR = 4$ cases (Figures 6.10*b*, 6.10*d* and 6.10*f*), since the LEV is formed along the entire wing span. On the other hand, the behavior of the flow structures for the cases AR4-R000* and AR4-R020* (Figures 6.10*g* and 6.10*h*, respectively) differs from the other cases. At a time instant between $t/T = 0$ and $t/T = 0.25$ the TiVs and the LEV start to break down. Therefore, the structures shed into the wake close to $t/T = 0.5$ are different from those observed in the cases with equal h_0. Moreover, the separation of the LEV seems to occur slightly before in these two cases (AR4-R000* and AR4-R020*) than in cases AR4-R000 and AR4-R020, which have the same AR and R.

Figure 6.10 also allows us to compare the LEV of the different cases at the mid-downstroke. In the flapping wing cases (cases with $R = 0$ and $R = 2$), the LEV intensity (i.e. volume of the dark blue Q isosurface) decays from the outboard wing tip to the inboard wing tip forming a conical-shaped LEV. The taper of this LEV from outboard to inboard tip is sharper as R decreases. This LEV feature correlates with the evolution of the c_n distributions of those cases along the wing span, which was also linked with α_e. For instance, for the cases with the same h_0, the LEV structure is similar at the outboard tip (where α_e is almost the same), while at the inboard tip it is weaker for cases with smaller R (i.e., cases with smaller α_e). Moreover, the details of the LEV provide additional information to understand the differences and similarities observed on the distributions of c_n in Figures 6.8 and 6.9. At the mid-downstroke, the case AR4-Rinf presented a large value of suction at the mid-span, which did not appear in case AR2-Rinf (6.9*b*). However, the shape of the LEV at that region is really similar. The only difference between the LEV of both cases at the mid-span is that in AR4-Rinf (Figure 6.10*b*) the TiVs are far away, while in the case AR2-Rinf (Figure 6.10*a*) they are flanking the mid-span section of the LEV from a distance closer than one chord. For

cases with the same α_e near the inboard or outboard wing tip, which presented analogous c_n distributions in those region (see Figure 6.9), the vortex structures are almost equal. This can be observed in the region close to the inboard wing tip of cases AR2-R000 and AR4-R000* (AR2-R020 and AR4-R020*), which have been highlighted with blue (black) circumferences in Figures 6.10a and 6.10g (6.10c and 6.10h), respectively. Close to the region near the outboard tip, the cases AR2-R020 and AR4-R000 also present very similar vortex structures (see red circumferences in Figures 6.10c and 6.10f).

6.5 LEV characterization at mid-downstroke

The importance of the effect of the LEV on the aerodynamic forces has been observed in the previous two sections. Thus, it seems necessary to go one step further and analyze quantitatively the specific features of the LEV to correlate them with the values and surface distributions of the forces discussed above. This characterization is performed using the algorithm described in chapter 5. Since, in that chapter, it was proven that the impact of the Q' criterion threshold was minor, all the results presented in this chapter use a $Q'_{th} = 4{u_\infty}^2/c^2$.

First, the position of the LEV core is analyzed at the mid-downstroke for the cases with equal h_0 in Figure 6.11. This Figure shows that both heaving wing cases present an almost symmetric configuration respect to $y_w = b/2$ as observed qualitatively in Figures 6.10a and 6.10b. Furthermore, the similarities observed in the LEV of all cases near the outboard wing tip are confirmed with the vertical ($z_{w,c}$) and the streamwise ($x_{w,c}$) position of the LEV core. At the last half chord of the wing span, i.e., $1.5 \lesssim y_w/c \lesssim 2$ in the cases with $AR = 2$ and $3.5 \lesssim y_w/c \lesssim 4$ in the $AR = 4$ cases, the lines of $z_{w,c}$ of the different cases almost coincide. Note that although in $x_{w,c}$ the differences are slightly larger, the uncertainty of the position (depicted with shaded contours) is also somewhat larger. Last, the decay of LEV intensity from the outboard wing tip to the inboard wing tip discussed for the flapping wing cases in Figure 6.10, seems to be related to a decrease of $z_{w,c}$ (see Figures 6.11a and 6.11b) and a closer position of the LEV core to the leading edge of the wing (see Figures 6.11c and 6.11d). This may be suggesting that at the spanwise positions where the LEV core is close to the leading edge of the wing and to the wing surface (near the inboard tip), the LEV is less developed and less intense. On the other hand, when it is farther away from the leading edge and is more separated from the wing (close to the outboard tip), the LEV is already developed and has more intensity. Besides, a more intense LEV would be providing large lift force in that particular region, as shown near the outboard wing tip in the distributions of c_n (Figure 6.8).

Regarding the position of the LEV core at $t/T = 0.25$ for the cases with equal α_e at the inboard or outboard wing tip regions (Figure 6.12), only those particular regions

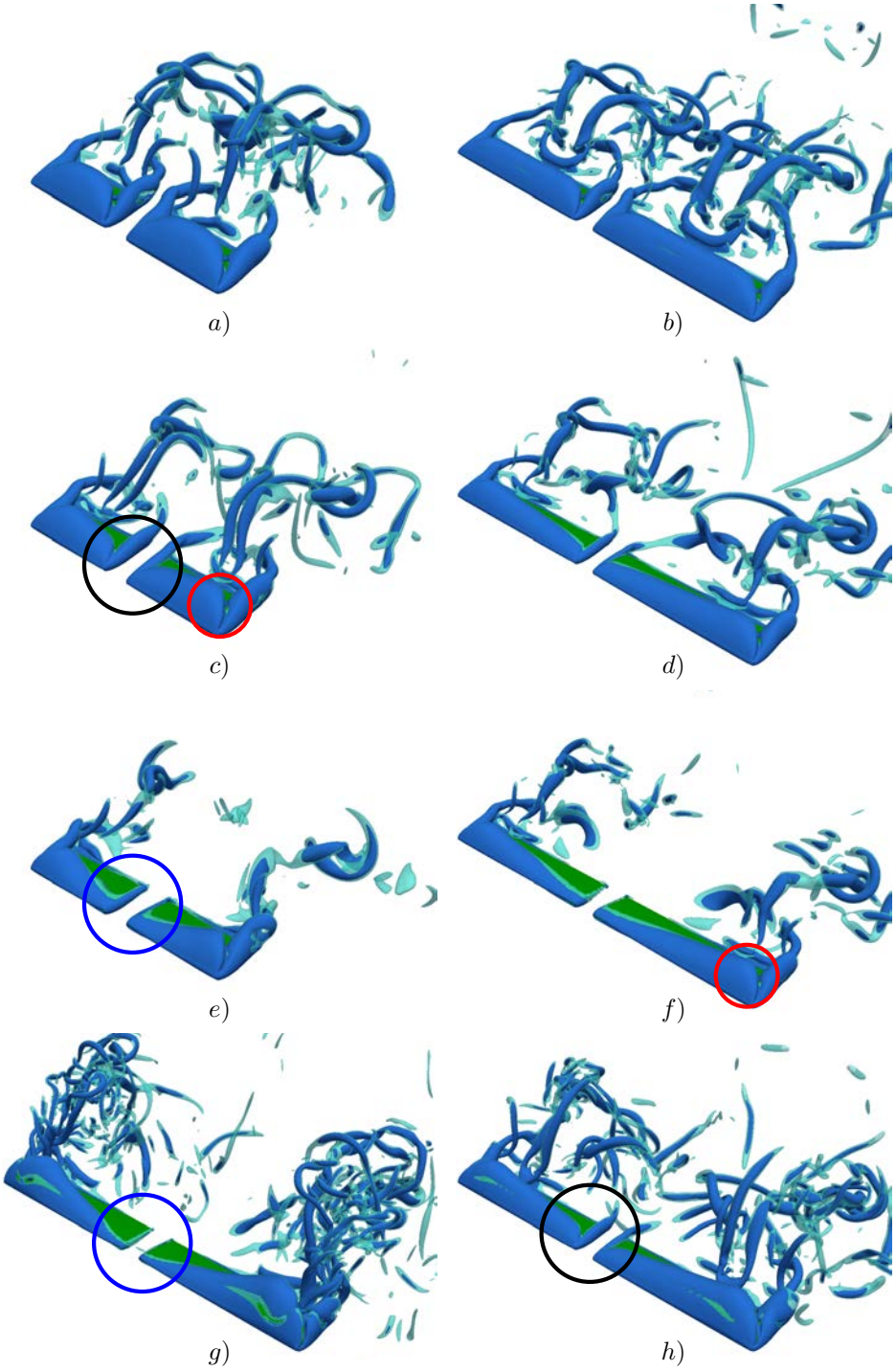

Figure 6.10: Flow visualization at the mid-downstroke ($t/T = 0.25$) of cases *a*) AR2-Rinf, *b*) AR4-Rinf, *c*) AR2-R020, *d*) AR4-R020, *e*) AR2-R000, *f*) AR4-R000, *g*) AR4-R000* and *h*) AR4-R020*. Light blue surfaces correspond to $Q = \sigma/8$ and dark blue surface corresponds to $Q = \sigma/4$ for each case. Wings are displayed in green in the panels. The red circumferences highlight regions of interest discussed in the text. In case AR4-Rinf (*b*) the region of interest is zoomed in *i*).

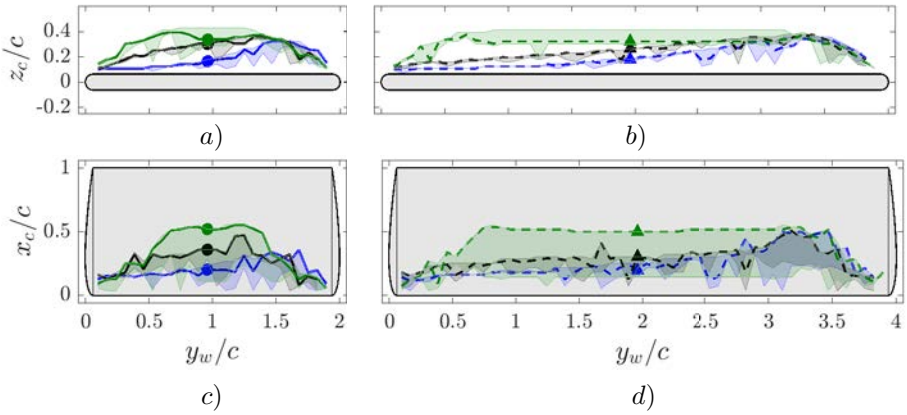

Figure 6.11: *a*), *b*) Vertical (z_c) and *c*), *d*) streamwise coordinate of the LEV core (x_c) along the wing span at mid-downstroke ($t/T = 0.250$). Panels *a*) and *c*) correspond to $AR = 2$ cases and panels *b*) and *d*) to the cases with $AR = 4$. The cases are identified as in Figure 6.7. $Q'_{th}c^2/u_\infty^2 = 4$ has been selected to find the LEV core with the algorithm presented in chapter 5. The colored shaded area indicates the uncertainty in the position of the LEV core and the wing is displayed in grey.

are likely to be compared. Predictably, the LEV core is located at completely different positions in all the cases presented at the regions where the motion of the wing and the values of α_e are different (i.e., at the outboard wing tip for cases AR2-R000 and AR4-R000* and at the inboard wing tip for cases AR2-R020 and AR4-R000). However, Figures 6.12*a* and 6.12*b* show that at $t/T = 0.25$ the LEV core of cases AR2-R000 and AR4-R000* has a very similar streamwise and vertical position near the inboard wing tip ($0 < y_w/c \lesssim 1$). Hence, it seems that the LEV behaves equal in regions where the motion of the wing is the same, independently of the AR. Although not shown for brevity, cases AR2-R020 and AR4-R020*, which also have the same motion near the inboard tip, present analogous results than the previous two cases. The streamwise and vertical LEV core positions of the cases AR2-R020 and AR4-R000 are shown in Figures 6.12*c* and 6.12*d*, respectively. Remind, that at $t/T = 0.25$ these two cases have the same α_e near the outboard wing tip (located between $3 \lesssim y_w/c \lesssim 4$ in these Figures). In these cases the position of the LEVs cores is also very alike. The results shown in Figure 6.12 are consistent with the c_n distribution shown in Figure 6.9, highlighting the relevance of the LEV in the aerodynamic force distribution.

Finally, in order to isolate the effect of the α_e on the LEV core position, two cases with the same R and AR (AR4-R000 and AR4-R000*) are compared at the mid-downstroke ($t/T = 0.25$). At that time instant, the streamwise ($x_{w,c}$) and vertical ($z_{w,c}$) positions

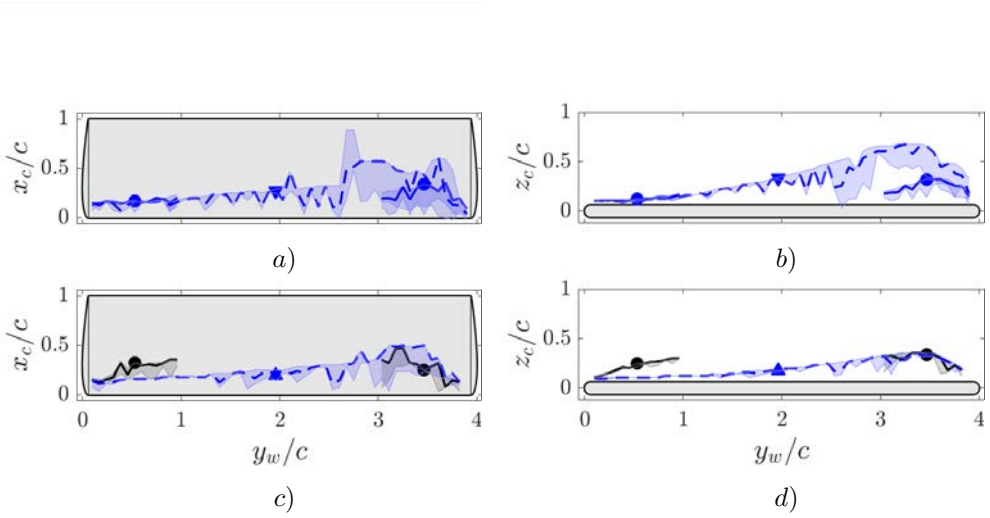

Figure 6.12: *a*), *c*) Streamwise (x_c) and *b*), *d*) vertical coordinate of the LEV core (z_c) along the wing span at mid-downstroke ($t/T = 0.250$). Panels *a*) and *b*) show cases AR2-R000 (●) and AR4-R000* (▼) and panels *c*) and *d*) present cases AR2-R020 (●) and AR4-R000 (▲). Note that cases with $AR = 4$ are depicted with dashed lines - - - , while $AR = 2$ cases are shown with solid lines ——— and are split and separated along the spanwise direction following the procedure explained in Figure 6.7. $Q'_{th}c^2/u_\infty^2 = 4$ has been selected to find the LEV core with the algorithm presented in chapter 5. The colored shaded area indicates the uncertainty in the position of the LEV core and the wing is displayed in grey.

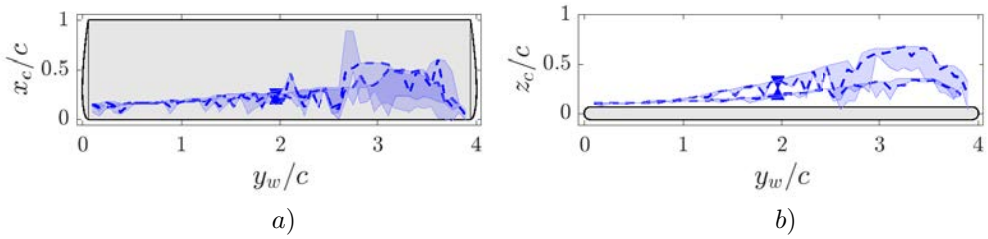

Figure 6.13: *a*) Streamwise (x_c) and *b*) vertical coordinate of the LEV core (z_c) along the wing span at mid-downstroke ($t/T = 0.250$). Case AR4-R000 is depicted by (▲) and case AR4-R000* is identified by (▼). $Q'_{th}c^2/u_\infty^2 = 4$ has been selected to find the LEV core with the algorithm presented in chapter 5. The colored shaded area indicates the uncertainty in the position of the LEV core and the wing is displayed in grey.

of the LEV core of these cases are shown in Figures 6.13*a* and 6.13*b*, respectively. Even though the α_e values of AR4-R000* are larger than those presented by case AR4-R000, near the inboard wing tip ($0 \lesssim y_w/c \lesssim 1$) both cases have similar values of $x_{w,c}$ and $z_{w,c}$. From $y_w/c \sim 1$ to the end of the wing span ($y_w/c = AR = 4$), the vertical position of the LEV core increases faster for case AR4-R000* than for case AR4-R000. Note that, the difference of α_e between both cases in that spanwise region is larger than 13.5° and peaks at $y_w/c = 2.75$ with a $\alpha_e \sim 20.5°$ (see Figure 6.7). However, the maximum difference in $z_{w,c}$ is found approximately at $y_w/c = 3.25$, where the maximum values of $z_{w,c}$ are reached, being $z_{w,c,\max} \sim 0.39c$ for case AR4-R000 and almost double for case AR4-R000*. Surprisingly, despite the differences observed in the vertical position of the the LEV core, the streamwise position is very similar along the whole wing span in both cases, suggesting that α_e does not affect $x_{w,c}$ as much as $z_{w,c}$. Similar results were obtain in the analysis of cases AR4-R020 and AR4-R020*, but they were not include here for brevity.

Besides the position, the intensity of the LEV seems to be the more important factor to measure its influence on the aerodynamic forces. This LEV intensity can be quantify through the circulation on its core (Γ_c). In Figure 6.14, The LEV circulation of all the cases detailed in Table 6.1 is shown as a function of y_w at the mid-downstroke. The curves of Γ_c between $0.5 \lesssim y_w/c \lesssim 3.5$ are similar to those observed in Figure 6.7 for the effective angle of attack (α_e). All the flapping cases increase their value of Γ_c with y_w, the cases with $AR = 2$ show a faster growth of Γ_c than the cases with $AR = 4$ with the same h_0, and the cases with the same motion at the inboard or outboard wing tip present analogous values of Γ_c in those regions. Moreover, both heaving wing cases

show an almost constant value of Γ_c slightly larger than 2, where α_e is equal to 45°. In the regions near the inboard ($0 \leq y_w/c \lesssim 0.5$) and the outboard ($3.5 \lesssim y_w/c \leq 4$) wing tips, the circulation of most of the cases behaves differently than α_e. This is consistent, since those regions are affected by the TiVs. Even so, in those regions the algorithm might be associating the Γ_c of the LEV and the TiVs, as the larger uncertainty region seems to be indicating. Note also that for the cases with larger α_e (AR4-R000* and AR4-R020*) the circulation reach a maximum between $y_w/c = 2.5$ and $y_w/c = 3$ and then decreases. These behavior along with the larger regions of uncertainties seem to be linked to the presence of the split "y"-shaped LEV observed in Figures 6.10*g* and 6.10*h*, and discussed in chapter 5.

The effect of Γ_c on the distribution of c_n in the upper surface can be easily extrapolated from the previous discussions. In the wing sections where the LEV is more intense (i.e., has a larger circulation) the c_n distribution presents larger positive values and therefore is producing more lift force. Furthermore, in cases with span sections that have almost equal Γ_c and α_e the c_n distributions are similar in shape and magnitude. This can be observed near the inboard wing tip of cases AR2-R000 and AR4-R000* or AR2-R020 and AR4-R020* and near the outboard wing tip of cases AR2-R020 and AR4-R000. Note also that the cases AR4-R000*, AR4-R020* and AR4-Rinf have the same α_e and Γ_c at $y_w/c \sim 2$ (Figures 6.7 and 6.14*a*). However, Figure 6.14*b* shows that at mid-span only the force coefficient of cases AR4-R020* and AR4-Rinf are similar. Case AR4-R000* has a force coefficient in this location that is significantly larger.

6.6 Time evolution of the LEV

Since the flow over flapping wings is unsteady, it is also necessary to characterize the evolution in time of the LEV. One of the most critical time instants during the downstroke motion is when the LEV detaches from the wing and is shed into the wake. This phenomenon is associated with a substantial decrease of lift force Martín-Alcántara et al. [2015], Moriche et al. [2017] therefore the ability to identify when and how this is happening could increase our understanding on flapping flight. To that end, the analysis presented in chapter 5 for cases AR2-R000 and AR4-R000 is extended here to the cases summarized in Table 6.1. Since the objective is to evaluate the effect of R on the LEV evolution, mostly cases with $AR = 4$ are analyzed. Unless explicitly stated, the results for the $AR = 2$ cases are qualitatively the same.

The time evolution of the LEV is first characterized with the chordwise ($x_{w,c}$) and vertical ($z_{w,c}$) position of its core for the cases with $AR = 4$ and equal h_0 at three positions corresponding to 25%, 50% and 75% of the wing span (Figure 6.15). In the region closer to the inboard wing tip (i.e., 25% of the span, see Figures 6.15*a* and 6.15*b*) the position of the LEV of each case evolves differently during the downstroke. In the

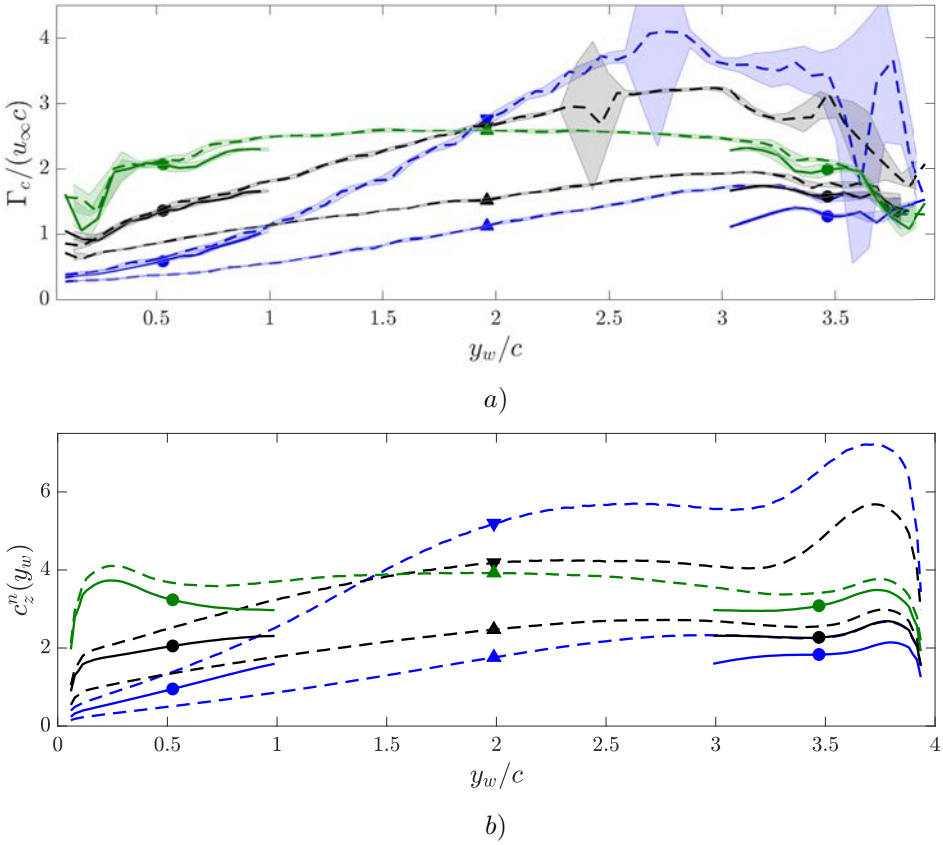

Figure 6.14: *a*) Circulation on the LEV core (Γ_c) and *b*) vertical contribution of the local normal force coefficient (c^n) as a function of the wing span direction (y_w). The cases are identified as in Figure 6.7. Note that, the wing span of the cases with $AR = 2$ has been split and separated following the procedure explained in Figure 6.6.

case with smaller R (AR4-R000) the LEV core remains close to leading edge and to the surface of the wing and present a small uncertainty. For AR4-Rinf, the LEV core moves downstream at a roughly constant velocity ($\sim 0.4u_\infty$), starting at $t = 0.2T$. This downstream motion is coupled to a vertical motion, which increases smoothly with time and reaches a broad maximum around $t/T \sim 0.4$, Note that, the uncertainty on $x_{w,c}$ and $z_{w,c}$ increases considerably during this phase in which $x_{w,c}$ grows linearly and $z_{w,c}$ remains almost constant. In case AR4-R020, $x_{w,c}$ starts to move downstroke at the same constant velocity than case AR4-Rinf somewhat later (at $t/T \sim 0.4$). Moreover, its maximum vertical displacement respect to the wing ($z_{w,c,\max}$) is smaller than in case AR4-Rinf, being $z_{w,c,\max} \sim 0.3c$ in the former case and $z_{w,c,\max} \sim 0.5c$ in the later.

At the mid-span, Figure 6.15*c* shows that eventually the LEV of all the cases move downstream at $0.4u_\infty$. The time instant when it happens decreases with R, i.e., it occurs before during the downstroke for the case AR4-Rinf than for AR4-R000. In the vertical direction (Figure 6.15*d*), the LEV core of the three cases start to separate from the wing at $t/T \sim 0.1$. This separation increases with time and is more pronounced as R increases, reaching a larger value of $z_{w,c,\max}$ in the heaving case. Finally, near the outboard wing tip, where the cases have a more similar α_e, the LEV core behaves almost equal. In all the cases it starts moving downstream and separating vertically from the wing at the same time, reaching the same value of $z_{w,c,\max}$. Note that the heaving case shows almost the same $x_{w,c}$ and $z_{w,c}$ as a function of time along y_w (i.e., at the three span sections shown), while in the flapping cases they increase with y_w. Thus, although $x_{w,c}$ and $z_{w,c}$ increase with time, it seems that the behavior of the LEV core along y_w during the downstroke is the same observed in Figure 6.11. It is important to note that the downstream velocity of the LEV core is the same for all cases in Table 6.1, regardless of the AR (see also discussion in 5).

As expected, the position of the LEV core during the downstroke is roughly the same independently of the AR and R at wing sections with the same α_e. For instance, Figure 6.16 compares the time history of $x_{w,c}$ and $z_{w,c}$ for cases AR2-R020 and AR4-R000, at the wing section located at $0.5c$ from the outboard wing tip. It can be observed that both the position and uncertainty of the LEV core is almost the same. Similar results are obtained near the inboard wing tip when the comparison is made for cases AR2-R000 and AR4-R000*, or AR2-R020 and AR4-R020* (not shown here).

The effect of α_e on the evolution of the LEV is evaluated next in two cases with the same R and AR. In Figure 6.17 the evolution of $x_{w,c}$ and $z_{w,c}$ is shown at two positions corresponding to 50% and 75% of the wing span for cases AR4-R000 and AR4-R000*. Figures 6.17*a* and 6.17*c* show that $x_{w,c}$ is almost equal during the downstroke in both cases at 50% and 75% of the span, respectively. Note that, although both lines do not coincide (especially at 75% of the span), the uncertainty regions overlap. This suggests that, despite the large difference of α_e during the downstroke motion between cases

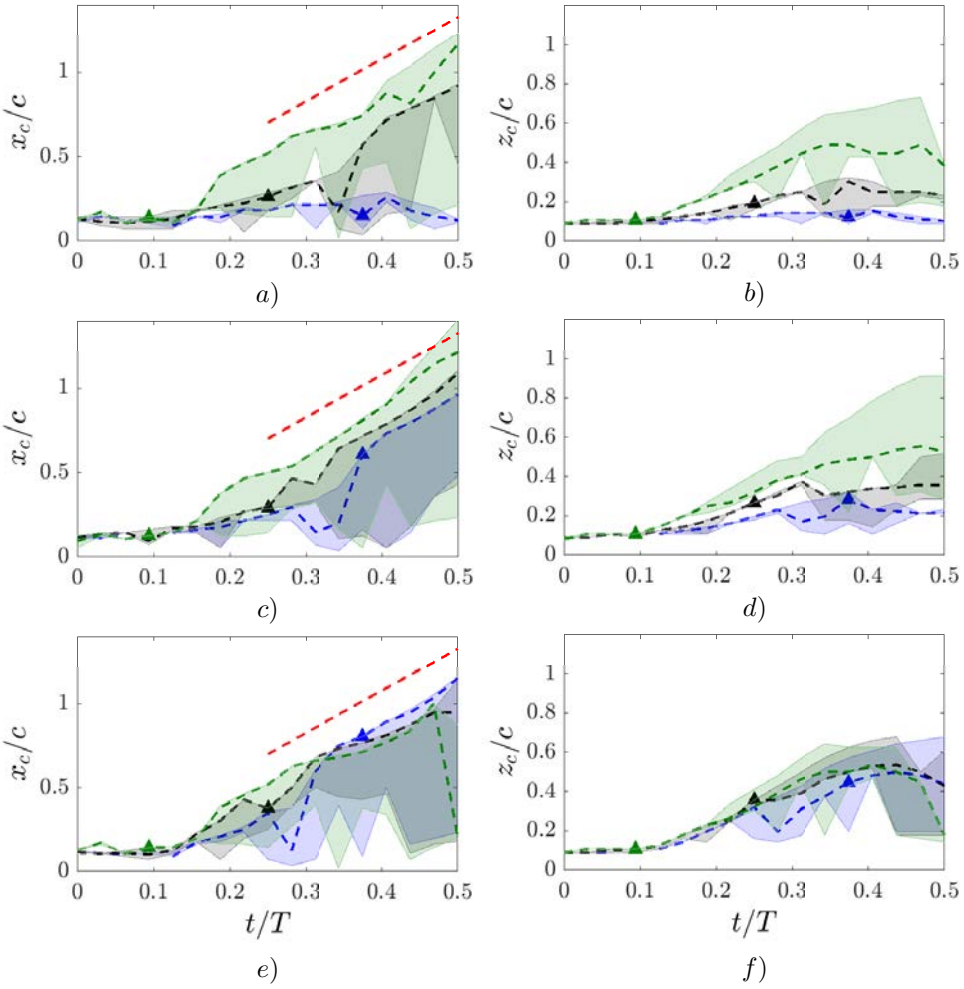

Figure 6.15: *a*),*c*),*e*) Streamwise and *b*),*d*),*f*) vertical coordinate of the LEV core for the cases with $AR = 4$ and equal h_0 as a function of time during the downstroke. The spanwise sections considered are $y_w/b = 0.25$ (*a*,*b*), $y_w/b = 0.5$ (*c*,*d*), and $y_w/b = 0.75$ (*e*,*f*). The cases are identified as in Figure 6.1. $Q'_{th}c^2/u_\infty^2 = 4$ has been selected to find the LEV core with the algorithm presented in chapter 5. The colored shaded area indicates the uncertainty in the position of the LEV. The red dashed lines in panels *a*), *c*) and *e*) are parallel to $x_c = 0.4u_\infty t$.

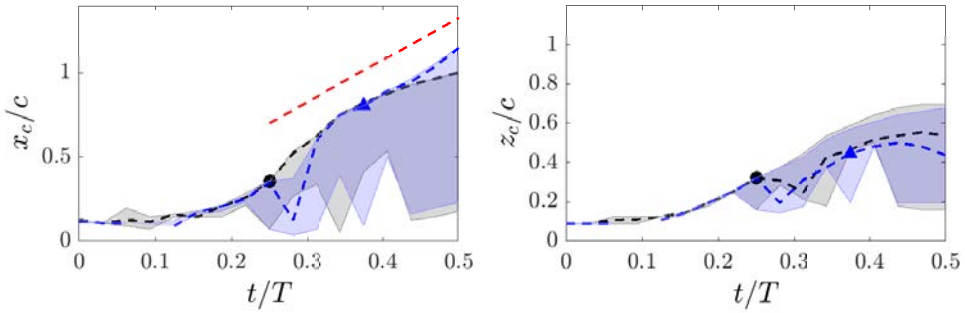

Figure 6.16: *a*) Streamwise and *b*) vertical coordinate of the LEV core for cases AR2-R020 and AR4-R000 as a function of time during the downstroke. The wing section shown is $y_w/b = 0.75$ for the case of $AR = 2$ and $y_w/b = 0.875$ for the $AR = 4$ case (both section are located at $0.5c$ from the outboard wing tip). The cases are identified as in Figure 6.1. $Q'_{th}c^2/u_\infty^2 = 4$ has been selected to find the LEV core with the algorithm presented in chapter 5. The colored shaded area indicates the uncertainty in the position of the LEV. The red dashed line in *a*) is parallel to $x_c = 0.4u_\infty t$.

AR4-R000 and AR4-R000*, the value of $x_{w,c}$ is mostly the same for both cases over the whole wing and for the whole downstroke motion, consistently with the results shown in Figure 6.13 at $t/T = 0.25$. In addition, $x_{w,c}$ of both cases moves downstream at $\sim 0.4u_\infty$, as in all the cases in Table 6.1.

On the other hand, the differences on the evolution of $z_{w,c}$ are smaller at the mid-span section (Figure 6.17*b*) than near the outboard wing tip (Figure 6.17*d*). In the section located at 75% of the span, the large uncertainty in $z_{w,c}$ (larger than 50%), suggests a possible detachment of the LEV. Moreover, this uncertainty is considerable larger in the case AR4-R000* than in case AR4-R000. Thus, this might be also related to the break down process of the LEV discussed below, and more clearly observed in animations (not shown).

The intensity of the LEV of cases AR4-R000 and AR4-R000* is studied during the downstroke motion in Figure 6.18. In this Figure, the same span sections analyzed in Figure 6.17 are shown. The circulation of both cases increases during the first half of the downstroke, while in the second half, its behaviour depends on the case. At the mid-span, Figure 6.18*a* shows that the increase of Γ_c is more pronounced in case AR4-R000* than in case AR4-R000 during $0 < t/T < 0.25$. After the mid-downstroke ($t/T = 0.25$), the difference of Γ_c between both cases is $\gtrsim 1.5u_\infty c$, being Γ_c of case AR4-R000* at least twice as large than in case AR4-R000. However, in the span section

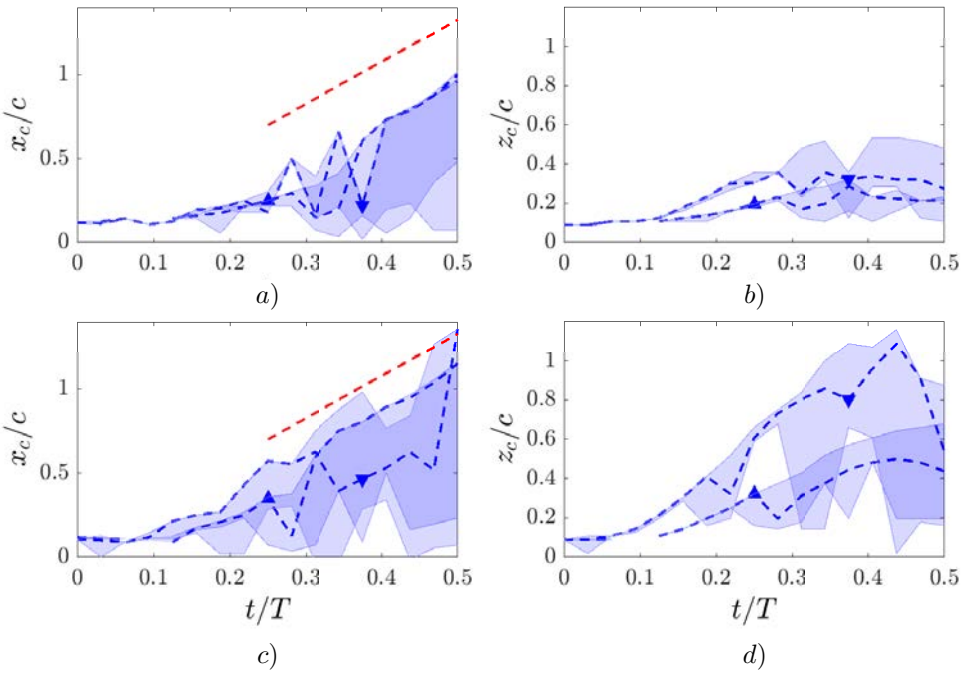

Figure 6.17: *a*),*c*) Streamwise and *b*),*d*) vertical coordinate of the LEV core for cases AR4-R000 and AR4-R000* as a function of time during the downstroke. The spanwise sections considered are $y_w/b = 0.5$ (*a*,*b*) and $y_w/b = 0.75$ (*c*,*d*). The cases are identified as in Figure 6.1. $Q'_{th}c^2/u_\infty^2 = 4$ has been selected to find the LEV core with the algorithm presented in chapter 5. The colored shaded area indicates the uncertainty in the position of the LEV. The red dashed lines in panels *a*) and *c*) are parallel to $x_c = 0.4u_\infty t$.

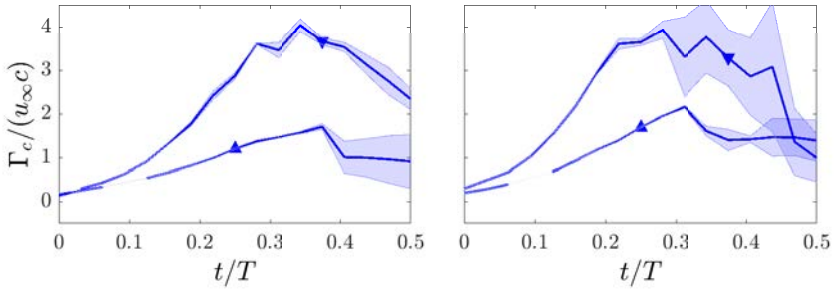

Figure 6.18: Circulation on the LEV core (Γ_c) during the downstroke motion at *a*) $y_w/b = 0.5$ and *b*) $y_w/b = 0.5$. Cases AR4-R000 and AR4-R000* are identified with (▲) and (▼) respectively. The colored shaded area indicates the uncertainty in Γ_c.

closer to the outboard tip (Figure 6.18*a*), the circulation of case AR4-R000* starts to decay abruptly after $t/T = 0.25$, while Γ_c of the case AR4-R000 remains nearly constant after $t/T \sim 0.35$. Remind that, as discussed in chapter 5 the behaviour observed for case AR4-R000 is consistent with an LEV being shed into the wake during the second half of the downstroke (i.e., constant downstream velocity of $x_{w,c}$ in Figures 6.17*a* 6.17*c*, and constant Γ_c in Figure 6.18). On the other hand, the decrease of Γ_c (and the increase of its uncertainty) during the second half of the downstroke of case AR4-R000* suggest that a different phenomenon is happening.

In order to analyze this phenomenon Figure 6.19 shows instantaneous visualizations of the LEV at two different times, $t/T = 0.25$ and $t/T = 0.38$. This figure shows the points of the vortex skeleton detected by the algorithm presented in chapter 5 at $y_w/b = 0.5$ and $y_w/b = 0.75$ for both cases (AR4-R000 and AR4-R000*). The LEV is depicted by the isosurface $Q' = 4{u_\infty}^2/c^2$ (translucent) and with chordwise-vertical planes located at $y_w/b = 0.5$ (blue) and $y_w/b = 0.75$ (orange). The points are shown with spheres inscribed in the isosurface (as in Figures 5.2*c* and 5.6).

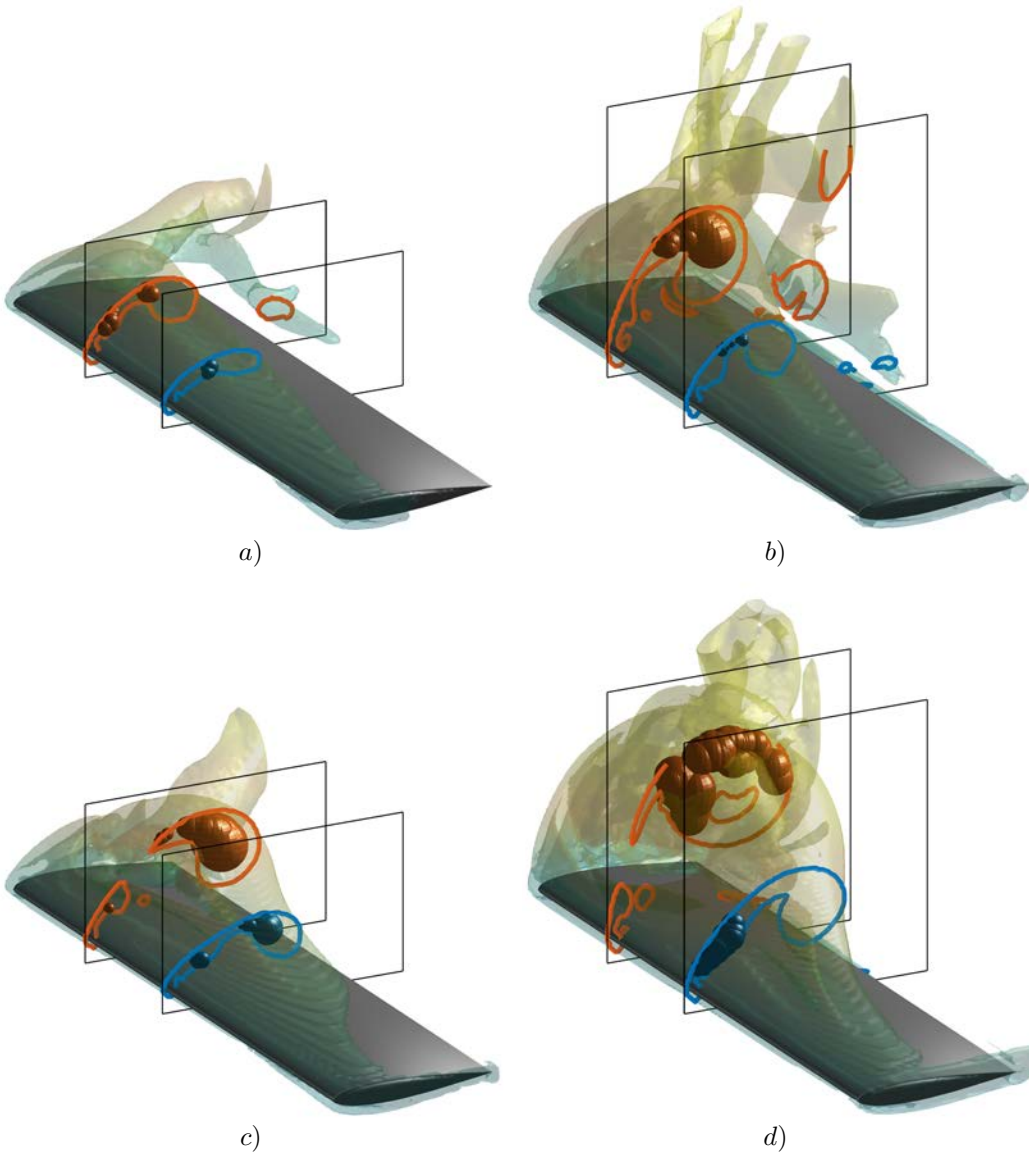

Figure 6.19: Isosurfaces of $Q' = 4.0{u_\infty}^2/c^2$ for cases AR4-R000 (*a*,*c*) and AR4-R000* (*c*,*d*) at $t/T = 0.25$ (*a*,*b*) and $t/T = 0.38$ (*c*,*d*). Panels also display the intersection of the planes $y/b = 0.5$ (blue) and $y/b = 0.75$ (orange) with the isosurfaces. The inscribed spheres associated to the skeleton points at these two spanwise location are also shown.

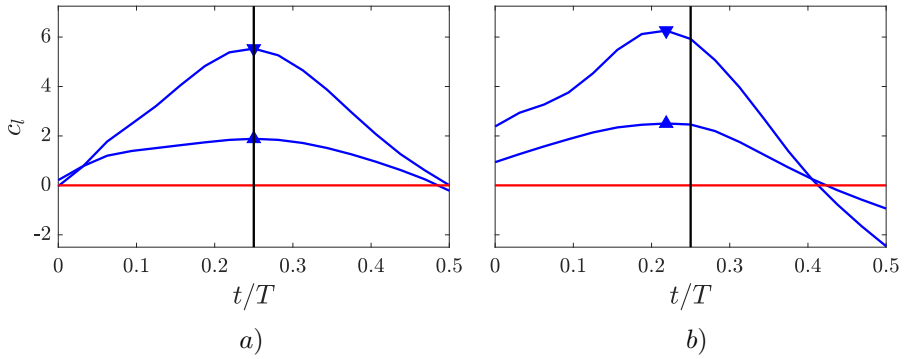

Figure 6.20: Sectional lift coefficient (c_l) of cases AR4-R000 (▲) and AR4-R000* (▼) during the downstroke motion at *a*) $y_w/b = 0.5$ and *b*) $y_w/b = 0.75$. The black vertical line indicates the mid-downstroke ($t/T = 0.25$) and the red horizontal line separates the positive from the negative c_l.

First, the cases are compared in terms of the size of the LEV. At both time instants and span sections depicted in Figure 6.19 the LEV is larger for case AR4-R000* than for case AR4-R000. Thus, the differences observed in the circulation of both cases (Figure 6.17) seems to be mostly related with that size increment. Note also, that the vertical separation respect to the wing of the LEV of both cases is alike, consistently with the uncertainty of $z_{w,c}$ observed in Figures 6.17*b* and 6.17*d*.

On the other hand, the uncertainty in Γ_c observed at $y_w/b = 0.75$ after the mid-downstroke seems to be linked with the separation of the LEV (orange lines in Figures 6.19*c* and 6.19*d*). Probably, this uncertainty is particularly larger for case AR4-R000*, since at $t/T = 0.38$ (Figure 6.19*d*) its LEV is already broken down close to the outboard wing tip.

Finally, the evolution of the sectional lift coefficient, c_l (defined in equation 5.9), is studied for AR4-R000 and AR4-R000* cases at the same positions (50% and 75% of the wing span) in Figure 6.20. The difference of c_l between both cases is large during almost the whole downstroke in both sections, becoming maximum when c_l peaks. At the mid-span of the wing, Figure 6.20*a* shows that the differences between the c_l of both cases is similar to those observed in Γ_c in Figure 6.18*a*. Similarly, at the section close to the outboard wing tip this happens during the first half of the downstroke. However, in the second half, the difference in Γ_c between both cases does not seem to be translated directly into c_l. Since this difference in Γ_c remain roughly constant until $t/T \sim 0.4$, while the difference in c_l starts decreasing from the mid-downstroke.

CHAPTER
SEVEN

Summary, conclusions and future work

7.1 Summary and conclusions/Resumen y conclusiones

Summary and conclusions

The main objective of this thesis was to obtain a deeper insight in the 3D aerodynamics of flapping wings in forward flight and, in particular, in the effect that a transition from heaving to flapping motion had on the aerodynamic forces and flow structures. To that end several numerical simulations of flapping wings of $AR = 2$ and 4 in forward flight at Reynolds number $Re = 500$ and reduced frequency $k = 1$ have been presented. The calculations were performed by solving the Navier-Stokes equations using an immersed boundary method, prescribing the motion of the wings. The simulations have been designed to study a smooth transition from a heaving motion to a flapping motion respect to its root by varying the radius of flapping motion, R. In this set of simulations, the vertical displacement of the outboard wing tip (h_0), has been kept fixed and equal to c. The motion imposed to the wings of all the cases is symmetric and therefore, the analyses are mainly focused on the downstroke motion.

Since the leading edge vortex (LEV) is one of the most important unconventional aerodynamic mechanisms providing lift augmentation in flapping wing aerodynamics, its characterization was of utmost importance to understand the transition studied. However, this characterization entailed several challenges since the LEV grows and evolves, and during the course of the flapping oscillation can present complicated shapes, including changes in the topology (i.e., splitting). In this thesis, a methodology to analyze the LEV that takes into account these complexities aiming to provide a quantitative description of the LEV have been proposed. The first step of the methodology involves the identification of the vortical structures surrounding the wing. The identification of the structures has been done employing an isosurface of the second invariant of the velocity gradient tensor, Q, but, in principle, it can be done with any of the methods existing in the literature [Chakraborty et al., 2005]. A sensitivity analysis was performed with different threshold values of Q to identify the vortex. The results of this analysis showed that the impact of the employed threshold to identify the vortex are minor, not influ-

encing the observed trends. The second step consists of the identification of the skeleton or core of the LEV using a thinning algorithm also available in the literature [Lee et al., 1994, Kerschnitzki et al., 2013]. The LEV is discriminated from the remaining vortical structures using the orientation of the vorticity vector and making use of additional geometrical considerations. The final step consists of the computation of relevant flow quantities along the LEV core. This is done by averaging the flow quantities within planes perpendicular to the local vorticity vector, which is used here to define the local direction of the LEV core.

The analysis of the aforementioned database has shown that for cases with equal h_0, the transition from heaving to flapping motion does not affect the shape of the curves of the time evolution of the streamwise (C_x) and vertical (C_z). Nonetheless, the other parameter that varied in the simulations, the aspect ratio (AR), does have an influence in the shape of the curve of the time evolution of C_x. The peaks of the aerodynamic forces increase with both R and AR, so that the forces are maxima for the heaving cases. The increments of these peaks are more affected by R than by AR, i.e., the differences are larger when compared between cases with different R and equal AR, than in cases with equal R and different AR. Note that in the heaving cases, all wing sections are subjected to the same local effective angle of attack (α_e). In the flapping cases α_e is roughly the same as in the heaving cases only near the outboard wing tip, however, in the former cases this value decreases from the outboard to the inboard wing tip, resulting in lower peaks of the forces. In order to confirm that the governing parameter in the variation of the aerodynamic forces is α_e, three additional simulations have been performed. The first one consists on a heaving wing with $AR = 2$ that moves with a smaller vertical displacement than the cases performed with a fixed h_0. The aerodynamic forces obtained in this case are very similar to those of the flapping wing simulation that rotates respect to its root and has the same averaged effective angle of attack along the wing span ($\langle\alpha_e\rangle$). The other two simulations consist in flapping wings ($R = 0$ and $R = 2$) of $AR = 4$ that move between the inboard wing tip and the mid-span equal to the wings of cases with $AR = 2$ and the same R. Therefore, these four cases have the same α_e in the span sections located at $0 < y_w/c < 2$, but the $AR = 4$ cases present larger values of h_0 and $\langle\alpha_e\rangle$ than the $AR = 2$ cases. These two cases with $AR = 4$ present peaks of aerodynamic forces notably larger than the corresponding $AR = 2$ cases, in fact, these values are even larger than those obtained in all the cases with equal h_0. Since this effect seems to be linked to the $\langle\alpha_e\rangle$, the mean vertical force has been analyzed as a function of $\langle\alpha_e\rangle_{\max}$, showing that $\overline{C_z}$ increases proportional to $\langle\alpha_e\rangle^n_{\max}$, where $1 < n < 2$. Thus, $\overline{C_z}$ shows a growth faster than the linear behavior predicted by potential theory.

The aerodynamic forces have been decomposed in tangential and normal components and their respective contributions to C_z (lift) and C_x (drag-thrust) have been analyzed.

In all cases, the vertical force is dominated by the normal force. However, the streamwise force is the result of a competition between normal contributions that produce thrust and tangential contributions that produce drag. In both contributions, the cases with larger $\langle\alpha_e\rangle_{\max}$ tend to provide larger thrust force (i.e., the normal contribution produce more thrust and the tangential contribution less drag). The time-averaged value of the normal contribution to C_x shows an increment with $\langle\alpha_e\rangle_{\max}$ slower than linear, far below the quadratic increment predicted by potential theory. The tangential contribution presents a decrease with $\langle\alpha_e\rangle_{\max}$ which is proportional to the increase observed in the normal contribution. However, the value obtained for the flapping case with $AR = 4$, $R = 0$ and no fixed h_0 does not fit in the trend observed for the rest of the $AR = 4$ cases. This case presents a similar $\langle\alpha_e\rangle_{\max}$ than the other flapping case with $AR = 4$ and no fixed h_0 ($R = 2$) and the heaving case with $AR = 4$, however, it produces a larger drag reduction. This discrepancy has been investigated through the local tangential force coefficient and the flow structures around the wing at the time instant when the tangential contribution to C_x differs more with the other two cases. The local tangential force coefficient shows that the larger differences between these cases appear in a region close to the outboard wing tip and after the mid-chord. At this region, the case with larger drag reduction presents a broken down tip vortex (TiV) near the outboard wing tip that does not appear in the other two cases. Additionally, it has been observed that the differences between the tangential contributions of the cases with different R and equal h_0 seem to be linked to the position of the stagnation point. This position is located nearest to the leading edge in cases with smaller R, therefore it seems to be controlled by α_e.

The normal contribution to the vertical force has been analyzed using the distribution of the normal force per unit area (c_n). This distribution shows a lower suction in the upper surface of the wing near its inboard tip as R decreases for all the cases studied. Besides, these cases also show a large suction peak close to the outboard wing tip. The comparison of c_n on the upper surface of the wing for the heaving cases with equal h_0 shows that there is a region that does not seem to be affected by the TiVs. Interestingly, this region only appears in the $AR = 4$ case. Besides, in this region the suction has a similar value than the one observed in the peak found close to the outboard wing tip. Moreover, c_n has also been compared in the flapping cases with same R and h_0 but different AR. These cases show differences close to the inboard wing tip and similarities close to the outboard wing tip, where they present a more similar value of α_e. The similarities of c_n observed at sections with similar α_e have been confirmed through the comparison of the cases with equal α_e between $0 < y_w/c < 2$, and comparing two cases with equal h_0 and different R and AR that present the same value of α_e near the outboard wing tip.

Regarding the analysis of the flow structures it has been shown that the flow over

the wings of all cases is rather complex, with the presence of an LEV and TiVs, which interact and are shed into the wake forming ring-like structures. The rings are clearly visible for the cases with large R. For smaller R, the displacement of the inboard wing tip decreases and the intensity of the LEV decreases from the outboard to the inboard wing tip, forming a conical-shaped LEV. Besides, the inboard wing tip vortices also become less intense as R decreases, disappearing when $R = 0$. For this case, the vortical structures shed into the wake are half-rings. The LEV separation has been analyzed first qualitatively, studying its correlation with the normal force distribution on the upper surface of the wing. In this analysis it has been observed that the spanwise location where the separation of the LEV occurs depends on R. For the heaving cases, the LEV separates earlier near the mid-span, while for the flapping cases, the LEV separates earlier near the outer wing tip. In the cases with larger h_0, the LEV starts to separate from the wing before than in the cases with $h_0 \leq c$. Since these two cases (with $h_0 > c$) have larger values of α_e close to the outboard wing tip, it seems that the LEV structure is also linked to α_e, as it happened in the distribution of c_n. In fact, it has been shown that at the mid-downstroke the regions with similar c_n distributions in the upper surface also present alike LEVs.

The geometry of the LEV has been characterized quantitatively, by tracking, as a function of time, its core along the wing span during the downstroke. At the mid-downstroke, the LEV core of all cases with $h_0 = c$ presents similar chordwise and vertical positions near the outboard wing tip. For the heaving cases, the chordwise position of the LEV core is roughly constant along the wing span, except close to the wing tips. However, for the flapping cases, the LEV core is found closer to the leading edge of the wing as y_w decreases. As R decreases, the LEV approaches the leading edge of the wing, independently of the AR. The comparison of the location of the LEV core at sections with the same α_e, has confirmed that the local structure of the LEV is linked to this parameter. However, by comparing two cases with different value of $\langle\alpha_e\rangle$ and the same values of R and AR, it has been observed that while the vertical position of the LEV core is affected by α_e, the chordwise position is not.

In addition to the geometrical characterization of the LEV, the local circulation of the LEV (i.e., the intensity of the LEV) has been analyzed. The distribution of local circulation along the wing span (y_w) of each case is similar to their distributions of α_e and of the local contribution of the normal force to C_z along y_w. This suggests that the local α_e is linked also with the intensity of the LEV in addition to its structure and location, and therefore, it is the main responsible of the change in the local aerodynamic forces.

The evolution of the LEV has been analyzed during the downstroke at the wing sections located at the mid-span and close to the outboard wing tip. At these sections the motion of the LEV core can be divided in two different phases. The first one

starts at the beginning of the downstroke and is characterized because the LEV core moves downstream and vertically at a slow but increasing pace. In the second phase, which starts at a time instant that depends on the α_e of the span section analyzed, the convection velocity of the LEV core in the chordwise direction becomes rather constant. This suggests that its detachment from the wing has started. At the mid-span, the second phase (i.e., the detachment of the LEV) starts earlier for larger R in cases with $h_0 = c$. At the section close to the outboard wing tip, the LEV detachment starts at the same time instant, since the cases with $h_0 = c$ present similar values of α_e. For the flapping cases, the analysis shows that the LEV starts to detach from the wing near its outboard tip and then the process continue towards the inboard wing tip. Although for cases with small R, the LEV does not detach from the wing near its inboard tip. For the cases with $h_0 = c$ the relative vertical distance of the LEV core to the wing increases with R at the span sections analyzed, except close to the outboard wing tip, where the cases have similar values of α_e. The similarities observed in the position of the LEV during the whole downstroke at regions with comparable values of α_e have been confirmed by analyzing the cases that have the same α_e near the inboard or the outboard wing tip. For the flapping cases with the same R and AR, and different value of $\langle\alpha_e\rangle$, the LEV core motion shows the same two phases observed observed in the cases with $h_0 = c$. However, while the chordwise component of the LEV core remains almost equal during the downstroke, the vertical component is found more separated to the wing for the cases with larger α_e. Furthermore, at this second phase, it has also been observed that the uncertainty in the position of the LEV core increases. Flow visualizations have shown that this large uncertainty is associated to the subsequent splitting of the LEV. This splitting causes a "y"-shaped LEV to develop, which has one branch that is advected downstream at a roughly constant velocity ($\sim 0.4u_\infty$), and that eventually either breaks down or is shed into the wake.

The local circulation, Γ_c, has also been studied during the downstroke to quantify the intensity of the LEV of the flapping cases with equal R and AR, and different $\langle\alpha_e\rangle$. At the mid-span, Γ_c increases faster at the beginning of the downstroke for the case with larger $\langle\alpha_e\rangle$. After the mid-downstroke, its magnitude is almost twice that observed in the case with smaller $\langle\alpha_e\rangle$. However, closer to the outboard tip the local circulation of the former case begins to decay abruptly after the mid-downstroke, while Γ_c of the latter remains roughly constant after a time instant slightly lagged respect to the mid-downstroke. Moreover, the uncertainty of Γ_c of the case with larger $\langle\alpha_e\rangle$ is considerably larger after the mid-downstroke than the one observed in the case with smaller $\langle\alpha_e\rangle$. Flow visualizations have shown that this difference in the uncertainty is linked to the break down of the LEV of the case with larger $\langle\alpha_e\rangle$ near the outboard wing tip. In addition, these visualizations suggest that at the mid-span and close to the outboard wing tip the intensity of the LEV is related with the size of the LEV for time instants

before the mid-downstroke.

This analysis has been closed by studying the sectional lift coefficient, c_l in both sections (mid-span and section close to the outboard wing tip). The differences observed in c_l at the mid-span and at the first half of the downstroke in the region close to the outboard wing tip are associated to the intensity of the LEV (i.e., Γ_c). However, at the section close to the outboard wing tip, the differences observed in Γ_c during the second half of the downstroke are not directly translated into differences of c_l. This suggest that the relative vertical distance of the LEV to the wing might has also influence in the c_l, especially when it is large.

Finally, the ability of unsteady potential flow methods for predicting the aerodynamic forces on flapping wings with $AR = 2$ have been explored. When comparing to the DNS data, a very good agreement for the lift coefficient and a poor prediction of the drag coefficient are found. Even if the lift coefficient is well predicted, it has been shown that the normal force distribution on the surface of the wing obtained from the unsteady potential flow method is very different to that obtained in the DNS. Thus, these methods should not be used for the prediction of other quantities of aerodynamic interest like the pitching moment coefficient.

Resumen y conclusiones

El objetivo principal de esta tesis era lograr entender mejor la aerodinámica tridimensional de alas batientes en vuelo en avance. En particular, queríamos comprender el efecto de la transición entre alas que oscilan verticalmente y alas que rotan respecto de sus respectivas raíces en las fuerzas aerodinámicas y en las estructuras del flujo. Para ello, se han realizado una serie de simulaciones numéricas que estudian un flujo con un número de Reynolds, $Re = 500$ alrededor de varias alas batientes en vuelo en avance. Las alas que se han considerado tienen distintas relaciones de aspecto ($AR = 2$ y 4) y se mueven con la misma frecuencia reducida ($k = 1$). En las simulaciones se han resuelto las ecuaciones de Navier-Stokes asumiendo un flujo incompresible, la interación entre el fluido y las alas se ha realizado mediante un método de las fronteras embebidas y el movimiento de las últimas ha sido prescrito. Las simulaciones se diseñaron para poder estudiar de forma suave la transición decrita anteriormente, para ello, se ha variado el radio del movimiento de aleteo, R. En estas simulaciones, el desplazamiento vertical de la punta exterior del ala (h_0), se ha mantenido fijo e igual a c. Además, el movimiento impuesto en las alas de todos los casos es simétrico y, por lo tanto, los análisis se centran principalmente en el movimiento de descenso del ala.

Según la literatura, el torbellino que aparece en el borde de ataque (TBA) es uno de los mecanismos aerodinámicos no convencionales más importantes para la generación de sustentación en la aerodinámica de alas batientes. Por lo que su caracterización es de

suma importancia para comprender por completo la transición estudiada. Sin embargo, esta caracterización supone varios desafíos, ya que el TBA crece y evoluciona durante el movimiento de aleteo, desarrollando en algunos casos formas complicadas. En ocasiones, estos cambios modifican por completo la topología del TBA, llegando incluso a dividirse en varias estructuras. Para analizar el TBA, en esta tesis se ha desarrollado una metodología que tiene en cuenta estas complejidades y que nos permite proporcionar una descripción cuantitativa del TBA. El primer paso de esta metodología consiste en identificar las estructuras de torbellinos que rodean el ala. La identificación de las estructuras se ha realizado empleando una iso-superficie del segundo invariante del tensor del gradiente de velocidad, Q, pero, en principio, podría realizarse con cualquiera de los métodos que existen en la literatura [Chakraborty et al., 2005]. Como Q identifica torbellinos basándose en un umbral, se ha realizado un análisis de sensibilidad usando diferentes umbrales. Los resultados de este análisis mostraron que el impacto del umbral empleado para identificar los torbellinos es pequeño, y no tine gran influencia en las tendencias de las variables estudiadas. El segundo paso consiste en la identificación del esqueleto o centro del TBA utilizando un algoritmo de adelgazamiento que también está disponible en la literatura [Lee et al., 1994, Kerschnitzki et al., 2013]. Posteriormente, el TBA se discrimina del resto de estructuras de torbellinos utilizando la orientación del vector de vorticidad y haciendo uso de consideraciones geométricas adicionales. El último paso consiste en calcular varaibles que dan información sobre el flujo a lo largo del centro del TBA. Esto se hace promediando estas variables del flujo en planos perpendiculares al vector de vorticidad local, que se usa en este método para definir la dirección local del TBA.

El análisis de la base de datos mencionada anteriormente ha mostrado que en casos con el mismo h_0, la transición entre el movimiento de oscilación vertical y el de aleteo no afecta a la forma de las curvas de la evolución temporal de los coeficientes de fuerza en la dirección del flujo (C_x), ni en la dirección vertical (C_z). No obstante, el otro parámetro que variaba entre las simulaciones, la relación de aspecto (AR) sí que tiene influencia en la forma de las curvas de la evolución temporal de C_x. La picos de las fuerzas aerodinámica aumentan tanto con R como con AR, por lo que las fuerzas son máximas en los casos en los que las alas oscilacilan verticalmente. Los incrementos de estos picos se ven más afectados por R que por AR, es decir, sus diferencias son mayores cuando se comparan casos con diferente R y misma AR, que al comparar casos con el mismo R y distinta AR. Tenga en cuenta que en los casos que oscilan verticalmente, todas las secciones del ala tienen el mismo ángulo de ataque local efectivo (α_e). En los casos de aleteo α_e sólo es similar al de los casos que oscilan verticalmente cerca del borde exterior del ala, para secciones del ala más alejadas de ese borde, el valor de α_e va disminuyendo hasta llegar a un mínimo en el borde interior del ala. Este cambio de α_e a lo largo de la dirección de la envergadura del ala (y_w) se traduce en la obtención

de picos de fuerzas más bajos (es decir, para valores de R menores, los picos de fuerzas son más pequeños). Para poder confirmar que el parámetro que rige los cambios en las fuerzas es α_e, se han realizado tres simulaciones adicionales. La primera de ellas consiste en un ala con $AR = 2$ que oscila verticalmente con h_0 más pequeño que el de los casos con descritos anteriormente. Las fuerzas aerodinámicas obtenidas en este caso son muy parecidas a las de la simulación del ala batiente que rota con respecto de su raíz y que tiene el mismo ángulo de ataque efectivo medio a lo largo del ala ($\langle\alpha_e\rangle$). Las otras dos simulaciones consisten en alas batientes con $R = 0$ y 2 y con $AR = 4$ que se mueven entre la punta interior del ala y la mitad de la envergadura del ala de la misma forma que las alas de los casos con $AR = 2$ y el mismo R. Por lo tanto, estos cuatro casos tienen el mismo α_e en las secciones de la envergadura ubicadas entre $0 < y_w/c < 2$, pero los casos con $AR = 4$ obtienen valores mayores de h_0 y de $\langle\alpha_e\rangle$ que los casos con $AR = 2$. Estos dos casos con $AR = 4$ muestran fuerzas aerodinámicas máximas notablemente más elevadas que los casos con $AR = 2$ y el mismo R, de hecho, estos valores son incluso más elevados que los obtenidos en todos los casos que tienen $h_0 = c$. Dado que este efecto parece estar relacionado con $\langle\alpha_e\rangle$, la fuerza vertical media ($\overline{C_z}$) se ha analizado en función de $\langle\alpha_e\rangle_{\max}$. Este análisis ha mostrando que $\overline{C_z}$ aumenta de forma proporcional a $\langle\alpha_e\rangle^n_{\max}$, siendo $1 < n < 2$, por lo que su crecimiento es más rápido que el comportamiento lineal que predice la teoría potencial.

Las fuerzas aerodinámicas se han descompuesto en sus componentes tangencial y normal y sus respectivas contribuciones a C_z (sustentación) y a C_x (resistencia-empuje) se han analizado. En todos los casos, la fuerza vertical está dominada por la fuerza normal. Sin embargo, la fuerza en la dirección del flujo muestra que ambas contribuciones son parecidas, siendo las fuerzas normales las que producen empuje y las fuerzas tangenciales las que producen resistencia. En ambas contribuciones, los casos con mayor $\langle\alpha_e\rangle_{\max}$ tienden a proporcionar una mayor fuerza de empuje (es decir, la contribución normal produce más empuje y la contribución tangencial una mayor reducción de resistencia). El valor promediado en el tiempo de la contribución normal a la fuerza en la dirección del flujo ($\overline{C_x^n}$) muestra un incremento con $\langle\alpha_e\rangle_{\max}$ inferior a un comportamiento lineal, quedando muy por debajo del incremento cuadrático que predice la teoría potencial. La contribución tangencial ($\overline{C_x^\tau}$) presenta una disminución con $\langle\alpha_e\rangle_{\max}$ que es proporcional al aumento observado en $\overline{C_x^n}$. Sin embargo, el valor obtenido en el caso de aleteo con $AR = 4$, $R = 0$ y $h_0 \neq c$ no encaja en la tendencia que muestran el resto de casos con $AR = 4$. Este caso tiene un valor de $\langle\alpha_e\rangle_{\max}$ similar al del otro caso de aleteo con $AR = 4$ y $h_0 \neq c$ (con $R = 2$) y al caso del ala con $AR = 4$ que oscila vericalmente, sin embargo produce una reducción de resistencia mayor. Esta discrepancia se ha investigado mediante el coeficiente de fuerza tangencial local y las estructuras del flujo que aparecen cerca del ala en el instante en el que la contribución tangencial a C_x difiere más con los otros dos casos. El coeficiente de fuerza tangencial local muestra

que las mayores diferencias entre estos casos aparecen en una región cercana a la punta exterior del ala y pasada la mitad de la cuerda del ala. En esta región, el caso con mayor reducción de resistencia presenta un torbellino de punta de ala (TPA) cerca de la punta exterior del ala que no aparece en los otros dos casos. Además, se ha observado que las diferencias entre las contribuciones tangenciales de los casos con $h_0 = c$ y con R distintos parecen estar relacionadas con la posición en la que se encuentra el punto de remanso. Esta posición aparece más cerca del borde de ataque del ala en los casos con valores mas pequeños de R, por la tanto parece que también depende de α_e.

La contribución normal a la fuerza vertical se ha analizado utilizando la distribución de la fuerza normal por unidad de área (c_n). A medida que R disminuye, esta distribución muestra una succión menor en la superficie superior del ala cerca de su punta interior en todos los casos estudiados. Además, estos casos también muestran un valor elevado de succión cerca de la punta exterior del ala. La comparación de c_n en la superficie superior del ala de los casos con $h_0 = c$ que oscilan verticalmente muestra que hay una región que no parece afectada por los TsPA. Curiosamente, esta región sólo aparece en el caso del ala con $AR = 4$. Además, en esta región la succión tiene un valor similar al observado en el pico de succión encontrado cerca de la punta exterior del ala. Por otra parte, c_n también se ha comparado en casos de aleteo con el mismo R y h_0, pero distinta AR. Estos casos muestran diferencias cerca de la punta interior del ala y similitudes cerca de la punta exterior del ala, donde presentan un valor de α_e más parecido. Las similitudes en c_n observadas en secciones con α_e parecidos han sido confirmadas mediante la comparación de los casos con el mismo α_e entre $0 < y_w/c < 2$, y comparando dos casos con el mismo h_0 y con diferentes R y AR que presentan el mismo α_e cerca de la punta exteior del ala.

En cuanto al análisis de las estructuras del flujo, se ha demostrado que el flujo sobre las alas de todos los casos es bastante complejo, siendo posible identificar el TBA y los TsPA, que interactúan y se desprenden a la estela formando estructuras con forma de anillos. Los anillos son claramente visibles para casos con un valor de R elevado. Para casos con R más pequeño, el desplazamiento de la punta interior del ala disminuye y la intensidad del TBA disminuye desde la punta exterior del ala hasta su punta interior, formando un TBA con forma cónica. Además, los TPA también se vuelven menos intensos a medida que R disminuye, desapareciendo cuando el $R = 0$. Para este caso, las estructuras de torbellinos desprendidas a la estela tienen forma de medios anillos. La separación del TBA se ha analizado primero cualitativamente, estudiando su correlación con la distribución de la fuerza normal en la superficie superior del ala en el instante en el que el ala ha recorrido la mitad del movimiento de descenso. En este análisis se ha observado que la sección de la envergadura del ala donde ocurre la separación del TBA depende de R. Para los casos que oscilan verticalmente, el TBA se separa antes cerca de la sección media de la envergadura, mientras que para los casos que aletean,

el TBA se separa antes cerca de la punta exterior del ala. En los casos con un valor mayor de h_0, el TBA comienza a separarse del ala antes que en los casos que tienen un valor de $h_0 = c$ o menor. Dado que estos dos casos (con $h_0 > c$) tienen valores de α_e mayores cerca de la punta exterior del ala, parece que la estructura local del TBA y su separción también están ligadas a α_e, como ocurría en la distribución de c_n. De hecho, se ha observado que en la mitad del movimiento de descenso del ala, las regiones que tienen distribuciones de c_n en la superficie superior del ala parecidas también presentan TBAs con una estructura similar.

La geometría del TBA se ha caracterizado cuantitativamente, siguiendo su centro a lo largo de la envergadura del ala y en función del tiempo durante el movimiento de descenso del ala. Durante este periodo de tiempo, el centro del TBA de todos los casos con $h_0 = c$ tiene una posición, en la dirección vertical y en la dirección de la cuerda del ala, parecida en las zonas cercanas a la punta exterior del ala. En los casos que oscilan verticalmente, la posición del TBA en la dirección de la cuerda del ala es aproximadamente constante a lo largo de la envergadura de la misma, excepto cerca de sus puntas. Sin embargo, para los casos de aleteo, el TBA se encuentra más cerca del borde de ataque del ala a medida que y_w disminuye. A medida que R disminuye, el TBA se acerca al borde de ataque del ala, independientemente del valor de AR. La comparación de la ubicación del centro del TBA en secciones con el mismo α_e ha confirmado que la estructura local del TBA está relacionada con este parámetro. Sin embargo, al comparar dos casos con un valor del $\langle \alpha_e \rangle$ diferente y con los mismos valores de R y de AR, se ha observado que mientras que la posición vertical del centro del TBA está afectada por α_e, la posición en la dirección de la cuerda del ala no lo está.

Además de la caracterización geométrica del TBA, la circulación local del TBA (es decir, la intensidad del TBA) se ha analizado. La distribución de la circulación local a lo largo del ala (es decir, a lo largo de y_w) de cada caso es similar a sus distribuciones de α_e y de la contribución local de la fuerza normal a C_z a lo largo de y_w. Esto sugiere que α_e también está relacionado con la intensidad del TBA además de con su estructura y ubicación, y por lo tanto, es el principal responsable del cambio en las fuerzas aerodinámicas locales.

La evolución del TBA se ha analizado durante el movimiento de descenso del ala en las secciones del ala ubicadas en la mitad de su envergadura y cerca de la punta exterior del ala. En estas secciones el movimiento del centro del TBA se puede dividir en dos fases distintas. La primera de ellas comienza al principio del movimiento de descenso del ala y se caracteriza porque en ella el centro del TBA se mueve aguas abajo y verticalmente a un ritmo lento pero creciente. En la segunda fase, que comienza en un instante de tiempo que depende del valor de α_e en la sección del ala analizada, la velocidad de advección del centro del TBA en la dirección de la cuerda del ala se vuelve constante. Esto sugiere que su separación con respecto del ala ha comenzado. En la mitad de la envergadura del

ala, la segunda fase (es decir, la separación del TBA) comienza antes para valores de R más grandes en los casos con $h_0 = c$. En la sección cercana a la punta exterior del ala, la separación del TBA comienza en el mismo instante de tiempo en estos casos, ya que todos tienen valores similares de α_e. En concreto, para los casos de aleteo , el análisis muestra que el TBA comienza a desprenderse del ala cerca de su punta exterior y luego el proceso continúa hacia la punta interior del ala. Aunque para casos con valores de R pequeños, el TBA no se separa del ala cerca de su punta interior. Para los casos con $h_0 = c$, la distancia vertical relativa entre el centro del TBA y el ala aumenta con R en las secciones del ala analizadas, excepto cerca de su punta exterior, donde los casos tienen valores de α_e parecidos. Las similitudes observadas en la posición del TBA durante el movimiento de descenso del ala en regiones con valores comparables de α_e, se han confirmado mediante el analisis de los casos que tienen el mismo α_e cerca de la punta interior o exterior del ala. Para los casos de alas aleteando que tienen los mismos valores de R y de AR, y un valor distinto del $\langle\alpha_e\rangle$, el movimiento del centro del TBA muestra las mismas dos fases que se observaron en los casos con $h_0 = c$. Sin embargo, mientras que la componente del centro del TBA en la dirección de la cuerda permanece casi igual durante el movimiento de descenso del ala, la componente vertical se encuentra más separada del ala para los casos con mayor α_e. Además, en esta segunda fase, también se ha observado que aumenta la incertidumbre de la posición del centro del TBA. Las visualizaciones del flujo han demostrado que esa alta incertidumbre está asociada a la división del TBA. Esta división hace que se forme un TBA con forma de "y", que tiene una rama que es adveccionada aguas abajo a una velocidad aproximadamente constante ($\sim 0.4u_\infty$) y que finalmente se rompe o se desprende a la estela.

La circulación local, Γ_c, también se ha estudiado durante el movimiento de descenso del ala para cuantificar la intensidad del TBA de los casos con un movimiento de aleteo con R y AR iguales, y un valor del $\langle\alpha_e\rangle$ distinto. En la mitad de la envergadura del ala, la Γ_c aumenta más rápido al comienzo de movimiento de descenso del ala para el caso con mayor $\langle\alpha_e\rangle$. Pasada la mitad del movimiento de descenso, su magnitud es casi el doble que la del caso con menor $\langle\alpha_e\rangle$. Sin embargo, más cerca de la punta exterior del ala, la circulación del primer caso comienza a decaer bruscamente después de la mitad del movimiento de descenso del ala, mientras que la Γ_c del último caso permanece aproximadamente constante después de un instante de tiempo levemente posterior a la mitad del movimiento de descenso del ala. Además, la incertidumbre de la Γ_c del caso con mayor $\langle\alpha_e\rangle$ es considerablemente más grande después de la mitad del movimiento de descenso del ala que la del caso con un $\langle\alpha_e\rangle$ más pequeño. Las visualizaciones del flujo muestran que esta diferencia en la incertidumbre está relacionada con la rotura del TBA del caso con mayor $\langle\alpha_e\rangle$ cerca de la punta exterior del ala. Además, estas visualizaciones sugieren que en la mitad de la envergadura y cerca de la punta exterior del ala, la intensidad del TBA está asociada con el tamaño del mismo en instantes

anteriores a la mitad del movimiento de descenso del ala.

El análisis se ha cerrado estudiando el coeficiente de sustentación local (c_l) en ambas secciones del ala (mitad de la envergadura y sección cercana a la punta exterior). Las diferencias observadas en el c_l en la mitad de la envergadura y en la primera mitad del movimiento de descenso del ala en la región cercana a la punta exterior del ala están asociadas a la intensidad del TBA (es decir, a la Γ_c). Sin embargo, en la sección cercana a la punta exterior del ala, las diferencias observadas en la Γ_c durante la segunda mitad del movimiento de descenso del ala no se traducen directamente en diferencias en el c_l. Lo que sugiere que la sepación vertical del TBA también puede tener influencia en el c_l, sobre todo cuando es grande.

Por último, se ha explorado la capacidad que tienen los métodos no estacionarios de flujo potencial para predecir las fuerzas aerodinámicas en alas batientes con $AR = 2$. Al comparar la solucón obtenida con los datos de las simulaciones numéricas directas, se obtienen resultados muy parecidos del coeficiente de sustentación y predicciones del coeficiente de resistencia bastante pobres. Incluso cuando el coeficiente de sustentación está bien predecido, se ha observado que la distribución de fuerza normal en la superficie del ala, obtenida mediante el método no estacionario de flujo potencial, es muy diferente a la obtenida con las simulaciones numéricas directas. Por lo tanto, estos métodos no deberían usarse para la predecir otras cantidades aerodinámicas de interés como el coeficiente del momento de cabeceo.

7.2 Future work

First it would be interesting to evaluate whether the hypothesis of a symmetry plane between the wings is also valid for the case where non-periodic forces appeared due to weak 3D secondary instabilities in the flow. Since TUCANREF is able to solve problems with larger domains than TUCAN, solve the same problem with two wings (without imposing any symmetry boundary condition) would be computationally affordable. Furthermore, other problems that would require a more accurate resolution near the wing, such us the influence of gust, could be solved using TUCANREF.

On the other hand, the LEV quantification method could be applied to a larger database that includes cases with pitching (or other kinematics and geometric parameters), with the aim of improving reduced-order aerodynamics models.

Bibliography

J.M. Anderson, K. Streitlien, K. S. Barret, and M. S. Triantafyllou. Oscillating foils of high propulsive efficiency. *J. Fluid Mech.*, 360:41–72, 1998.

R. Ansari, R. Zbikowski, and K. Knowles. Aerodynamic modelling of insect-like flapping flight for micro air vehicles. *Prog. Aerospace Sci.*, 42:129–172, 2006.

G. Arranz and O. Flores. Thrust generation in heaving and flapping wings in forward flight. AIAA Paper 2016-3556, 2016.

G. Arranz, A. Gonzalo, M. Uhlmann, O. Flores, and M. García-Villalba. A numerical study of the flow around a model winged seed in auto-rotation. in press, Flow Turbul. Combust., 2018a.

G. Arranz, M. Moriche, M. Uhlmann, O. Flores, and M. García-Villalba. Kinematics and dynamics of the auto-rotation of a model winged seed. *Bioinspir. Biomim.*, 13: 036011, 2018b.

Y. S. Baik, L. P. Bernal, K. Granlund, and M. V. Ol. Unsteady force generation and vortex dynamics of pitching and plunging aerofoils. *J. Fluid Mech.*, 709:37–68, 2012.

J. M. Birch and M. H. Dickinson. Spanwise flow and the attachment of the leading-edge vortex on insect wings. *Nature*, 412(6848):729–733, 2001.

J. M. Birch and M. H. Dickinson. The influence of wing–wake interactions on the production of aerodynamic forces in flapping flight. *J. Exp. Biol.*, 206(13):2257–2272, 2003.

J. M. Birch, W. B. Dickson, and M. H. Dickinson. Force production and flow structure of the leading edge vortex on flapping wings at high and low Reynolds numbers. *J. Exp. Biol.*, 207(7):1063–1072, 2004.

F. M. Bos, B. W. van Oudheusden, and H. Bijl. Wing performance and 3-D vortical structure formation in flapping flight. *J. Fluids Struct.*, 42:130–151, 2013.

M. Bross and D. Rockwell. Flow structure on a simultaneously pitching and rotating wing. *J. Fluid Mech.*, 756:354–383, 2014.

D. L. Brown, R. Cortez, and M. L. Minion. Accurate projection methods for the incompressible Navier–Stokes equations. *J. Comp. Phys.*, 168(2):464–499, 2001.

D. E. Calderon, D. J. Cleaver, I. Gursul, and Z. Wang. On the absence of asymmetric wakes for periodically plunging finite wings. *Phys. Fluids*, 26(7):349–376, 2014.

Z. R. Carr, C. Chen, and M. J. Ringuette. Finite-span rotating wings: three-dimensional vortex formation and variations with aspect ratio. *Exp. Fluids*, 54(2):1444, 2013.

P. Chakraborty, S. Balachandar, and R. J Adrian. On the relationships between local vortex identification schemes. *J. Fluid Mech.*, 535:189–214, 2005.

C. Chan-Braun, M. García-Villalba, and M. Uhlmann. Force and torque acting on particles in a transitionally rough open-channel flow. *J. Fluid Mech.*, 684:441–474, 2011.

C.-C. Chang. Potential flow and forces for incompressible viscous flow. *Proc. R. Soc. Lond. A*, 437(1901):517–525, 1992.

Y. H. Chen and M. Skote. Study of lift enhancing mechanisms via comparison of two distinct flapping patterns in the dragonfly sympetrum flaveolum. *Phys. Fluids*, 27(3): 033604, 2015.

J. Choi, T. Colonius, and D. R. Williams. Surging and plunging oscillations of an airfoil at low Reynolds number. *J. Fluid Mech.*, 763:237–253, 2015.

GCHE De Croon, M Perçin, BDW Remes, R Ruijsink, and C De Wagter. *The DelFly*. Springer, 2016.

J. C. del Álamo and J. Jiménez. Spectra of the very large anisotropic scales in turbulent channels. *Phys. Fluids*, 15(6):L41–L44, 2003.

M. H. Dickinson, F.-O. Lehmann, and S. P. Sane. Wing rotation and the aerodynamic basis of insect flight. *Science*, 284(5422):1954–1960, 1999.

W. B. Dickson and M. H. Dickinson. The effect of advance ratio on the aerodynamics of revolving wings. *J. Exp. Biol.*, 207(24):4269–4281, 2004.

H. Dong, R. Mittal, and F. M. Najjar. Wake topology and hydrodynamic performance of low-aspect-ratio flapping foils. *J. Fluid Mech.*, 566:309–343, 2006.

C. P. Ellington. The aerodynamics of hovering insect flight. IV. Aerodynamic mechanisms. *Philos. Trans. R. Soc. Lond., B, Biol. Sci.*, 305(1122):79–113, 1984.

C. P. Ellington, C. Van Den Berg, A. P. Willmott, and A. L. Thomas. Leading-edge vortices in insect flight. *Nature*, 384(6610):309, 1996.

P Fischer, , S Kerkemeier, J Lottes, A Tomboulides, A Obabko, E Merzari, Y Peet, A Peplinkski, O Marin, and R Rahaman. Nek5000: Oa fast scalable high-order solver for computational fluid dynamics. *Argonne National Laboratory,Illinois.*, 2008. Available: https://nek5000.mcs.anl.gov.

O. Flores, A. Gonzalo, M. Garcia-Villalba, L. Rossini, A. Hsiao, E. McVeigh, A. M. Kahn, and J. C. Del Alamo. Patient-specific analysis of blood stasis in the left atrium. In *APS Meeting Abstracts*, page L15.001, November 2016.

John W Gerdes, Satyandra K Gupta, and Stephen A Wilkerson. A review of bird-inspired flapping wing miniature air vehicle designs. *Journal of Mechanisms and Robotics*, 4(2):021003, 2012.

C. Geuzaine and J.-F. Remacle. Gmsh: A 3-d finite element mesh generator with built-in pre-and post-processing facilities. *Int. J. Numer. Methods Eng.*, 79(11):1309–1331, 2009.

A. Gonzalo, G. Arranz, M. Moriche, M. García-Villalba, and O. Flores. From flapping to heaving: a numerical study of wings in forward flight. submitted to J. Fluids Struct., 2018.

L. Graftieaux, M. Michard, and N. Grosjean. Combining PIV, POD and vortex identification algorithms for the study of unsteady turbulent swirling flows. *Meas. Sci. Tech.*, 12(9):1422, 2001.

J. M. Grasmeyer and M. T. Keennon. Development of the black widow micro air vehicle. *AIAA paper*, 127, 2001.

J.E. Guerrero. Wake signature and Strouhal number dependence of finite-span flapping wings. *J. Bionic Eng.*, 7:S109–S122, 2010.

I. Gursul and D. Cleaver. Plunging oscillations of airfoils and wings: Progress, opportunities, and challenges. *AIAA J.*, 2018. in press.

R. R. Harbig, J. Sheridan, and M. C. Thompson. Reynolds number and aspect ratio effects on the leading-edge vortex for rotating insect wing planforms. *J. Fluid Mech.*, 717:166, 2013.

R. R. Harbig, J. Sheridan, and M. C. Thompson. The role of advance ratio and aspect ratio in determining leading-edge vortex stability for flapping flight. *J. Fluid Mech.*, 751:71–105, 2014.

J. C. R. Hunt, A. A. Wray, and P. Moin. Eddies, streams, and convergence zones in turbulent flows. *Center For Turbulence Research*, Report CTR-S88, 1988.

HYPRE. High performance linear solvers for extreme-scale parallel supercomputers, 2018 August. URL https://computation.llnl.gov/projects/hypre-scalable-linear-solvers-multigrid-methods.

K. Isogai, Y. Shinmoto, and Y. Watanabe. Effects of dynamic stall on propulsive efficiency and thrust of flapping airfoil. *AIAA J.*, 37(10):1145–1151, 1999.

R. Jantzen, K. Taira, K. Granlund, and M. V. Ol. On the influence of pitching and acceleration on vortex dynamics around low-aspect-ratio rectangular wings. In *In: of the 51st AIAA Aerospace Sciences Meeting & Exhibit*, 2013.

R. T. Jantzen, K. Taira, K. O. Granlund, and M. V. Ol. Vortex dynamics around pitching plates. *Phys. Fluids*, 26(5):053606, 2014.

T. Jardin. Coriolis effect and the attachment of the leading edge vortex. *J. Fluid Mech.*, 820:312–340, 2017.

T. Jardin and L. David. Spanwise gradients in flow speed help stabilize leading-edge vortices on revolving wings. *Phys. Rev. E*, 90(1):013011, 2014.

T. Jardin, A. Farcy, and L. David. Three-dimensional effects in hovering flapping flight. *J. Fluid Mech.*, 702:102–125, 2012.

J. Jeong and F. Hussain. On the identification of a vortex. *J. Fluid Mech.*, 285:69–94, 1995.

A. R. Jones and H. Babinsky. Reynolds number effects on leading edge vortex development on a waving wing. *Exp. Fluids*, 51(1):197–210, 2011.

C.-K. Kang, H. Aono, Y. Sik Baik, L. P. Bernal, and W. Shyy. Fluid dynamics of pitching and plunging flat plate at intermediate Reynolds numbers. *AIAA J.*, 51(2): 315–329, 2012.

J. Katz and A. Plotkin. *Low-speed aerodynamics*. Cambridge Univ. Press, 2001.

M. Kerschnitzki, P. Kollmannsberger, M. Burghammer, G. N. Duda, R. Weinkamer, W. Wagermaier, and P. Fratzl. Architecture of the osteocyte network correlates with bone material quality. *J. Bone Miner. Res.*, 28(8):1837–1845, 2013.

J. Kim, P. Moin, and R. Moser. Turbulence statistics in fully developed channel flow at low Reynolds number. *J. Fluid Mech.*, 177:133–166, 1987.

D. Kolomenskiy, Y. Elimelech, and K. Schneider. Leading-edge vortex shedding from rotating wings. *Fluid Dyn. Res.*, 46(3):031421, 2014.

J. Kweon and H. Choi. Sectional lift coefficient of a flapping wing in hovering motion. *Phys. Fluids*, 22(7):071703, 2010.

T.-C. Lee, R. L. Kashyap, and C.-N. Chu. Building skeleton models via 3-D medial surface axis thinning algorithms. *CVGIP-Graph Model Im.*, 56(6):462–478, 1994.

Y. J. Lee, K. B. Lua, and T. T. Lim. Aspect ratio effects on revolving wings with Rossby number consideration. *Bioinspir. & Biomim.*, 11(5):056013, 2016.

D. Lentink and M. H. Dickinson. Rotational accelerations stabilize leading edge vortices on revolving fly wings. *J. Exp. Biol.*, 212(16):2705–2719, 2009.

G. C. Lewin and H. Haj-Hariri. Modelling thrust generation of a two-dimensional heaving airfoil in a viscous flow. *J. Fluid Mech.*, 492:339–362, 2003.

G. Liu, H. Dong, and C. Li. Vortex dynamics and new lift enhancement mechanism of wing–body interaction in insect forward flight. *J. Fluid Mech.*, 795:634–651, 2016.

L. N. Long and T. E. Fritz. Object-oriented unsteady vortex lattice method for flapping flight. *J. Aircraft*, 41(6):1275–1290, 2004.

A. P. Maertens and G. D. Weymouth. Accurate Cartesian-grid simulations of near-body flows at intermediate Reynolds numbers. *Comput. Meth. Appl. Mech. Eng.*, 283:106–129, 2015.

A. Martín-Alcántara, R. Fernández Feria, and E. Sanmiguel-Rojas. Vortex flow structures and interactions for the optimum thrust efficiency of a heaving airfoil at different mean angles of attack. *Phys. Fluids*, 27:073602, 2015.

M. Moriche. *A numerical study on the aerodynamic forces and the wake stability of flapping flight at low Reynolds number*. PhD thesis, Univ. Carlos III Madrid, 2017.

M. Moriche, O. Flores, and M. García-Villalba. Three-dimensional instabilities in the wake of a flapping wing at low Reynolds number. *Int. J. Heat Fluid Flow*, 62:44–55, 2016.

M. Moriche, O. Flores, and M. García-Villalba. On the aerodynamic forces on heaving and pitching airfoils at low Reynolds number. *J. Fluid Mech.*, 828:395–423, 2017.

S. J. Morris. Design and flight test results for micro-sized fixed-wing and vtol aircraft. In *Proceedings of the First International Conference on Emerging Technologies for Micro Ai Vehicles, Georgia Institute of Technology, Atlanta, GA*. Citeseer, 1997.

H. Nagai, K. Isogai, T. Fujimoto, and T. Hayase. Experimental and numerical study of forward flight aerodynamics of insect flapping wing. *AIAA J.*, 47(3):730, 2009.

C. A. Ozen and D. Rockwell. Three-dimensional vortex structure on a rotating wing. *J. Fluid Mech.*, 707:541–550, 2012.

P.-O. Persson, D. J. Willis, and J. Peraire. Numerical simulation of flapping wings using a panel method and a high-order Navier–Stokes solver. *Int. J. Num. Meth. Eng.*, 89 (10):1296–1316, 2012.

C. S. Peskin. The immersed boundary method. *Acta Numer.*, 11:479–517, 2002.

D. J. Pines and F. Bohorquez. Challenges facing future micro-air-vehicle development. *J. Aircraft*, 43(2):290–305, 2006.

C. W. Pitt Ford and H. Babinsky. Lift and the leading-edge vortex. *J. Fluid Mech.*, 720:280–313, 2013.

E. C. Polhamus. A concept of the vortex lift of sharp-edge delta wings based on a leading-edge-suction analogy. NASA Tech Note D-3767, 1966.

M. M. Rai and P. Moin. Direct simulations of turbulent flow using finite-difference schemes. *J. Comp. Phys.*, 96(1):15–53, 1991.

D. A. Read, F. S. Hover, and M. S. Triantafyllou. Forces on oscillating foils for propulsion and maneuvering. *J. Fluids Struct.*, 17(1):163–183, 2003.

B. A. Roccia, S. Preidikman, J. C. Massa, and D. T. Mook. Modified unsteady vortex-lattice method to study flapping wings in hover flight. *AIAA J.*, 51(11):2628–2642, 2013.

A. M. Roma, C. S. Peskin, and M. J. Berger. An adaptive version of the immersed boundary method. *J. Comp. Phys.*, 153(2):509–534, 1999.

P. G. Saffman and J. S. Sheffield. Flow over a wing with an attached free vortex. *Stud. Appl. Maths*, 57(2):107–117, 1977.

S. P. Sane. The aerodynamics of insect flight. *J. Exp. Biol.*, 206(23):4191–4208, 2003.

W. R. Sears. Some recent developments in airfoil theory. *J. Aeronautical Sci.*, 23(5): 490–499, 1956.

K. Taira and T. Colonius. Three-dimensional flows around low-aspect-ratio flat-plate wings at low Reynolds numbers. *J. Fluid Mech.*, 623:187–207, 2009.

M.S. Triantafyllou, A.H. Techet, and F.S. Hover. Review of experimental work in biomimetic foils. *IEEE J. Ocean. Eng.*, 29(3):585–594, 2004.

P. Trizila, C.-K. Kang, H. Aono, W. Shyy, and M. Visbal. Low-Reynolds-number aerodynamics of a flapping rigid flat plate. *AIAA J.*, 49(4):806–823, 2011.

M. Uhlmann. An immersed boundary method with direct forcing for the simulation of particulate flows. *J. Comput. Phys.*, 209(2):448–476, 2005.

M. Uhlmann. Direct numerical simulation of sediment transport in a horizontal channel. Technical Report No. 1088, CIEMAT, Madrid, Spain, 2006. ISSN 1135-9420.

O. V. Vasilyev. High order finite difference schemes on non-uniform meshes with good conservation properties. *J. Comput. Phys.*, 157(2):746–761, 2000.

M. S. Vest and J. Katz. Unsteady aerodynamic model of flapping wings. *AIAA J.*, 34 (7):1435–1440, 1996.

M. Visbal, T. O. Yilmaz, and D. Rockwell. Three-dimensional vortex formation on a heaving low-aspect-ratio wing: Computations and experiments. *J. Fluids Struct.*, 38: 58–76, 2013.

M. R. Visbal. Three-dimensional flow structure on a heaving low-aspect-ratio wing. AIAA Paper 2011-219, 2011a.

M. R. Visbal. Numerical investigation of deep dynamic stall of a plunging airfoil. *AIAA J.*, 49(10):2152–2170, 2011b.

M. R. Visbal. Flow structure and unsteady loading over a pitching and perching low-aspect-ratio wing. AIAA Paper 2012-3279, 2012.

K. Viswanath, K. Nagendra, J. Cotter, M. Frauenthal, and D.K. Tafti. Straight-line climbing flight aerodynamics of a fruit bat. *Phys. Fluids*, 26(2):604, 2014.

K. D. Von Ellenrieder, K. Parker, and J. Soria. Flow structures behind a heaving and pitching finite-span wing. *J. Fluid Mech.*, 490:129–138, 2003.

N. Yokoyama, K. Senda, M. Iima, and N. Hirai. Aerodynamic forces and vortical structures in flapping butterfly's forward flight. *Phys. Fluids*, 25(2):021902, 2013.

J. Young and J. C. S. Lai. Oscillation frequency and amplitude effects on the wake of a plunging airfoil. *AIAA J.*, 42(10):2042–2052, 2004.

L. Zheng, T.L. Hedrick, and R. Mittal. Time-varying wing-twist improves aerodynamic efficiency of forward flight in butterflies. *PLOS One*, 8(1):e53060, 2013.